Simulating the multi-phase interstellar medium and galactic outflows

Tim-Eric Rathjen

München 2021

Simulating the multi-phase interstellar medium and galactic outflows

Tim-Eric Rathjen

Dissertation
der Fakultät für Physik
der Ludwig-Maximilians-Universität
München

vorgelegt von
Tim-Eric Rathjen
aus Berg. Gladbach

München, den 27.07.2021

Erstgutachter: Prof. Dr. Simon D.M. White
Zweitgutachter: Porf. Dr. Andreas Burkert
Tag der mündlichen Prüfung: 11.10.2021

Contents

Zusammenfassung **ix**

Abstract **xi**

1 Introduction **1**
1.1 The interstellar medium 1
1.2 Studying the ISM via simulations 4
1.3 Introduction to emission line diagnostics 5
1.4 Goal and structure of this work 6

2 Multiphase ISM strucutre, stellar clustering and outflows with supernovae, stellar winds, ionising radiation, and cosmic rays **9**
2.1 Numerical methods 9
2.2 Simulation setup and parameters 12
2.3 Morphology and global evolution 14
2.4 Towards a complete model of the ISM 17
2.4.1 Star formation 17
2.4.2 Star cluster properties 22
2.4.3 The importance of supernova ambient densities 24
2.5 ISM structure 27
2.6 Implications for galactic outflows 30
2.6.1 Energy loading 32
2.6.2 Mass loading 36
2.7 This work in context 39
2.7.1 Possible caveats 43
2.8 Summary 43
2.9 Appendix A2 45
2.9.1 Phase structure of the outflow 45
2.9.2 Energy injection 46
2.9.3 Density flattening 47

3 Galactic outflows driven by cosmic rays and runaway stars **51**
3.1 Numerical realisation of runaway stars and type Ia SN 51
3.2 Simulation overview 52
3.3 Star formation 54
3.4 Supernova properties 54
3.5 Galactic outflows 62
3.5.1 Mass outflow 62
3.5.2 Energy outflow 62
3.5.3 Loading factors 64
3.5.4 Structure of the outflows 67
3.5.5 Outflowing gas velocities 69
3.6 This work in context 71
3.7 Summary 73

4 Optical emission line diagnostics for the simulated interstellar medium **75**
4.1 From ISM simulations to emission line diagnostics 75
4.1.1 Tests with idealised HII regions 78
4.1.2 The choice of the ionising spectrum 79
4.1.3 Resolution studies 83
4.2 Optical emission line diagnostics for the simulated ISM 84
4.2.1 Emission maps 88
4.2.2 BPT analysis 88
4.2.3 Origin of emission 91
4.2.4 Impact of beam resolution 94
4.3 Summary 96
4.4 Appendix A4 96

5 Conclusion and future prospects **99**

References **103**

List of Figures

1.1 Star-forming region Westerlund 2 . . . 3
1.2 Classic BPT diagram . . . 5

2.1 The SILCC Project - Simulation overview . . . 13
2.2 Time evolution of *S* and *SR* . . . 15
2.3 Time evolution of *SW* and *SWR* . . . 16
2.4 Time evolution of *SWC* and *SWRC* . . . 17
2.5 Star formation surface densities - Part 1 . . . 18
2.6 Kennicutt-Schmidt relation . . . 20
2.7 Gas depletion time-scales . . . 21
2.8 Star cluster accretion properties . . . 23
2.9 Star cluster mass distribution . . . 25
2.10 Ambient gas densities at SN explosion sites - Part 1 . . . 26
2.11 Volume-filling factors and mass fractions of the ISM . . . 28
2.12 Energy loading - Part 1 . . . 33
2.13 Energy loading relations . . . 35
2.14 Mass loading - Part 1 . . . 36
2.15 Mass loading relations . . . 38
2.16 Specific energy of the outflow . . . 40
2.17 A2: Energy loading components . . . 46
2.18 A2: Energy loading gas phases . . . 47
2.19 A2: Mass loading gas phases . . . 48
2.20 A2: Cumulative energy injection . . . 49
2.21 A2: Density flattening . . . 49

3.1 Gas column densities for four different gas surface densities . . . 57
3.2 SFR surface density - Part 2 . . . 58
3.3 Net mass loading factor . . . 59
3.4 Ambient gas densities at SN explosion sites - Part 2 . . . 60
3.5 Vertical position of the SN explosion sites . . . 61
3.6 Mass outflow rates . . . 63
3.7 Energy outflow rates . . . 64
3.8 Energy outflow rates - component-wise . . . 65

3.9 Loading factors . . . 66
3.10 Outflow energy density . . . 68
3.11 Volume-filling factors of the outflow . . . 69
3.12 Mass loading as a function of the hot gas volume-filling . . . 70
3.13 Outflow velocities . . . 71

4.1 Idealised HII regions . . . 78
4.2 BPT diagram of the idealised HII regions . . . 80
4.3 Exemplary spectrum with different models . . . 81
4.4 BPT study for different spectra . . . 82
4.5 Full spectrum and emission . . . 83
4.6 Resolution study . . . 84
4.7 Overview of the four simulations with increasing gas surface density at t_{25} . . . 86
4.8 Overview of the four simulations with increasing gas surface density at t_{50} . . . 87
4.9 Emission map for *s100*, t_{50} . . . 89
4.10 Optical emission line diagnostics of the ISM . . . 90
4.11 Compilation of the BPT diagnostics . . . 92
4.12 Phase diagrams of the emitting gas . . . 93
4.13 Emission fraction from the shocked gas . . . 94
4.14 Study to understand the impact of different beam sizes on the results in the BPT diagram . . . 95
4.15 A4: Emission maps *s010* . . . 97
4.16 A4: Emission maps *s030* . . . 97
4.17 A4: Emission maps *s050* . . . 97
4.18 A4: Emission maps *s100* . . . 98

List of Tables

1.1 The interstellar medium 2

2.1 Simulation overview and nomenclature - Part 1 14
2.2 Star cluster sink particle properties 24
2.3 Volume-filling factors and mass fractions of the ISM 30
2.4 Energy densities of the ISM 31
2.5 Loading factors 39
2.6 A2: Density flattening 48

3.1 Simulation overview and nomenclature - Part 2 53
3.2 Average SFRs 55
3.3 Supernova statistics 56
3.4 Loading factors 65

4.1 Interstellar abundances and depletion factors 77
4.2 Star formation and SN properties of the post-processed ISM simulations 85

Zusammenfassung

In dieser Arbeit wollen wir das mehrphasige interstellare Medium (ISM) unter solaren Bedingungen studieren, verstehen, wie massive Sterne ihre Umgebung formen, die treibenden Prozesse hinter galaktischen Ausströmungen untersuchen und Vorhersagen über die Emissionssignatur des ISM treffen. Wir nähern uns diesen Fragen mittels adaptiver Netzverfeinerungs- (AMR) und magnetohydrodynamischen- (MHD) Simulationen, in die wir alle wichtigen thermischen und nicht-thermischen ISM-Prozesse einbeziehen: Sternhaufenbildung mit der Möglichkeit Ausreißersterne zu beschleunigen, und Rückkopplung von massereichen Sternen, Sternwinde, wasserstoffionisierende Strahlung berechnet mit der neuartigen TreeRay-Strahlungsübertragungsmethode, Supernovae (SN) und Beschleunigung der kosmischen Strahlung (CR) in Supernova-Überresten.

Zunächst untersuchen wir systematisch den Einfluss von stellarer Rückkopplung auf das selbstgravitierende ISM mit Magnetfeldern, CR-Advektion und -diffusion sowie chemischer Entwicklung im Nichtgleichgewicht. Die Vernachlässigung der frühen stellaren Rückkopplung führt zu einem Sternenausbruch mit sehr hohen Sternhaufenmassen und starken Ausströmen. Durch frühe Strahlungsrückkopplung wird ein anfänglicher Sternenausbruch verhindert. In unseren Simulationen erhalten wir moderate Ausflussraten und Sternhaufenmassen gemäß den Beobachtungen. Volumenfüllfaktoren des warmen Gases, $\mathrm{VFF}_{\mathrm{warm}} = 60 - 80\%$, sowie thermische, kinetische, magnetische und kosmische Strahlungsenergiedichten des Modells einschließlich aller Rückkopplungsmechanismen stimmen gut mit Beobachtungen überein. Unsere Modelle zeigen, dass die Sternentstehung bei niedrigen Gasoberflächendichten auf Sternhaufenskalen durch Strahlung und Winde von massereichen Sternen reguliert wird.

Als Nächstes untersuchen wir die langfristigen Auswirkungen von CRs auf galaktische Ausflüsse. Darüber hinaus untersuchen wir, ob und wie Ausreißersterne einen Einfluss auf die Gasstruktur des ISM haben und ob sie einen galaktischen Ausfluss verstärken können. Wir finden heraus, dass CRs die Ausflussstruktur massiv verändern und den Massenladefaktor auf $\eta \approx 5 - 10$ erhöhen, selbst in einer Umgebung mit einem niedrigen Heißgas-VFF von $\mathrm{VFF}_{\mathrm{hot}} \approx 20\%$. Ausreißersterne, die entweder durch dynamische Interaktion oder durch einen SN-Kick in einem Doppelsternsystem aus Sternhaufen ausgestoßen werden, wandern entgegen der herkömmlichen Auffassung nicht in ein verdünnteres Medium als die Umgebung ihrer Geburtshaufen. Stattdessen explodieren die meisten Ausreißersterne in einem dichteren Medium als dem, aus dem sie stammen. Sie können jedoch in frühen Evolutionsstadien des ISM Fontänenströme auslösen, die die zukünftige Entwicklung des ISM prägen und die Gesamtausflussraten erhöhen.

Zum Abschluss dieser Studie entwickeln wir ein Werkzeug zur Nachbearbeitung unserer Si-

mulationen in Kombination mit dem Photoionisationscode CLOUDY und wenden es auf Simulationen mit unterschiedlichen Anfangsbedingungen mit Gasoberflächendichten bis zu $\Sigma_{\mathrm{Gas}} = 100\,\mathrm{M}_{\odot}\,\mathrm{pc}^{-2}$ an. Wir treffen Vorhersagen für die optische Linienemission des simulierten ISM und analysieren diese mit Linienverhältnisdiagnosen. Die Emission unserer ISM-Simulationen stimmt mit Beobachtungen lokaler Galaxien überein und wir können Aussagen über den Ursprung der Emission innerhalb unseres galaktischen Ausschnitts treffen.

Abstract

In this thesis, we want to study the multi-phase interstellar medium (ISM) at solar neighbourhood conditions, understand how massive stars shape their environment, examine the governing processes behind galactic outflows, and make predictions about the emission signature of the ISM. We approach these questions with adaptive mesh refinement (AMR), magneto-hydrodynamic (MHD) simulations in which we include all major thermal and non-thermal ISM processes, star cluster formation with the possibility to eject runaway stars, and feedback from massive stars: stellar winds, hydrogen ionising radiation computed with the novel TreeRay radiative transfer method, supernovae (SN), and acceleration of cosmic rays (CR) in supernova remnants.

First, we systematically investigate the impact of stellar feedback on the self-gravitating ISM with magnetic fields, CR advection and diffusion and non-equilibrium chemical evolution. Neglecting early stellar feedback leads to a starburst with very high star cluster masses and strong outflows. With early radiative feedback, an initial starburst is prevented. We achieve moderate outflow rates and star cluster masses, consistent with observations. Volume-filling factors of the warm gas, $\mathrm{VFF_{warm}} = 60 - 80$ per cent as well as thermal, kinetic, magnetic, and cosmic ray energy densities of the model including all feedback mechanisms agree well with observational constraints. Our models indicate that at low gas surface densities star formation is regulated on star cluster scales by radiation and winds from massive stars in clusters.

Next, we study the long-term impact CRs have on galactic outflows and examine if and how runaway stars exert an influence on the gas structure of the ISM and whether they can boost a galactic outflow. We find that CR massively change the outflow structure, increasing the mass loading factor to $\eta \approx 5 - 10$, even in an environment with a low hot gas VFF of $\mathrm{VFF_{hot}} \approx 20$ per cent. Runaway stars ejected from star clusters either by dynamical interaction or from a SN kick in a binary systems - contrary to conventional perception - do not propagate into a more rarefied medium than the environment of their natal clusters. But instead, the majority of runaway stars undergo SN explosion in a denser medium than they originate from. However, they can trigger fountain flows in early evolutionary stages of the ISM, which will then shape the future development of the ISM and increase the overall outflow rates.

Concluding this study, we develop a tool for post-processing our simulations in combination with the photo-ionisation code Cloudy, and apply it to simulations with a varying range of initial conditions with gas surface densities up to $\Sigma_{\mathrm{gas}} = 100\,\mathrm{M_\odot\,pc^{-2}}$. We make predictions for optical line emission of the simulated ISM and analyse them with line ratio diagnostics. The emission from our ISM simulations aligns with observations of local galaxies and we can make assumptions about the origin of emission within our galactic patch.

Chapter 1

Introduction

1.1 The interstellar medium

The interstellar medium (ISM) is traditionally defined as *everything* in-between the stars in galaxies, accounting for the non-stellar and non-relativistic baryonic matter, radiation, magnetic fields, and cosmic rays (CR) in galactic discs. In the ISM, star formation takes place, galactic outflows are launched, and galaxies grow in size and mass. Through an inflow/outflow interface, the ISM smoothly transitions to the circumgalactic medium (CGM) occupying the more spherical galactic halo. The CGM can contain significant fractions of the total baryonic mass which is gravitationally bound to galaxies but shows no evidence for star formation (Tumlinson et al., 2017). The inflow and outflow of gas from and into the ISM are of uttermost importance to understand the evolution of galaxies. Molecular clouds condense out of the hot and warm ISM. In those clouds dense filaments form which undergo fragmentation and collapse resulting in the formation of new stars and star clusters. Those star clusters disperse their natal environment via stellar feedback and create bubbles on different spatial scales. Overlapping bubbles heat the gas and drive outflows into the CGM. Some amount of gas in the CGM cools and falls back into the ISM, replenishing the gas reservoir and restarting the matter cycle by creating the next generation of stars.

The ISM is of a multi-phase nature with ionised, neutral, and molecular gas as well as dust (Draine, 2010). The cold and warm components are believed to be in pressure equilibrium (Wolfire et al., 2003; Cox, 2005). An additional meta-stable hot phase exists with gas temperatures exceeding $T = 10^5$ K (Cox & Smith, 1974; McKee & Ostriker, 1977; Ferrière, 2001; Klessen & Glover, 2016) generated predominately by supernova (SN) explosions.

Molecular gas is typically found in structured and compact molecular clouds, where all new stars in galaxies are born (McKee & Ostriker, 2007; Kennicutt & Evans, 2012). Those molecular clouds can be formed by cooling and gravitational collapse of the magnetised gas in dust shielded regions (Kennicutt & Evans, 2012; Ibáñez-Mejía et al., 2017) or by sweeping up gas and supersonic compression from multiple SN explosions (Inutsuka et al., 2015; Seifried et al., 2017). Most of the volume in the ISM, however, is occupied by neutral and ionised gas. Interstellar radiation from stars or gas cooling processes is also part of the ISM (Ferrière, 2001).

Table 1.1: Temperature, T, number density, n, and surface density, Σ, of the different components of the ISM in the solar neighbourhood (Ferrière, 2001, and references within).

Component	T [K]	n [cm^{-3}]	Σ [M$_\odot$ pc^{-2}]
Molecular	10 - 20	10^2 - 10^6	$\sim$ 2.5
Cold atomic	50 - 100	20 - 50	$\sim$ 3.5
Warm atomic	6×10^3 - $\times10^4$	0.2 - 0.5	$\sim$ 3.5
Warm ionised	$\sim 8 \times 10^4$	0.2 - 0.5	$\sim$ 1.4
Hot ionised	$\sim 10^6$	$\sim 6.5 \times 10^{-3}$	-

Additionally, magnetic fields and CRs – typically protons at relativistic speeds – are energetically equally important non-thermal components (Draine, 2010; Heitsch et al., 2009; Crutcher, 2012) and might play a vital role in the evolution of galaxies (see e.g. Naab & Ostriker, 2017, for an overview).

Feedback from massive O and B stars has the strongest impact on the environment by injecting radiation, momentum, and energy into the ISM (Mac Low & Klessen, 2004; Krumholz et al., 2014; Haid et al., 2018). Massive stars form in clusters (Lada & Lada, 2003) and create HII regions by ionising and heating their surroundings with UV radiation (see e.g. Spitzer, 1978; Whitworth, 1979; Dale et al., 2005, 2012; Walch et al., 2012, 2013; Dale et al., 2014; Geen et al., 2015; Haid et al., 2018, 2019; Kim et al., 2021). Additionally, stellar winds partly disperse their parental clouds (see e.g. Castor et al., 1975; Weaver et al., 1977; Wünsch et al., 2008, 2011; Toalá & Arthur, 2011; Dale et al., 2012; Rogers & Pittard, 2013; MacKey et al., 2015; Haid et al., 2018). At the end of a massive stars lifetime, SNe drive strong shocks into the ISM by generating hot ionised gas in expanding super-bubbles (see e.g. Mac Low & McCray, 1988; Mac Low et al., 1989; Gatto et al., 2015; Kim & Ostriker, 2015; Martizzi et al., 2015; Walch et al., 2015; Walch & Naab, 2015; Haid et al., 2016). CRs generated in these shocks interact with the magnetic field and generate an additional pressure component whose gradient can drive gas out of the ISM (Dorfi & Breitschwerdt, 2012; Simpson et al., 2016; Girichidis et al., 2016b, 2018a). Local observations suggest that CRs are accelerated by diffusive shock acceleration in SN remnants (Bell, 1978; Blandford & Ostriker, 1978) with an efficiency of $\sim$ 10 per cent (Helder et al., 2012; Ackermann et al., 2013). CRs have energy densities $u_{\rm cr} \approx 1.4\,$eV cm^{-3}, comparable to the thermal, turbulent, and magnetic energy densities (Draine, 2010). The impact of this relativistic component has only recently been investigated in numerical ISM and galaxy formation studies (e.g. Hanasz et al. 2013; Booth et al. 2013; Salem & Bryan 2014; Girichidis et al. 2016b; Pakmor et al. 2016; Simpson et al. 2016; Girichidis et al. 2018a).

The most dramatic single events, however, are the blast waves generated by SNe. They have a considerable dynamical impact on the ISM (McKee & Ostriker, 1977; Mac Low & Klessen, 2004). The SN impact can be stronger if they explode in low-density environments (Creasey et al., 2013; Martizzi et al., 2015; Gatto et al., 2015; Iffrig & Hennebelle, 2015; Kim & Ostriker, 2015; Walch et al., 2015; Fielding et al., 2017), otherwise, their injected energy is typically radiated away without strong coupling to the ambient gas (Walch et al., 2015; Naab & Ostriker,

Figure 1.1: The star-forming region Westerlund 2, located in the Carina nebula, captured in near-infrared and visible light by the Hubble Space Telescope. A perfect real-life example of the ISM processes discussed in the text. A cluster of young, hot and massive O stars blew a large cavity into the dense gas cloudy via stellar winds and ionising radiation. Dark red/brownish pillars of dense gas and dust, shaped by the violent stellar feedback from the massive stars, are the birthplaces for the next generation of stars. ©NASA, ESA, the Hubble Heritage Team (STScI / AURA), A. Nota (ESA/STScI), and the Westerlund 2 Science Team.

2017), even to the point that no Sedov-Taylor stage is developed (Jiménez et al., 2019). The non-linear interaction of clustered star formation, thermal and non-thermal feedback processes with the highly structured multi-phase ISM can be best investigated with numerical simulations.

Massive stars, the source of the feedback and precursors of the SNe, do not form by themselves. Instead, they form embedded in dense molecular clouds and young massive clusters (Lada & Lada, 2003). However, not all massive stars stay and end their lives within their natal clusters. Observations tell us that approximately 20 – 30 per cent of the O stars are located outside star clusters or OB associations, although this value varies up to 50 per cent, especially in older literature (Blaauw, 1964; Stone, 1991; Tetzlaff et al., 2011). These stars travel at speeds in excess of 30 $\mathrm{km\,s^{-1}}$, traversing distances of hundreds of parsecs before exploding as SNe, so the explosions usually occur in environments with different gas densities than their progenitor star clusters. Since previous works showed that the impact of SNe on the ISM depends on SNe

positioning and SNe environmental density, runaway OB stars pose the potential to strongly exert influence on the dynamics of the galactic disc, the structure of the gas above the disc, and SN-driven fountain flows. Two mechanisms were proposed to explain the origin of runaway OB stars, which can be back-traced to virtually any OB association. The first mechanism is the dynamical ejection scenario (DES), introduced by Poveda et al. (1967), where the runaways are produced in complicated three- or many-body encounters between stars or binaries in the core of a young, perhaps still embedded, star cluster. This mechanism can explain the abundance and velocities of observed runaway OB stars (Fujii & Portegies Zwart, 2011; Oh et al., 2015; Perets & Šubr, 2012). The second mechanism is the binary supernova scenario (BSS), introduced by Blaauw (1964). It is based on the observational fact that the vast majority of OB stars is observed in relatively close binaries and multiple systems. Many of the binaries are at orbital speeds of several tens of km s^{-1} or higher, so when the primary explodes as SN, and the SN remnant gets its natal kick, the secondary either escapes the system with its orbital speed or gets dragged with the SN remnant depending on the mass of these objects and their orbital separation (Portegies Zwart et al., 2010; Renzo et al., 2019). These two mechanisms produce runaway stars at different times. The dynamical ejection scenario needs a high-density environment, e.g. young open clusters, to be effective. It starts ejecting stars soon after the clusters formation and stalls after $\sim 2-3$ Myr (Poveda et al., 1967; Oh et al., 2015). The binary supernova scenario on the other hand starts ejecting stars with lesser efficiency with the onset of supernova events within the stellar cluster $\gtrsim 3$ Myr but keeps ejecting stars at a constant rate proportional to the supernova rate.

1.2 Studying the ISM via simulations

A theoretical approach to understanding the processes which govern the ISM are numerical simulations. Idealised stratified galactic disc simulations have followed the evolution of the multi-phase ISM and outflows driven by SNe with fixed rates inferred from observations (e.g. De Avillez & Breitschwerdt, 2005; Joung & Mac Low, 2006; Hill et al., 2012; Gent et al., 2013; Walch & Naab, 2015; Girichidis et al., 2016b; Li et al., 2015, 2017). Such approaches, however, do not allow for a self-consistent study of the evolution of the star-forming ISM. Current approaches allow for the modelling of star formation via sink particles (Federrath et al., 2010; Gatto et al., 2017; Peters et al., 2017; Iffrig & Hennebelle, 2017; Kim & Ostriker, 2017, 2018) and include feedback from massive stars by SNe (e.g. Gatto et al., 2017; Kim & Ostriker, 2017), SNe and stellar winds (Gatto et al., 2017), SNe and radiation either directly (e.g. Butler et al., 2017) or in post-processing (Kado-Fong et al., 2020), or SNe, stellar winds and radiation combined (Peters et al., 2017). ISM studies on the impact of CRs have, so far, no self-consistent star formation included.

Within the SILCC project[1] and related publications, the governing processes setting the ISM structure have been studied in idealised experiments. We have subsequently included feedback processes from SNe (Walch et al., 2015; Girichidis et al., 2016a), stellar winds (Gatto et al., 2017), ionising radiation (Peters et al., 2017) and magnetic fields (Pardi et al., 2017; Girichidis et al.,

[1] https://hera.ph1.uni-koeln.de/~silcc/

2018b). There are strong indications that radiation impacts and reduces the SFR and qualitatively changes the ISM structure. Therefore, this process has to be taken into account in studies aiming at creating a realistic model of the multi-phase ISM.

1.3 Introduction to emission line diagnostics

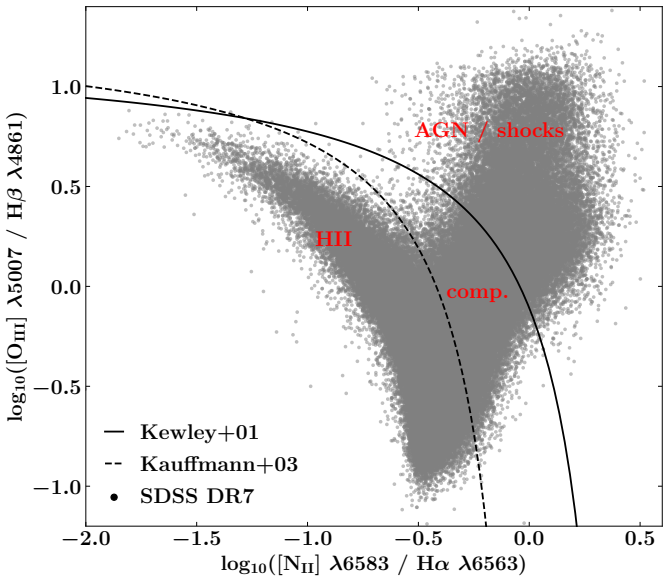

Figure 1.2: Baldwin, Phillips & Terlevich emission line ratio diagnostic (Baldwin et al., 1981, BPT hereafter). Shown in grey is optical emission line data from the Sloan Digital Sky Survey data release 7 (SDSS DR7, Abazajian et al., 2009). The solid and dashed black lines represent the maximum starburst limits by Kewley et al. (2001) and Kauffmann et al. (2003), respectively.

The main channel through which we can learn about the Universe is the study of light. In 1814, Joseph von Fraunhofer discovered dark features in the spectrum of the sun. Later, Gustav Kirchhoff and Robert Bunsen discovered that the *Faunhofer lines* coincide with emission lines of several heated elements. They deduced that the Fraunhofer lines are indeed absorption lines of exactly those elements. By this method, the composition of the sun's atmosphere was deciphered. Nowadays, we can use the study of optical emission lines of whole galaxies to deduce many properties like electron density, temperature, ISM pressure, ionisation sources and metallicity (Kewley et al., 2019, and references therein). The optical spectrum of a galaxy can differ substantially from another depending on the prevalent conditions in the galaxy. When a galaxy is in the phase or active star formation, there will be a signature in the spectrum. If, on the other hand, a galaxy is dominated by an actively feeding supermassive black hole (AGN) in its centre, the spectrum of the emission lines will show a completely different signature. One very powerful tool to classify the emitting galaxy is the Baldwin, Phillips & Terlevich emission line ratio diagnostic (Baldwin et al., 1981, BPT hereafter). With the line ratios [N_{II}] / Hα vs [O_{III}] /

Hβ it is possible to distinguish the dominant ionisation source in a emission line galaxy. AGN have a harder UV radiation field compared to a HII region, leading to a stronger excitation of [O_{III}] as well as [N_{II}]. The resulting emission line ratios would move to the upper right part of the BPT diagram (Fig. 1.2. HII regions, on the other hand, form a very clear sequence as a function of metallicity, ISM pressure and ionisation parameter,

$$U = \Phi \cdot n_{\rm H}^{-1} \cdot c^{-1} = n_\gamma \cdot n_{\rm H}^{-1}, \tag{1.1}$$

with the ionising photon flux, Φ, the speed of light, c, the hydrogen density, $n_{\rm H}$ and the density of ionising photons, n_γ. Kewley et al. (2001) developed a purely theoretical classification scheme by combining stellar population synthesis, photo-ionisation and shock models to derive a *maximum starburst line*, an upper limit for star-forming galaxies (solid black line in Fig. 1.2). Any emission line ratios above this line cannot be explained purely by star formation and must contain a significant contribution from either AGN or fast radiative shocks (Allen et al., 2008; Kewley et al., 2006, 2019). Shown as grey dots in Fig. 1.2 are a total of $\sim$ 200000 observations of local galaxies within a redshift range of $0.04 \leq z \leq 0.2$ selected by a high signal-to-noise ratio in all four shown optical emission lines from the Sloan Digital Sky Survey, DR7 (SDSS DR7 Abazajian et al., 2009). Kauffmann et al. (2003) made a semi-empirical fit of the Kewley et al. (2001) line to an outer bound of the SDSS galaxies and arrived at another classification line (dashed line in Fig. 1.2). The region between the two classification lines contains composite objects which are considered to have significant contributions from AGN as well as HII regions.

1.4 Goal and structure of this work

With this work, we aim to study the multi-phase ISM while accounting for all major thermal and non-thermal ISM processes. These processes include self-consistent star formation in the self-gravitating disk of the ISM, star cluster formation with the possibility to eject single massive runaway stars, early feedback in form of stellar winds and ionising radiation, thermal feedback from SNe, both type Ia and type II, non-equilibrium chemistry with shielding and self-shielding of H_2 and CO, CR acceleration in SN remnants and the advection and anisotropic diffusion of CR along magnetic fields. We wish to show that all of the aforementioned processes are important to account for when trying to give a full picture of the ISM and galactic outflows. We give explanations for the effects each of those processes has on the ISM by systematically investigating them in numerical experiments. We carry out an extensive suite of numerical simulations within the SILCC framework (Walch et al., 2015; Girichidis et al., 2016a; Gatto et al., 2017; Peters et al., 2017; Girichidis et al., 2018b; Rathjen et al., 2021), based on the MPI parallel, 3D adaptive mesh refinement magneto-hydrodynamics (MHD) code FLASH (Fryxell et al., 2000; Dubey et al., 2008, 2009).

In Chapter 2, we focus on the structure of the ISM and investigate how stellar feedback regulates star formation and impacts galactic outflows. We run a total of six high-resolution, parsec-scale, stratified disk MHD simulations of the solar neighbourhood at increasing physical complexity and realism. We present the first time application of the novel radiative transfer method TreeRay (Wünsch et al., 2021), the novel implementation of a $4^{\rm th}$-order Hermite integrator for

computing the N-body dynamics of the stellar cluster sink particles (Dinnbier & Walch, 2020), and the novel CR injection and propagation prescription (Girichidis et al., 2018a, 2020), in a self-consistent large-scale ISM simulation.

We build up upon the results of Chapter 2 and extend our analysis with another set of six ISM simulations in Chapter 3, in which we study the long-term impact of CR and runaway stars on galactic outflows. We let the ISM in our simulations evolve through multiple episodes of star formation up to a simulated time of $t = 250\,\mathrm{Myr}$. We put a special emphasis on the influence runaway stars have on the ISM and demonstrate how the inclusion of runaway stars can increase the overall mass outflow rates by establishing warm gas fountain flows in the early stages of the simulation. In combination with Chapter 2, this study gives more insights towards a complete picture of the ISM.

In the third part of this thesis (Chapter 4), we are moving on from simulating the ISM and engage in optical emission line diagnostics. We have developed a tool in combination with the photo-ionisation code Cloudy (Ferland et al., 2017), which lets us post-process our high-resolution ISM simulations and predict the emission signature of the simulated ISM. We test and benchmark our tool with idealised HII region simulations based on the SILCC framework and then deploy it to a set of four full ISM simulations with increasing initial gas surface densities, ranging from $\Sigma_{\mathrm{gas}} = 10\,\mathrm{M}_\odot\,\mathrm{pc}^{-2}$ up to $\Sigma_{\mathrm{gas}} = 100\,\mathrm{M}_\odot\,\mathrm{pc}^{-2}$. We examine the predicted emission lines with classic line ratio diagnostic tools (Baldwin et al., 1981) and analyse the possible origins of the emission. To our knowledge, this is the first time an analysis like this is carried out to that level of complexity.

We introduce and explain numerical methods and techniques used in each chapter separately at the beginning of each chapter. To not hinder the reading flow, we put additional material of each chapter into a separate appendix, if applicable.

The foundation of this work are a total of 16 high-resolution, parsec-scale ISM simulations with different levels of complexity. Those simulations were carried out by one part on the dedicated computing cluster Freya hosted by the Max Planck Computing & Data Facility[2], as well as on the high-performance-computing cluster SuperMUC hosted by the Gauss Centre for Supercomputing e.V.[3] within the 40 Mio. CPU-h grant pn34ma.

[2] https://www.mpcdf.mpg.de/
[3] https://www.gauss-centre.eu

Chapter 2

Multiphase ISM strucutre, stellar clustering and outflows with supernovae, stellar winds, ionising radiation, and cosmic rays

In this Chapter, we will present the effects of stellar feedback with increasing complexity on the ISM, analysed via numerical simulations. We put an emphasised focus on the SN properties and the strong influence of star cluster formation on the shape of the ISM and its capability to drive outflows. The results of this chapter are peer-reviewed and published in *Mon. Not. R. Astron. Soc.*, 504, 1039 (Rathjen et al., 2021).

2.1 Numerical methods

Stratified disc patches are simulated using the MPI parallel, 3D adaptive mesh refinement magneto-hydrodynamics (MHD) code FLASH (Fryxell et al., 2000; Dubey et al., 2008, 2009). Our setup follows the general SILCC framework (Walch et al., 2015; Girichidis et al., 2016a; Gatto et al., 2017; Peters et al., 2017; Girichidis et al., 2018b) with the inclusion of the radiative transfer solver TreeRay (Wünsch et al., 2021), 4^{th}-order Hermite integrator for sink particle N-body dynamics Dinnbier & Walch (2020), and anisotropic CR transport as in Girichidis et al. (2016b, 2018a). The MHD equations are solved with a modified, directionally split, three-wave Bouchut scheme (HLLR3) for ideal MHD, suitable for flows of high Mach number (Bouchut et al., 2007, 2010; Klingenberg et al., 2007; Waagan et al., 2011). Self-gravity is accounted for by solving the Poisson equation via an Oct-tree based method (Barnes & Hut, 1986; Wünsch et al., 2018). An external potential is also included to model the gravitational impact of the pre-existing stellar disc and the contribution of a dark matter halo.

We explicitly follow the non-equilibrium time-dependent chemical evolution of H, H^+, H_2, C^+, CO (Nelson & Langer, 1997; Glover & Mac Low, 2007) and account for photoelectric heating and radiative cooling, assuming a constant far ultraviolet (FUV) interstellar radiation field (ISRF)

with $G_0 = 1.7$ (Draine, 1978) and a constant dust-to-gas ratio of 1 per cent. The local optical depth of gas and dust and hence their shielding and self-shielding are calculated with the TreeCol algorithm (Clark et al., 2012; Wünsch et al., 2018). We refer the reader to Walch et al. (2015) for a detailed description of the chemical network and the shielding processes included.

Star formation is modelled with accreting Lagrangian sink particles, which represent star clusters (see Gatto et al., 2017). For each cluster sink, we explicitly follow the evolution of massive stars in a mass range $m_\star = 9 - 120\,\mathrm{M}_\odot$. For every $120\,\mathrm{M}_\odot$ of accreted gas, we form one new massive star sampled from a Salpeter IMF (Salpeter, 1955). Accretion and formation of the sink particles are described by Federrath et al. (2010), with an accretion radius of $r_{\rm accr} = 3 \times \Delta x$ ($\sim 11.7\,\mathrm{pc}$ at the highest refinement level with $\Delta x \approx 3.9\,\mathrm{pc}$) and a particle threshold density of $n_{\rm sink} \approx 10^3\,\mathrm{cm}^{-3}$. Furthermore, the gas within $r_{\rm accr}$ has to be in a converging flow, gravitationally bound, Jeans unstable, and in a local gravitational potential minimum to form or be accreted by a sink particle. The accretion radius depends on the grid resolution and is chosen to be as small as possible without creating grid artefacts (see e.g. Federrath et al., 2010; Hennebelle & Iffrig, 2014; Gatto et al., 2017; Peters et al., 2017). If all accretion criteria are fulfilled, the gas that is above the threshold density within the accretion radius is added to the sink particle. It is important to note that not all the gas of the respective cells is accreted by the sink particle but only the difference between its actual density and the threshold density. Otherwise, the sink particles would create holes in the density structure of the ambient medium and potentially trigger runaway collapse. Therefore, there is no inherent minimum star cluster sink particle mass. Furthermore, the total gas density of cells within a sink particle's accretion radius is not necessarily at the threshold density of $n_{\rm sink} \approx 10^3\,\mathrm{cm}^{-3}$. We note that many cells within a sink particle's accretion radius are below that density. The trajectories of the cluster sinks are computed with an $4^{\rm th}$-order Hermite predictor-corrector integration scheme (see Dinnbier & Walch, 2020, for details). The sink particles are coupled to the Oct-tree which makes the calculations of their interaction with the gas efficient for a large number of particles.

Type II supernovae (SNe) are realised by injecting $E_{\rm sn} = 10^{51}\,\mathrm{erg}$ as thermal energy into a spherical region with fixed radius $r_{\rm inj} = 3 \times \Delta x$ (~ 11.7 pc) around the sink particle in which a massive star explodes. We evenly distribute the ejecta mass in the same region and keep the density fluctuations in the injection region intact, i.e. we do not *by hand* flatten the density to an average value.

The SN remnant radius at the end of the Sedov-Taylor-phase (Blondin et al., 1998) is

$$R_{\rm ST} = 19.1 \left(\frac{E_{\rm SN}}{10^{51}\mathrm{erg}}\right)^{5/17} \left(\frac{\overline{n}}{\mathrm{cm}^{-3}}\right)^{-7/17} \mathrm{pc}. \tag{2.1}$$

To resolve this radius with at least 3 grid cells, the ambient density of a SN explosion site must not exceed $n_{\rm ambient} = 3.3\,\mathrm{cm}^{-3}$. If the average ambient density is above this threshold, we switch to momentum injection and deposit the expected radial blast wave momentum at the beginning of the momentum conserving snowplough phase into the injection region. Furthermore, we set the temperature of the injection region to $T = 10^4\mathrm{K}$ as described in Gatto et al. (2017).

To account for stellar winds, we inject mass and radial momentum of each massive star in a cluster sink using mass loss rates form the Geneva stellar evolution tracks from the zero-age

main sequence to the Wolf-Rayet phase (Ekström et al., 2012). The terminal wind velocities are estimated according to Puls et al. (2008). The mass of the wind is evenly distributed in the injection region and the wind is assumed to be spherically symmetric. Chemical abundances in the injection region are kept unchanged. All details are discussed in Gatto et al. (2015).

The propagation of ionising UV photons from massive stars is handled with the novel TreeRay algorithm (Wünsch et al., 2021) which has been benchmarked and applied in Bisbas et al. (2015) and Haid et al. (2018, 2019). It is a backwards ray-tracing scheme which uses the Oct-tree structure from the gravity- and diffuse radiation solver described in Wünsch et al. (2018). The method couples self-consistently to the chemistry using one energy bin for photons with energy $h\nu \geq 13.6\,\mathrm{eV}$. Heating by the UV is calculated using the mean excess photon energy as described in Haid et al. (2019). First, the gas with its emission and absorption coefficients and the emitting sources are mapped onto the Oct-tree. Rays are then cast from each target cell via the HEALPix algorithm (Gorski et al., 2005), which distributes the rays uniformly over the surface of a unit sphere. Then, the 1D radiative transport equation is solved along each ray accounting for the radiation passing through the calculated ray from other directions. Finally, the whole process is repeated until the radiation density converges everywhere. The great advantage of this approach is that the cost of computation does not depend on the number of sources and hence multiple radiating star clusters can be handled effectively. The UV photons coming from the massive stars are injected within the star cluster sink particle's accretion radius. However, the photons will already be locally absorbed and re-processed by the gas in the cells in which they get injected, and then propagated by the aforementioned mechanism. The photons are not launched from the surface of the sink particles but their centre. The absorption of the UV photons within the sink particle's radius is treated by the radiation transfer module in the same way as in the other cells along the UV photon's propagation. Nonetheless, local porosity and clumps cannot be resolved on scales below the cell size of $\Delta x \approx 4\,\mathrm{pc}$. The UV photon escape fraction from compact and ultra-compact HII regions (cHII) is an uncertainty in our models for resolution reasons. Still, the lifetime of cHII regions is of order $\sim 0.3\,\mathrm{Myr}$ (Mottram et al., 2011), less than ~ 10 per cent of the lifetime of the massive stars powering the HII regions. We do not expect this uncertainty to have a large impact on our results. Photoelectric heating and photo-dissociation of H_2 is not treated by the radiative transfer module but is instead included through the assumed-uniform ISRF, which is attenuated at high column densities. The current prescription simplifies the role of dust, which can either decrease UV ionisation by attenuation or on the other hand enhance the UV escape fraction by excavating the centre of HII regions via radiation pressure, which is not included in our models. We justify the omission of radiation pressure by noting that radiation pressure is only expected to play an important role in molecular cloud dispersal on scales smaller than those that we resolve (Olivier et al., 2021) and for star clusters more massive than the ones that form in our simulations (Rahner et al., 2017; Reissl et al., 2018). For molecular cloud scales like in our models the UV radiation will quickly be absorbed and re-emitted in the thermal infrared, at which wavelength the clouds are optically thin.

CRs are treated as an additional non-thermal, relativistic fluid in the advection-diffusion approximation. They add another source term Q_{cr} to the MHD equations (Girichidis et al., 2016b, 2018a), including the injection of CRs by SNe with an efficiency of 10 per cent (i.e. $E_{\mathrm{cr}} = 10^{50}\,\mathrm{erg}$, Helder et al. 2012; Ackermann et al. 2013) as well as hadronic losses $\Lambda_{\mathrm{hadronic}}$ as

described in Pfrommer et al. (2017) and Girichidis et al. (2020). We assume a steady-state energy spectrum. For the CR diffusion tensor, we choose $K_{\parallel} = 10^{28}$ cm^2 s^{-1} parallel to the magnetic field lines and $K_{\perp} = 10^{26}$ cm^2 s^{-1} perpendicular to the magnetic field lines (Strong et al., 2007; Nava & Gabici, 2013). With CRs added, the complete set of MHD equations reads

$$\frac{\partial \rho}{\partial t} + \nabla \cdot (\rho \mathbf{v}) = 0 \tag{2.2}$$

$$\frac{\partial \rho \mathbf{v}}{\partial t} + \nabla \cdot \left(\rho \mathbf{v}\mathbf{v}^{\mathrm{T}} - \frac{\mathbf{B}\mathbf{B}^{\mathrm{T}}}{4\pi} \right) + \nabla P_{\mathrm{tot}} = \rho \mathbf{g} + \dot{\mathbf{q}}_{\mathrm{sn}} \tag{2.3}$$

$$\frac{\partial e}{\partial t} + \nabla \cdot \left[(e + P_{\mathrm{tot}})\, \mathbf{v} - \frac{\mathbf{B}\,(\mathbf{B} \cdot \mathbf{v})}{4\pi} \right] = \rho \mathbf{v} \cdot \mathbf{g} + \nabla \cdot (\mathsf{K} \nabla e_{\mathrm{cr}}) + \dot{u}_{\mathrm{chem}} + \dot{u}_{\mathrm{sn}} + Q_{\mathrm{cr}} \tag{2.4}$$

$$\frac{\partial \mathbf{B}}{\partial t} - \nabla \times (\mathbf{v} \times \mathbf{B}) = 0 \tag{2.5}$$

$$\frac{\partial e_{\mathrm{cr}}}{\partial t} + \nabla \cdot (e_{\mathrm{cr}} \mathbf{v}) = -P_{\mathrm{cr}} \nabla \cdot \mathbf{v} + \nabla \cdot (\mathsf{K} \nabla e_{\mathrm{cr}}) + Q_{\mathrm{cr}}, \tag{2.6}$$

with the mass density ρ, the gas velocity $\mathbf{v}$, the magnetic field $\mathbf{B}$, the total pressure $P_{\mathrm{tot}} = P_{\mathrm{thermal}} + P_{\mathrm{magnetic}} + P_{\mathrm{cr}}$, the total energy density $e = \frac{\rho v^2}{2} + e_{\mathrm{thermal}} + e_{\mathrm{cr}} + \frac{B^2}{8\pi}$, the momentum input of unresolved SNe $\dot{\mathbf{q}}_{\mathrm{sn}}$, the thermal energy input from resolved SNe, $\dot{u}_{\mathrm{sn}}$, the changes in thermal energy due to heating and cooling, $\dot{u}_{\mathrm{chem}}$, the CR diffusion tensor, K, and the CR energy source term, $Q_{\mathrm{cr}} = Q_{\mathrm{cr,injection}} + \Lambda_{\mathrm{hadronic}}$. The resulting effective adiabatic index is $\gamma_{\mathrm{eff}} = \frac{\gamma P_{\mathrm{thermal}} + \gamma_{\mathrm{cr}} P_{\mathrm{cr}}}{P_{\mathrm{thermal}} + P_{\mathrm{cr}}}$ with $\gamma = \frac{5}{3}$ and $\gamma_{\mathrm{cr}} = \frac{4}{3}$.

2.2 Simulation setup and parameters

We run a suite of six stratified box simulations. They all have a size of 0.5 kpc × 0.5 kpc × 4 kpc with periodic boundaries in x- and y- direction and strictly outflow boundary conditions in the z-direction, i.e. no material is allowed to flow back into the box. Those boundary conditions do not allow for shearing flows and therefore the impact of galactic shear is not accounted for in this study. Possible ramifications of this omission are discussed in Sec. 2.7. Within $z = \pm 1$ kpc, we always adopt a resolution of $\Delta x \approx 3.9$ pc, whereas outside of this region we adopt a base resolution of $\Delta x \approx 7.8$ pc with the possibility to refine on the density gradient up to $\Delta x \approx 3.9$ pc. We set up the gas with a Gaussian distribution in z and a scale height of 30 pc with a surface density of $\Sigma_{\mathrm{gas}} = 10\,\mathrm{M}_{\odot}\,\mathrm{pc}^{-2}$ and solar metallicity, mimicking solar neighbourhood conditions. The medium is magnetised with an initial magnetic field along the x-axis of the box and field strength of $B_x = 6\ \mu$G. At the beginning of the simulation, the gas in the mid-plane is set to be in pressure equilibrium and purely atomic. We artificially drive large-scale turbulence for the first 10 Myr to introduce inhomogeneities and prevent the gas from collapsing into a thin sheet in the mid-plane. This is done by injecting kinetic energy on the largest scale corresponding to the box side-length $L_x = L_y = 0.5$ kpc with a mix of 2:1 of solenoidal to compressive modes (Schmidt et al., 2009; Konstandin et al., 2015) so that the gas stays at a constant root mean square velocity

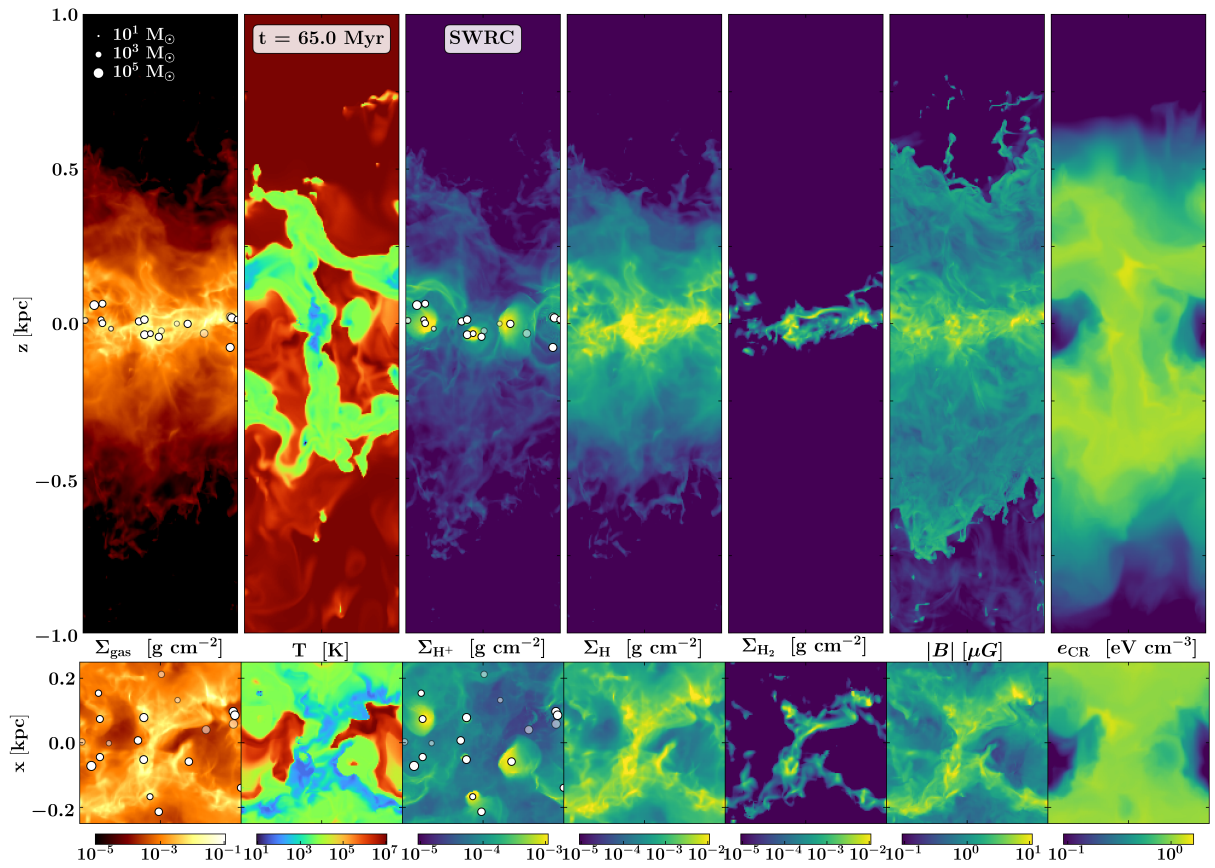

Figure 2.1: Overview of the *SWRC* (see Table 2.1) run, including supernovae, stellar winds, UV radiation and cosmic rays, at $t = 65$ Myr. Edge-on (top row) and face-on (bottom row) views of the total gas, ionised-, atomic-, and molecular hydrogen column densities. Individual HII regions (3$^{\rm rd}$ panel) from active star clusters are visible. We also show the density-weighted column of the magnetic field strength (6$^{\rm th}$ panel) and slices through the centre of the simulation box with temperature (2$^{\rm nd}$ panel) and CR energy density (7$^{\rm th}$ panel). The star-forming galactic ISM is concentrated around the mid-plane. White circles in the 1$^{\rm st}$ and 3$^{\rm rd}$ panel indicate star clusters with different masses. Translucent symbols indicate *old* star clusters with no active massive stars in them. Stellar feedback generates a highly structured and turbulent multi-phase ISM with all its major thermal and non-thermal components.

of $v_{\rm rms} = 10\,{\rm km s^{-1}}$ (Eswaran & Pope, 1988). For the external potential, we take an isothermal sheet (Spitzer, 1942) with a stellar surface density of $\Sigma_\star = 30\,{\rm M_\odot\,pc^{-2}}$ and a vertical scale height $z_{\rm d} = 300$ pc for the stars. For the dark matter, we assume an NFW profile (Navarro et al., 1996) with a virial radius of $R_{\rm vir} = 200$ kpc and concentration parameter $c = 12$, at a distance from the galactic centre of $R_{\rm D} = 8$ kpc as in Li et al. (2017).

With each simulation, we increase the level of stellar feedback complexity. The run labelled as *S* only includes the feedback of SNe at the end of the lifetime of each massive star. In run *SW*, we add continuous stellar wind feedback, in run *SR*, we add ionising radiation from the massive

stars, and in run *SWR*, we account for the three feedback mechanisms together. The injection of CRs through SN remnants is introduced in the runs *SWC* and *SWRC*. All simulations cover 100 Myr of evolution. In this time the ISM can be evolved through multiple cycles of star formation. An overview of the simulations is given in Table 2.1.

In Fig. 2.1 we give a general overview of what our most realistic simulation looks like. We show *SWRC* at a later stage of its evolution at $t = 65$ Myr. The upper row is an edge-on view and the lower row a face-on view of the total gas column density, temperature as a slice, ionised, atomic, and molecular hydrogen column density, density-weighted magnetic field strength column, and CR energy density as a slice. The white circles in the 1st and 3rd panels show the star clusters with their drawn size scaled to their respective masses. Please note that this size does not accurately reflect the actual physical size of stars clusters, which is only several parsecs (McLaughlin & van der Marel, 2005; Bastian et al., 2013) and could not be properly visualised here. Translucent circles represent old star clusters with no active massive stars within them.

Table 2.1: List of simulations with the included feedback processes. S: Type II SNe implemented as thermal energy input. W: stellar winds implemented as radial momentum and mass injection. R: ionising UV radiation (HII regions). C: injection and transport of non-thermal CRs (10 per cent of the SN energy) at SN explosion sites.

Name	**S**upernovae	Stellar **W**inds	**R**adiation	**C**osmic rays
S	✓	×	×	×
SW	✓	✓	×	×
SWC	✓	✓	×	✓
SR	✓	×	✓	×
SWR	✓	✓	✓	×
SWRC	✓	✓	✓	✓

2.3 Morphology and global evolution

In Fig. 2.2, 2.3 and 2.4, we show the time evolution of the total gas surface density $\Sigma_{\rm gas}$ seen edge-on for the three models without radiation *S*, *SW*, and *SWC* on the left and the corresponding counterparts including radiation on the right. Models *S* and *SR* are depicted in Fig. 2.2. Fig. 2.3 shows models *SW* and *SWR*, and Fig. 2.4 models *SWC* and *SWRC*. We present the evolution from $t = 30$ Myr until the end of the simulations at $t = 100$ Myr for for the full computational domain ($0.5\,\mathrm{kpc} \times 0.5\,\mathrm{kpc} \times \pm 4\,\mathrm{kpc}$). Star formation starts after ~ 25 Myr.

The models without radiation drive the strongest outflows (left panels in Fig. 2.2, 2.3 and 2.4) due to an up to one order of magnitude higher SFR compared to their radiation counterparts (see Sec. 2.4.1). Those strong outflows can even lead to a nearly complete depletion of gas in the mid-plane like in model *S* (Fig. 2.2 left). Ionising UV radiation prevents the star clusters from accreting more gas as soon as the first stars are born, resulting in a strong regulation of star formation (see also Peters et al., 2017; Butler et al., 2017; Haid et al., 2018, for similar

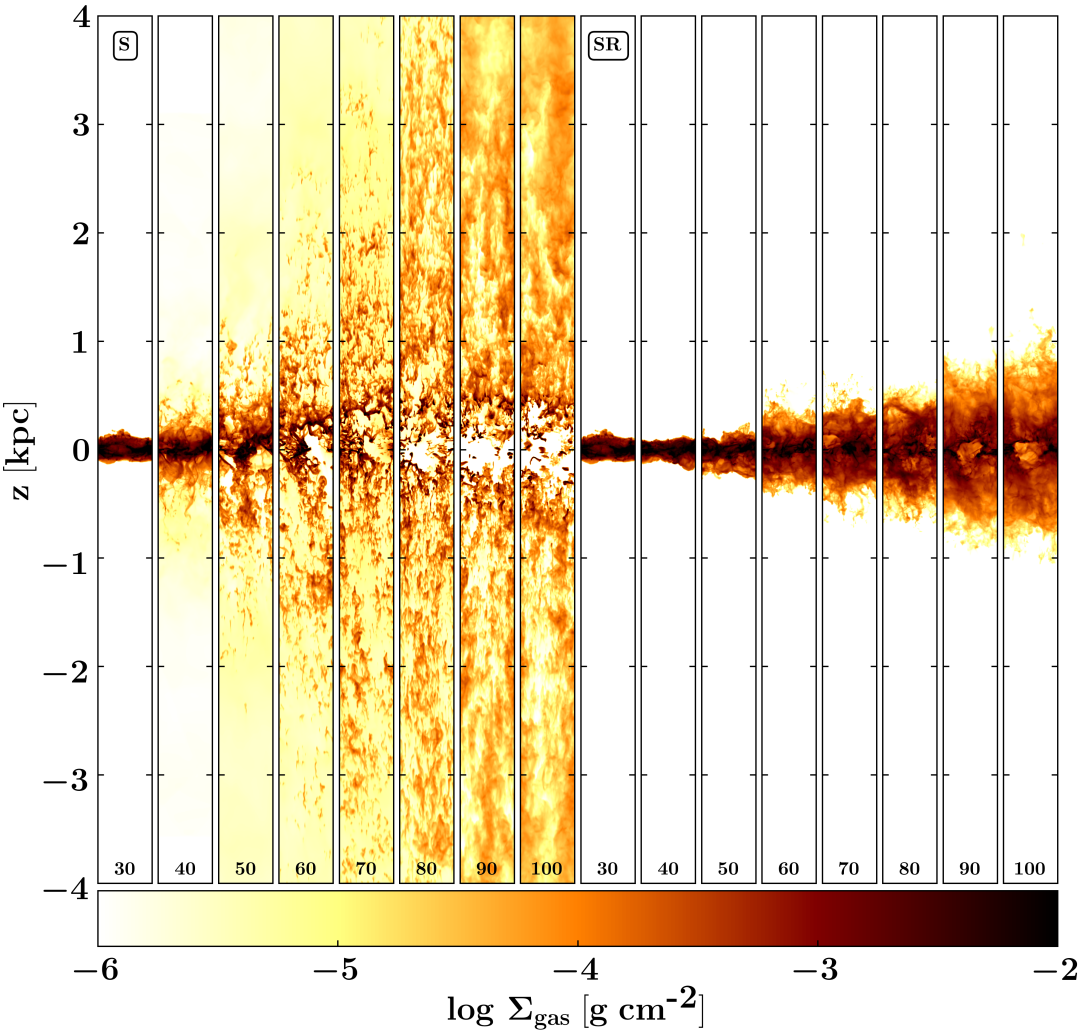

Figure 2.2: Edge-on view of the time evolution of the total gas column density for model *S* with SN-only feedback and *SR* with added ionising radiation from 30 to 100 Myr (indicated by the number at the bottom of each panel). The initial collapse triggers a starburst with strongly clustered SNe driving a highly structured outflow resulting in the dispersal of the mid-plane ISM. In longer-term evolution simulations, such a configuration might settle into a new equilibrium (Kim & Ostriker, 2017). The initial starburst is not inevitable. In our setup, it disappears if further early feedback processes from massive stars like stellar winds and radiation are included (see Fig. 2.3 and Fig. 2.4).

conclusions). This reduced SFR results in weaker outflows launched at later stages (see Sec. 2.6). CRs have a visible impact on the outflow structure during the first 100 Myr (*SWC*, left of Fig. 2.4 and *SWRC*, right of Fig. 2.4) resulting in a smoother gas distribution (see also Simpson et al., 2016; Girichidis et al., 2016b, 2018a). On this short time-scale, the additional CR pressure gradient does not result in significantly enhanced outflows as it requires some time to build up.

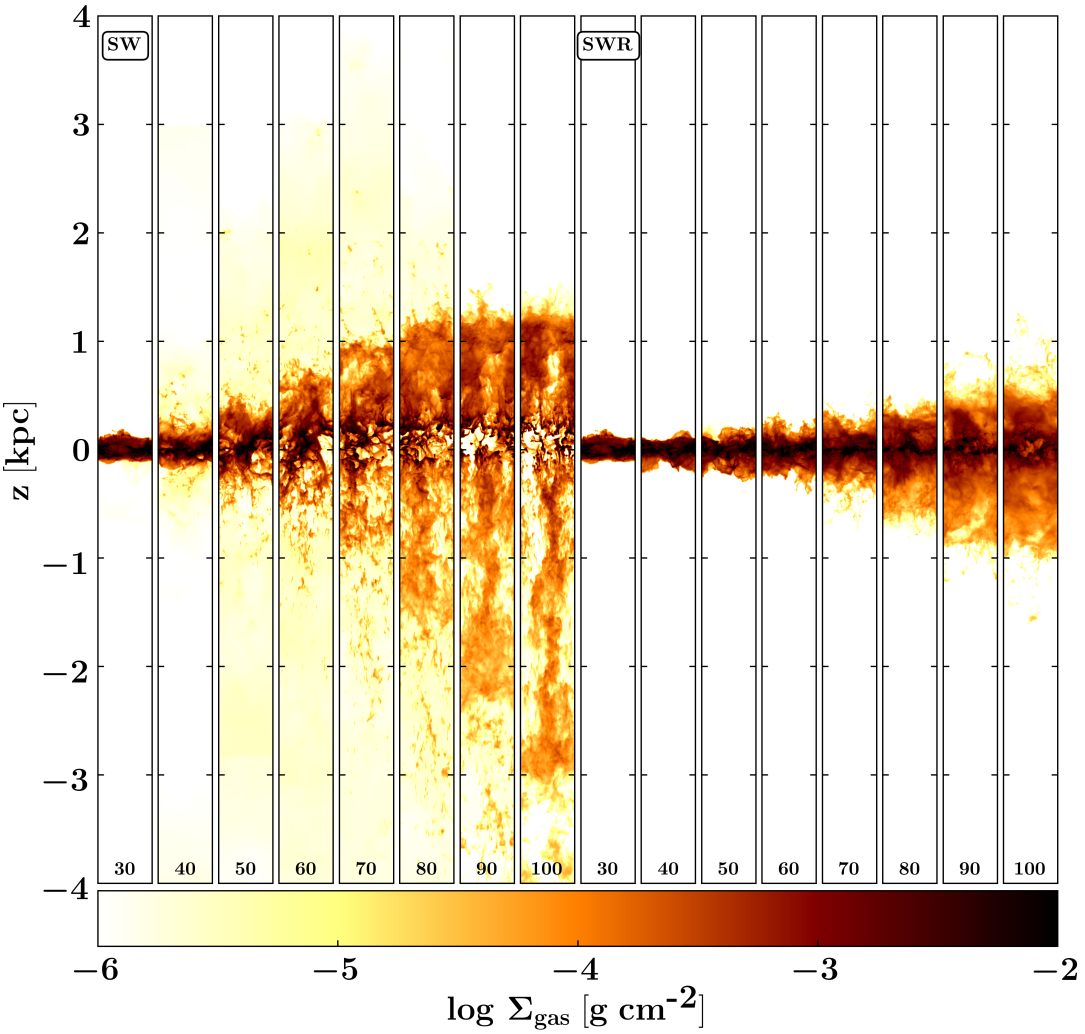

Figure 2.3: Column density time evolution for the models with added stellar winds (left, *SW*) and added winds and ionising radiation (right, *SWR*) from 30 to 100 Myr (see 2.2 for the SN-only and SN-radiation models). The inclusion of stellar winds (*SW*) reduces star formation (see Fig. 2.5) by limiting accretion onto sink particles. Including ionising radiation (*SWR*) regulates star formation even more and only weak outflows are driven.

On longer time-scales, CRs can become the dominant outflow driving mechanism as shown in Girichidis et al. (2016b). We will present the long-term evolution of simulations *SWR* and *SWRC* in Chapter 3.

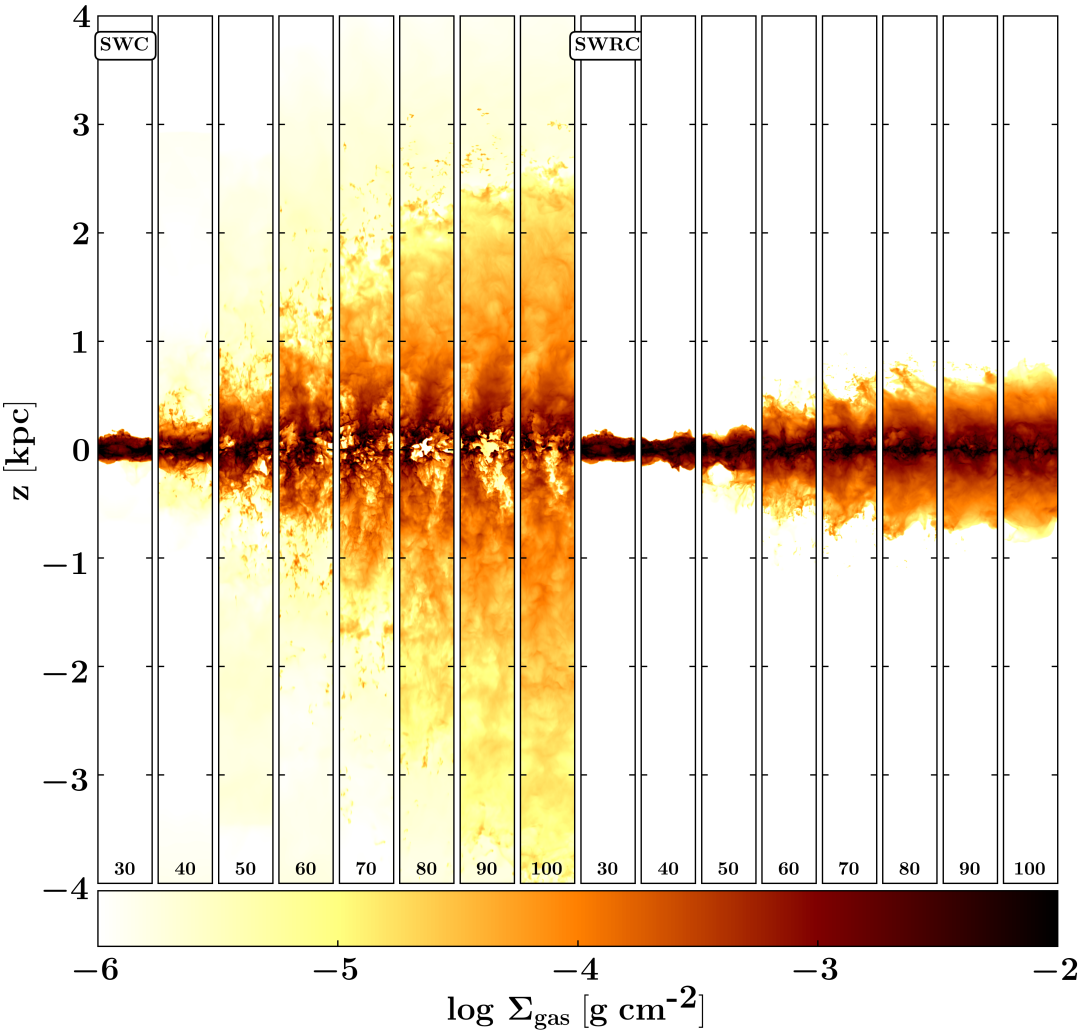

Figure 2.4: Column density time evolution for the models with added winds and CRs (left, *SWC*) and added winds, ionising radiation, and CRs (right, *SWRC*) from 30 to 100 Myr. The additional CR pressure smooths out the outflow. Overall, CRs have little effect on the mid-plane ISM in the early stages of the simulation but smooth out the gas in the outflow.

2.4 Towards a complete model of the ISM

2.4.1 Star formation

In Fig. 2.5, we show the SFR surface densities $\Sigma_{\dot{M}_\star}$ over time for the six models. The grey histograms indicate the instantaneous SFR surface densities, i.e. gas mass transformed into new stars, $\dot{M}_{\rm sink}$, in cluster i in a period of $\Delta t = 1$ Myr per kpc^2:

$$\Sigma_{\dot{M}_\star}(t) = \frac{1}{A}\sum_{i=1}^{N_{\rm sink}} \dot{M}_{\rm sink,i}, \tag{2.7}$$

for $t - \frac{\Delta t}{2} < t < t + \frac{\Delta t}{2}$ and the surface area of the mid-plane ISM $A = 0.25\,\mathrm{kpc}^2$.

The dashed line in each panel indicates a fiducial SFR surface density using the mean value of the Leroy et al. (2008) data for a H_2 + H gas surface density range of $\Sigma_{\mathrm{gas}} = 5 - 10\,\mathrm{M}_\odot\,\mathrm{pc}^{-2}$ (see Fig. 2.6 for more details). We indicate a factor 3 scatter by the shaded area. The solid black line $\overline{\Sigma}_{\dot{M}_\star}$ is the mean value of the SFR surface density averaged from $t = 25 - 100\,\mathrm{Myr}$ for each simulation respectively.

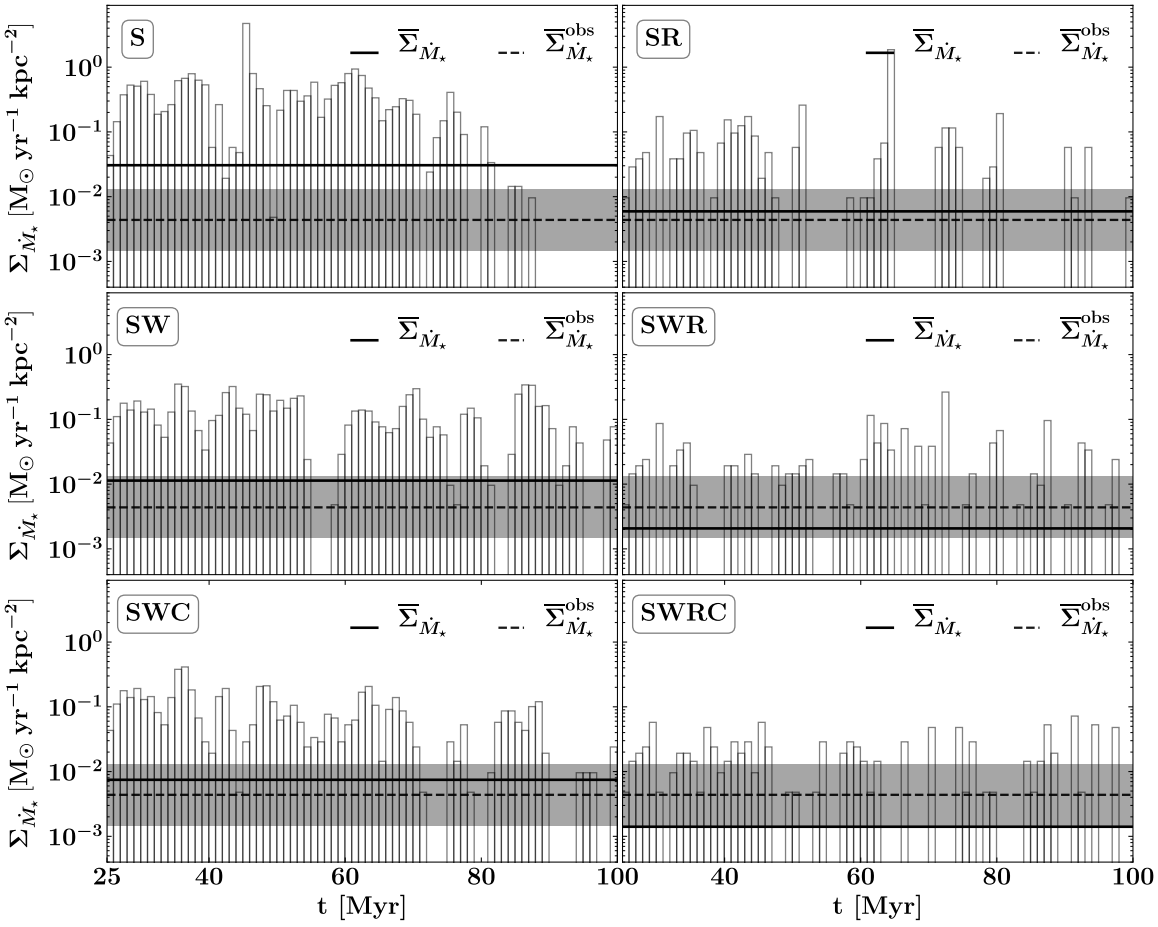

Figure 2.5: SFR surface densities $\Sigma_{\dot{M}_\star}$ for the different runs. The grey histograms indicate the instantaneous values. The solid line $\overline{\Sigma}_{\dot{M}_\star}$ is the time-averaged SFR surface density from $t = 25-100\,\mathrm{Myr}$ and the dashed black line is a mean SFR surface density for $\Sigma_{\mathrm{gas}} = 5-10\,\mathrm{M}_\odot\,\mathrm{pc}^{-2}$ from Leroy et al. (2008) (see Fig. 2.6), including a factor of 3 uncertainty shaded in light grey. The models without radiation undergo an initial starburst, whereas *SR*, *SWR* and *SWRC* (right panels) have lower SFRs comparable to observational estimates.

For the different models the average SFR surface densities $\overline{\Sigma}_{\dot{M}_\star}$ with 1σ scatter are:

$$
\begin{aligned}
&S: && \overline{\Sigma}_{\dot{M}_\star} = (3.06 \pm 2.18) \times 10^{-2} && \mathrm{M_\odot\,yr^{-1}\,kpc^{-2}}\\
&SW: && \overline{\Sigma}_{\dot{M}_\star} = (1.13 \pm 0.38) \times 10^{-2} && \mathrm{M_\odot\,yr^{-1}\,kpc^{-2}}\\
&SWC: && \overline{\Sigma}_{\dot{M}_\star} = (7.46 \pm 3.70) \times 10^{-3} && \mathrm{M_\odot\,yr^{-1}\,kpc^{-2}}\\
&SR: && \overline{\Sigma}_{\dot{M}_\star} = (5.93 \pm 4.54) \times 10^{-3} && \mathrm{M_\odot\,yr^{-1}\,kpc^{-2}}\\
&SWR: && \overline{\Sigma}_{\dot{M}_\star} = (2.07 \pm 1.06) \times 10^{-3} && \mathrm{M_\odot\,yr^{-1}\,kpc^{-2}}\\
&SWRC: && \overline{\Sigma}_{\dot{M}_\star} = (1.41 \pm 0.51) \times 10^{-3} && \mathrm{M_\odot\,yr^{-1}\,kpc^{-2}}.
\end{aligned}
$$

The model with SN-only, *S*, rapidly evolves into a starburst with an average SFR about one order of magnitude above the observationally motivated value of $\overline{\Sigma}^{\mathrm{obs}}_{\dot{M}_\star} = 4.4\times10^{-3}\,\mathrm{M_\odot\,yr^{-1}\,kpc^{-2}}$ (dashed black lines in Fig. 2.5) for a gas surface density range of $\Sigma_{\mathrm{gas}} = 5 - 10\,\mathrm{M_\odot\,pc^{-2}}$ (Leroy et al., 2008). We chose this range in gas surface density because it represents the upper and lower limits of average gas surface densities in our simulations. Due to the lack of early feedback processes from massive stars, gas can be accreted by the cluster sinks until the first SNe explode (Gatto et al., 2017; Peters et al., 2017). For this simulation, the median cluster mass is $M_{\mathrm{median}} = 1.6 \times 10^4\ \mathrm{M_\odot}$ with an average number of $\overline{N}_\star = 184$ massive stars per cluster (see Table 2.2). The highly clustered SNe drive a strong outflow and the mid-plane star-forming ISM completely disperses (see Fig. 2.2, left panel). Therefore star formation is terminated by the depletion and dispersal of the cold gas reservoir during the last ~ 15 Myr of model *S*. The SFR of model *SW* is lower than in model *S* by about a factor of 3. All three non-radiation models lie above the observationally motivated value.

For the radiation runs *SR*, *SWR* and *SWRC* the behaviour is qualitatively different. The SFR surface density is about a factor of 5 lower than for the respective runs without radiation and agrees with observational expectations. While the initial starburst is already slightly suppressed in models *SW* and *SWC* by the early feedback in form of stellar winds, it is absent in the radiation runs *SR*, *SWR* and *SWRC*. Comparing *SW*, *SR* and *SWR*, the SFR drops by nearly one order of magnitude when adding the radiation but only by about a factor of ~ 2.5 when adding winds. Thus, ionising UV radiation seems more important for quenching the SFR than stellar winds, at least for the models at ~ 4 pc resolution presented here. Those findings qualitatively agree with earlier studies (Butler et al., 2017; Peters et al., 2017) on this topic and also higher resolution simulations on smaller scales (see e.g. Dale et al., 2014; Geen et al., 2015, 2017; Haid et al., 2018). CRs do not directly impact the gas structure of the disc and the accretion behaviour of the sink particles. The ISM is still dominated by the thermal and kinetic gas pressures and the strongest impact of the CRs is seen only in the outflow region.

In Fig. 2.6, we compare the gas surface densities $\Sigma_{\mathrm{H+H_2}}$ and SFR surface densities $\Sigma_{\dot{M}_\star}$ of our models with spatially resolved observations from local star-forming spiral- and dwarf-galaxy patches (light grey dots, Leroy et al. (2008)). The dashed black line is the Kennicutt-Schmidt relation (KS-relation) $\Sigma_{\dot{M}_\star} \propto \Sigma^{1.4}_{\mathrm{H+H_2}}$ (Kennicutt, 1998) centred on the average SFR surface density for gas surface densities $\Sigma_{\mathrm{gas}} = 5 - 10\,\mathrm{M_\odot\,pc^{-2}}$ with $\overline{\Sigma}^{\mathrm{obs}}_{\dot{M}_\star} = 4.4\times10^{-3}\,\mathrm{M_\odot\,yr^{-1}\,kpc^{-2}}$. This range in gas surface densities is chosen because it represents the upper and lower limits of the averaged gas surface densities in our simulations. Shown are the averaged values of our models from $t = 25 - 100$ Myr, with the error bars indicating 1σ scatter. Including early feedback processes in the form of stellar winds (*SW*) and, in particular, radiation (*SR*) reduces the SFRs, resulting

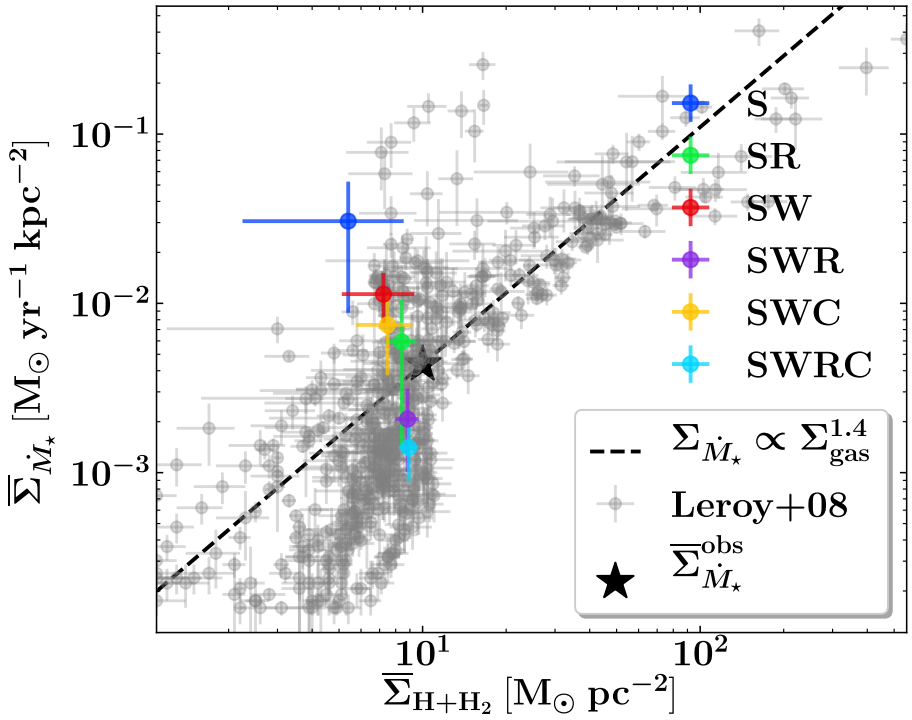

Figure 2.6: SFR surface densities vs. gas surface densities of the atomic and molecular hydrogen gas in the disc ($z = \pm 250$ pc), averaged over $t = 25 - 100$ Myr with 1σ scatter. The black dashed line indicates a Kennicutt-Schmidt relation (Kennicutt, 1998) slope of $\Sigma_{\dot{M}_\star} \propto \Sigma_{\rm gas}^{1.4}$. The grey dots are observational data from spatially resolved patches of nearby star-forming galaxies (Leroy et al., 2008). The black star indicates an average star formation rate value for gas surface densities $\Sigma_{\rm gas} = 5 - 10\,{\rm M}_\odot\,{\rm pc}^{-2}$ of $\overline{\Sigma}^{\rm obs}_{\dot{M}_\star} = 4.4 \times 10^{-3}\,{\rm M}_\odot\,{\rm yr}^{-1}\,{\rm kpc}^{-2}$. The SN-only run (*S*) has a very high SFR for its gas surface density. Models including winds (*SW*, *SWC*) and, in particular, radiation (*SR*, *SWR*, *SWRC*) are closer to most observational values.

in values more consistent with the mean value derived from observations (Leroy et al., 2008). CRs (*SWC* and *SWRC*) have a weak additional impact and only slightly reduce the SFR. We note that around a gas surface density of $\Sigma_{\rm gas} \sim 10\,{\rm M}_\odot\,{\rm pc}^{-2}$ the observations show an enormous range of star formation rates covering ~ 3 orders of magnitudes. Therefore models for higher surface densities might provide stronger physical constraints (see e.g. Gong et al., 2020).

In Fig. 2.7 we show the average depletion times $\overline{\tau}_{\rm depl} = \overline{\Sigma}_{\rm cold} \times \overline{\Sigma}^{-1}_{\dot{M}_\star}$ of the simulated cold gas phase ($T < 300$ K) against the average cold phase gas surface density $\overline{\Sigma}_{\rm cold}$ in the mid-plane $z = \pm 250$ pc. The observational data from Leroy et al. (2008) shows gas depletion times for molecular H_2 gas. The dashed black line indicates a constant depletion time of $\tau_{\rm depl} = 2$ Gyr as favoured by observations (Bigiel et al., 2008).

For our models, we find depletion times ranging from 0.19 Gyr in *S* to 5.02 Gyr in *SWRC*. The two other models including radiation *SR* and *SWR* exhibit average depletion times of 1.19 Gyr

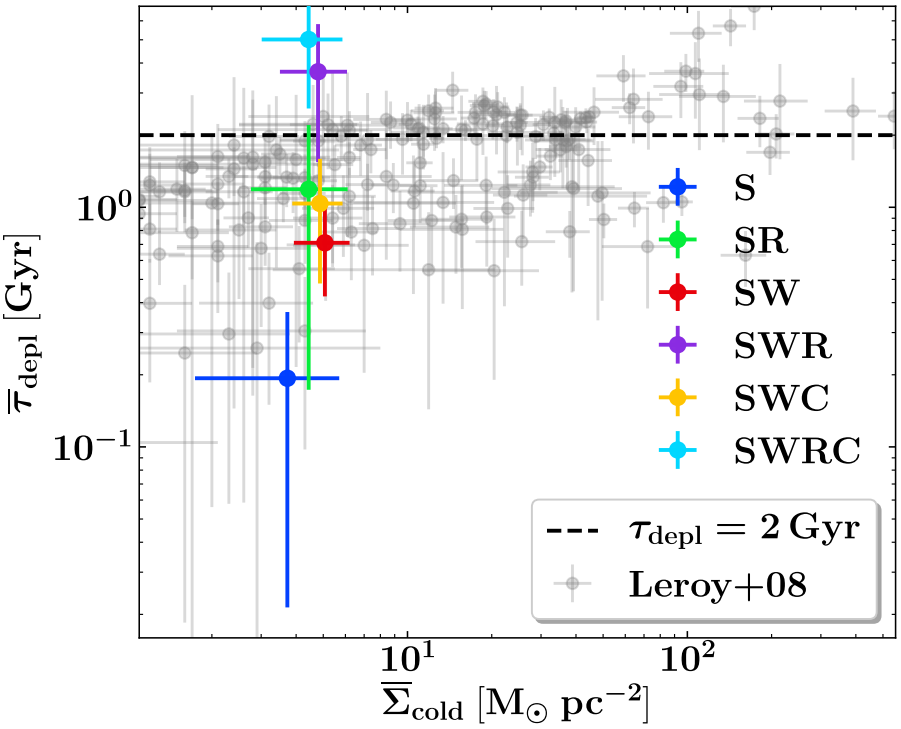

Figure 2.7: Average gas depletion times $\overline{\tau}_{\rm depl}$ of the cold gas phase ($T < 300$ K) vs. average gas surface densities of the cold phase $\overline{\Sigma}_{\rm cold}$ with 1σ scatter. The time averages are taken from $t = 25 - 100$ Myr. The horizontal dashed line indicates a constant depletion time of $\tau_{\rm depl} = 2$ Gyr. The grey dots are observed depletion times for molecular gas H_2 from Leroy et al. (2008).

and 3.68 Gyr, respectively. The two wind models without radiation (*SW* and *SWC*) have cold gas depletion times around 0.7 – 1.0 Gyr. A constant molecular gas depletion time, as suggested by the observations, indicates a linear relationship between the molecular gas surface density Σ_{H_2} and SFR surface density $\Sigma_{\dot{M}_\star}$, i.e. a constant efficiency of transforming molecular gas into stars. Bigiel et al. (2008) find a constant molecular gas depletion time of $\tau_{\rm depl} = 2$ Gyr with a rms scatter of 0.8 Gyr for a sample of 18 nearby galaxies, measured over a Σ_{H_2} range of $\sim 3 - 50\,M_\odot$ pc^{-2} (shown as black dashed line in Fig. 2.7). Our most realistic models including early feedback from ionising UV radiation and stellar winds (*SWR* and *SWRC*) lie remarkably close to the constant depletion time of 2 Gyr inferred by observations. Our SN-only model *S* shows a depletion time of ~ 200 Myr at the lower bound of the observational scatter. In *S*, star formation is fully quenched after ~ 90 Myr (see Fig. 2.5) and the gas reservoir is completely used up at later stages (see also the *holes* in the mid-plane gas column density in the left panel of Fig. 2.2). This indicates that the SFR is regulated by the galactic outflow, instead of depletion of the cold gas phase via star formation.

We show the depletion times for the cold gas instead of presenting it for the H_2, which is included in our chemical network. The reason for this is that the H_2 formation is likely not fully converged at our spatial resolution of $\Delta x \approx 4$ pc. The cold gas phase is the regime where

molecular gas would form and is used as a proxy for estimating the molecular gas surface density Σ_{H_2}. We might be over-estimating Σ_{H_2} with this assumption, which would hence result in a too large estimate for the depletion times.

2.4.2 Star cluster properties

Massive stars in galaxies are believed to form hierarchically, embedded in dense molecular clouds and young massive clusters (Lada & Lada, 2003; Portegies Zwart et al., 2010; Grasha et al., 2017). Fig. 2.8 shows the accretion properties of the star cluster sink particles formed in our simulations. We show the maximum accretion time-scale $\tau_{\rm accr}$ defined as the time each cluster takes to reach its respective maximum mass $M_{\rm max}$ through accretion against $M_{\rm max}$. Lower mass clusters ($M_{\rm max} < 120\,{\rm M}_\odot$, indicated by the dashed vertical line in Fig. 2.8) do not accrete enough gas to form massive stars and have no active feedback channel. Their accretion properties are solely determined by the availability of gas in their natal environment. The data-points indicated by crosses come from a high-resolution simulation done by Haid et al. (2019), which are part of the SILCC-Zoom project (see e.g. Seifried et al., 2017, for details about the zoom-in simulations). Haid et al. (2019) take two self-consistently formed molecular clouds (MC) from the first set of the SILCC simulation suite (Walch & Naab, 2015; Girichidis et al., 2016b) which have been identified in Seifried et al. (2017) and re-calculate the central part (a cube with side length $l = 40\,{\rm pc}$) at a resolution of $\Delta x \approx 0.122\,{\rm pc}$. They run two sets of simulations for each identified MC one without any form of feedback (labelled here as ZI:no-fb), equivalent to our model *S*, and one with ionising UV radiation (labelled here as ZI:R), equivalent to our model *SR*. We group the stars and sub-clusters formed in each MC together as one cluster and plot the mass-weighted average accretion time against the average maximum mass of those clusters. Being part of the same framework, Haid et al. (2019) use the same methods for radiative transfer (TreeRay Wünsch et al. (2021)), the same time-dependent chemical network, including heating and cooling, and the same sink particle creation and accretion mechanisms, albeit with different parameters. Their accretion radius is $r_{\rm accr} = 0.31$ pc (corresponding to $2.5 \times \Delta x$) and their density threshold is $n_{\rm sink} \approx 5 \times 10^3\,{\rm cm}^{-3}$.

Stellar feedback has a strong influence on the overall formation of the star clusters. Without continuous feedback (model *S*), the clusters become significantly more massive but the total number of formed star clusters $N_{\rm cluster}$ is slightly lower than in models with wind and radiation. Wind feedback can push down the median cluster mass $M_{\rm median}$ and the average number of massive stars in each cluster $\overline{N}_\star$ by a factor of ~ 3. The strongest effect, however, is seen in the models including ionising radiation. The clusters are remarkably lighter with the most massive one in model *SWRC* nearly 50 times less massive than in model *S*. The average number of massive stars per cluster drops from $\overline{N}_\star = 184$ in simulation *S* to only $\overline{N}_\star = 6$ in model *SWRC*. The maximum accretion time-scale $\tau_{\rm accr}$ is limited by the lifetime of the most massive star in a cluster after it undergoes a supernova explosion if no other feedback channels are included. Stellar winds only have a limited impact on the accretion time-scale. When radiative feedback is not included, the accretion time-scales do not depend on the total accreted mass, with only a few outliers. This trend is similar to results from higher resolution zoom simulations of individual molecular clouds (Haid et al., 2019). Cosmic rays seem to not play a role in cluster formation since the differences

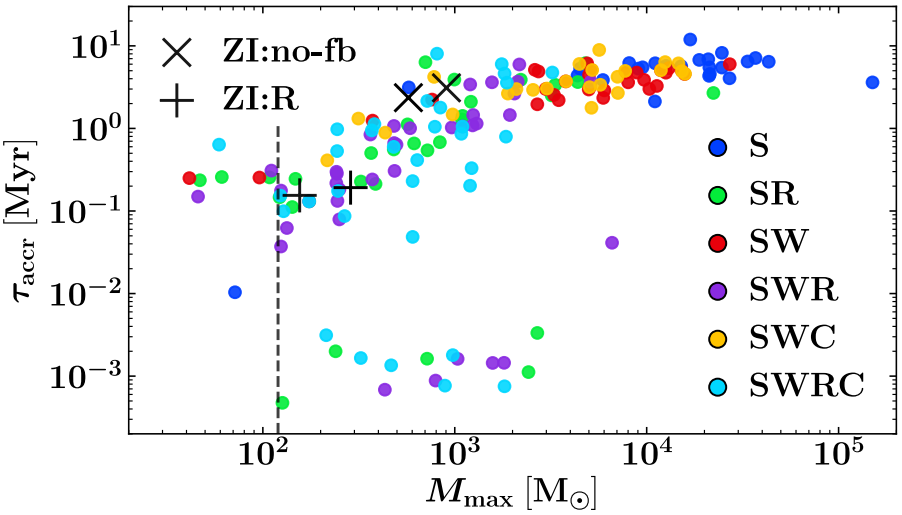

Figure 2.8: Maximum accretion time-scale $\tau_{\rm accr}$ of the star cluster sink particles against the maximum accreted mass $M_{\rm max}$ of each cluster sink in the simulations. The black crosses are from molecular cloud zoom-in simulations with a resolution of $\Delta x = 0.112$ pc (Haid et al., 2019), incorporating the same methods for radiative transfer, chemistry and sink particle creation as we do in this study. Without ionising radiation feedback, a slightly lower number of significantly more massive clusters are formed, with longer accretion times (see also Table 2.2). The dashed black vertical line indicates a cluster mass of 120 M$_\odot$. We form a handful of star cluster sink particles with $M_{\rm max} < 120\,{\rm M}_\odot$. Those clusters do not host massive stars and do not contribute feedback. Inherently, there is no lower mass limit for the star cluster sink particles we form.

between *SW* and *SWC*, as well as *SWR* and *SWRC* are negligible. Early stellar feedback strongly suppresses clustering (see also recent results from Hu et al., 2017; Smith et al., 2020), which also inhibits the formation of the super-bubbles needed to generate a volume-filling hot gas phase as discussed in the next sections. Our result that radiative feedback plays the most crucial role in regulating cluster formation and star formation properties is also found in other studies by e.g. Murray et al. (2010); Dale et al. (2012); Howard et al. (2017); Peters et al. (2017). We want to note that the effect of feedback does not change on smaller scales (compare with the Haid et al. (2019) data in Fig. 2.8) and the choice of sink particle accretion parameters does not qualitatively change the outcome. The properties of the star cluster sink particles, as well as the percentage of unresolved SNe with momentum injection $f_{\rm mom}$ are listed in Table 2.2.

In Fig. 2.9 we show the star cluster sink mass distribution normalised to the total number of clusters formed in each model. To improve readability, we split the six models into three panels, each panel grouping together the respective models with and without ionising UV radiation. The grey shaded histograms represent observational data of 114 open clusters in the solar neighbourhood ($d < 600$ pc) taken out of a catalogue of 520 Galactic open clusters (Kharchenko et al., 2005). The sharp cut-off at the low mass end of the distribution suggests a complete sample for clusters more massive than $M \gtrsim 10^2\,{\rm M}_\odot$, however, this sample includes clusters with age

Table 2.2: Star cluster sink properties of the six models. We list the mass of the most massive cluster sink formed $M_{\rm cl}$, the median mass of the formed cluster sinks when they stopped accreting $M_{\rm median}$, the median accretion time-scale of the cluster sinks $\tau_{\rm accr}$, the total number of formed cluster sinks $N_{\rm cluster}$, and the average number of massive stars per cluster sink $\overline{N}_{\star}$, computed as the total number of massive stars formed divided by the total number of cluster sinks formed. The percentage of unresolved SNe with momentum injection $f_{\rm mom}$ is given in the last column. Radiation feedback inhibits clustering and drastically reduces the median and maximum mass of the star cluster sinks, preventing the formation of super-bubbles and resulting in less effective SNe.

Run	$M_{\rm cl}$ [$M_\odot$]	$M_{\rm median}$ [$M_\odot$]	$\tau_{\rm accr}$ [Myr]	$N_{\rm cluster}$	$\overline{N}_{\star}$	$f_{\rm mom}$ [%]
S	1.5×10^5	1.6×10^4	5.39	26	184	5.3
SW	2.7×10^4	5.1×10^3	3.62	30	59	6.9
SWC	1.6×10^4	5.1×10^3	3.79	24	48	7.5
SR	2.2×10^4	7.1×10^2	1.39	30	15	5.9
SWR	6.6×10^3	5.0×10^2	0.98	37	8	4.2
SWRC	3.2×10^3	6.4×10^2	1.25	33	6	5.3

estimates between a few Myr to a few 10^3 Myr, way older than the total simulated time in our models. We do not incorporate any cluster disruption mechanisms in our simulations, so the comparison of our data to the observational data is mostly qualitative. The small number of clusters formed in our models ($N_{\rm cluster} \sim 30$) does not allow us to meaningfully sample a cluster mass function. Nonetheless, there is a clear trend of forming too massive clusters, atypical for the local solar neighbourhood, when omitting ionising UV radiation.

2.4.3 The importance of supernova ambient densities

The ambient ISM densities at SN sites are of fundamental importance for their local and global dynamical and thermal impact (Naab & Ostriker, 2017). At high environmental densities, the imparted SN energy is rapidly cooled away and the energy and momentum coupling to the ambient gas is very low (Gatto et al., 2015; Walch et al., 2015; Kim & Ostriker, 2015; Haid et al., 2016). For low ambient densities radiation losses are minor and super-bubbles (Mac Low & McCray, 1988; Wünsch et al., 2008) with a high hot gas VFF can be created by consecutive and spatially overlapping SN events (Mac Low & McCray, 1988; Creasey et al., 2013; Fielding et al., 2017). This will significantly support the driving of outflows from the ISM (see e.g. Li & Bryan, 2020). Numerical experiments by Walch et al. (2015) and Girichidis et al. (2016a) have shown that it makes a qualitative difference whether SNe at a fixed rate, i.e. with the same total energy input, explode at density peaks or random positions in the medium. Of course, ambient densities can be affected by the highly non-linear interaction of SNe, stellar winds, ionising radiation and clustering (Kim et al., 2011; Hennebelle & Iffrig, 2014; Li et al., 2015; Walch et al., 2015; Girichidis et al., 2016a; Gatto et al., 2017; Naab & Ostriker, 2017; Hu et al., 2017; Rahner et al., 2017; Fielding et al., 2018; Haid et al., 2018, 2019; Rahner et al., 2019; Smith et al., 2020).

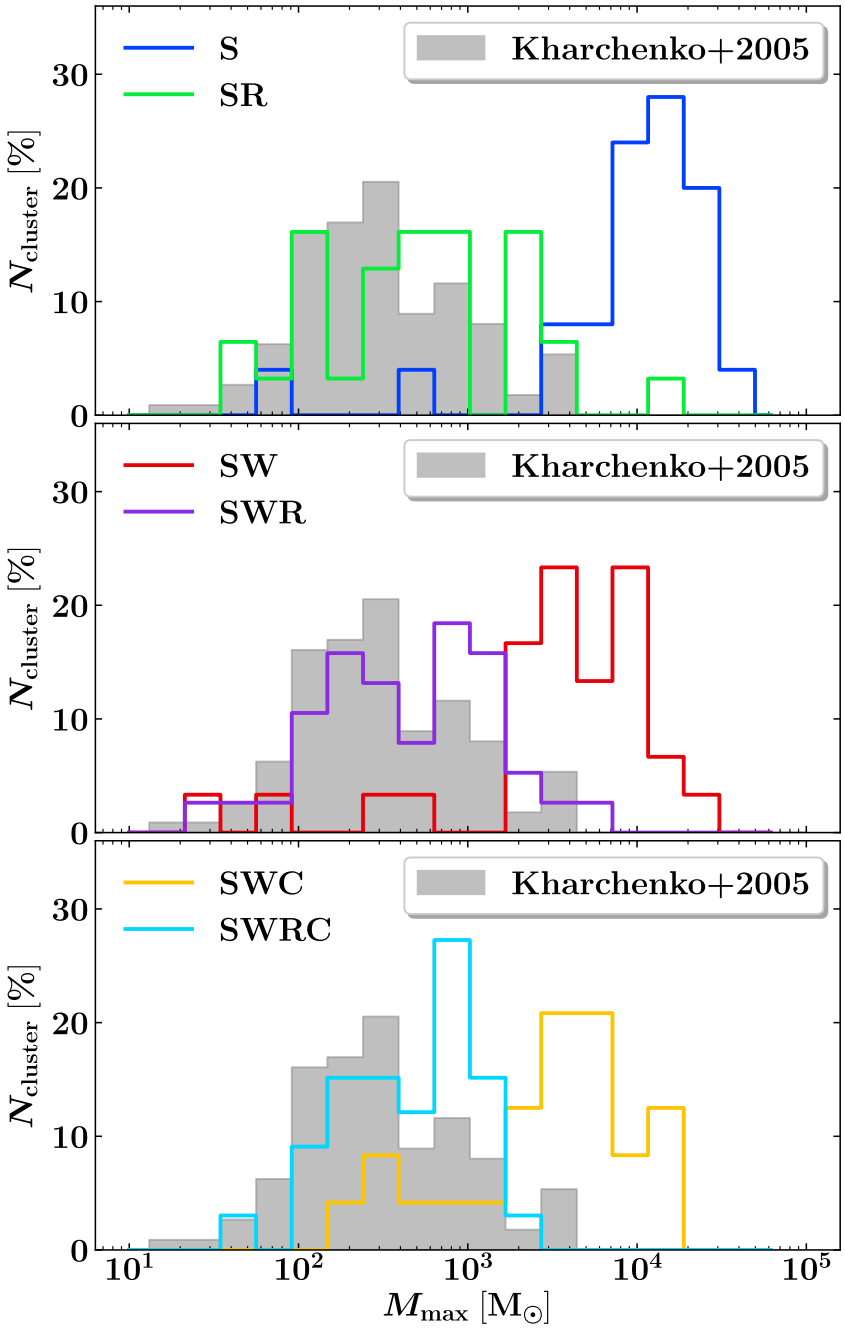

Figure 2.9: Histograms of the cluster sink mass distributions for the six models. For better readability, we split the depiction into three panels. The grey shades histograms come from observational data of 114 open star cluster in the solar neighbourhood ($d < 600$ pc) by Kharchenko et al. (2005). Without the accretion limiting effects of ionising UV radiation, the star clusters grow to masses greater than 10^4 $\mathrm{M}_\odot$, atypical for the solar neighbourhood.

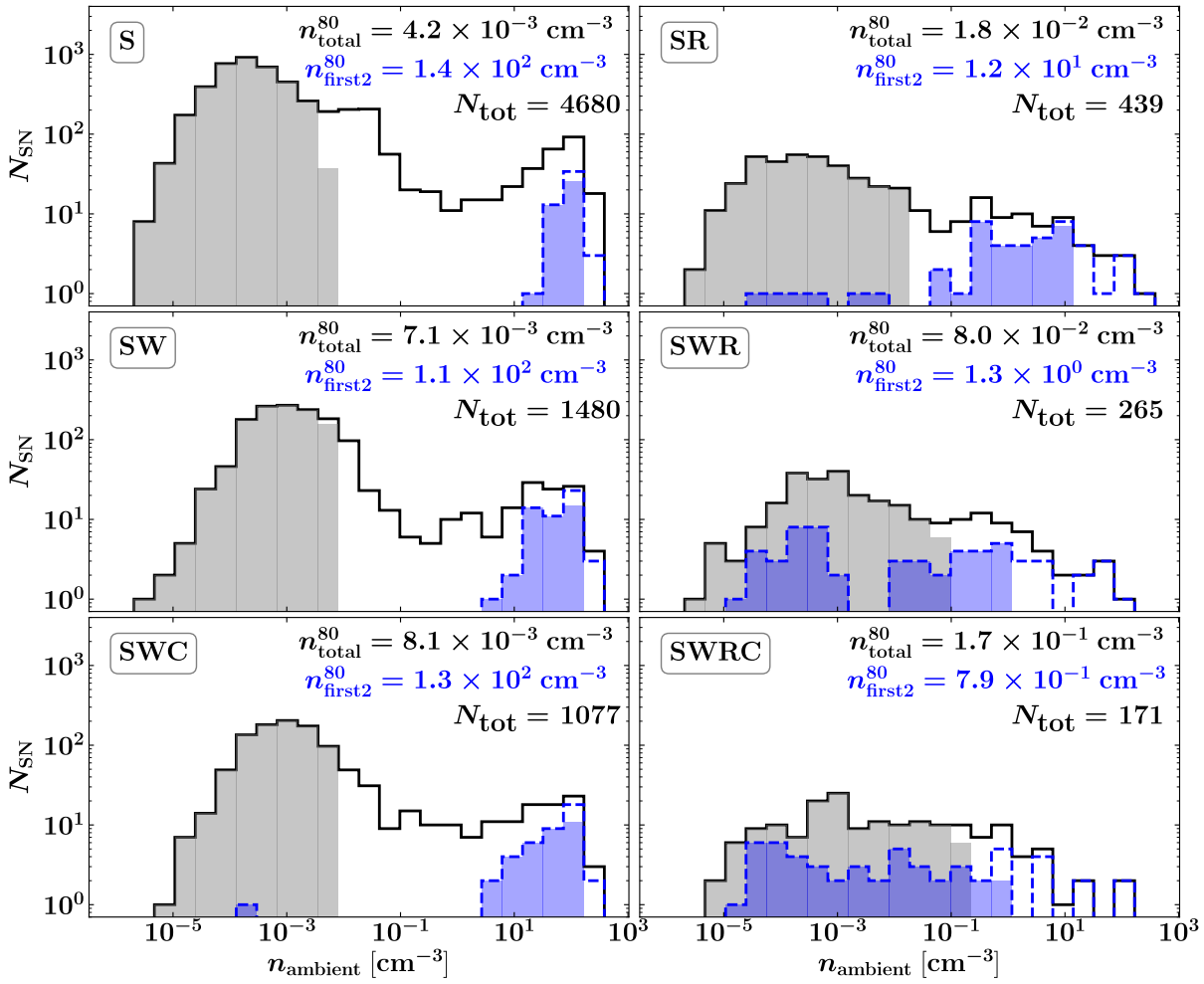

Figure 2.10: Distribution of the ambient gas densities at SN explosion sites. Shaded in grey are the histograms including 80 per cent of all SNe exploding at the lowest densities up to corresponding densities $n^{80}_{\rm total}$ given in the respective panels. The blue dashed histograms indicate the densities of the first two SNe in each star cluster sink, with the respective histograms including 80 per cent of the first two SNe per star cluster sink shaded in blue. For SN-only (*S*) the ambient density distribution is bi-modal, which is a clear sign of strong clustering. Most SNe explode in low-density bubbles created by previous events, 80 per cent of all SNe explode at ambient densities below $\sim 4 \times 10^{-3}\,\mathrm{cm}^{-3}$ (grey histogram). For runs without radiation (*S*, *SW*, *SWC*) the first SNe of a cluster always explode at high ambient densities $\sim 20 - 200\,\mathrm{cm}^{-3}$ (blue dashed histograms). The high-density peak disappears with the inclusion of radiation (*SR*, *SWR*, *SWRC*, right panels) and the distributions become flatter. While most SNe now explode at densities below $\sim 0.18\,\mathrm{cm}^{-3}$ the SN rate has dropped by a more than one order of magnitude. This highlights the complex interplay between SFR, clustering and feedback. In reality, however, all processes are at work as realised in model *SWRC* (bottom right panel).

In Fig. 2.10, we present the ambient ISM densities at the type II SN explosion sites for the six models. Those densities are computed as the average density of the gas cells within the SN injection radius ($r_{\rm inj} = 3 \times \Delta x \sim 11.7$ pc). We want to point out again that we do not change the gas structure within those cells. Any density fluctuations before the injection of the thermal SN energy are retained (see Sec. 2.1). In the left panels, we show the runs without radiation and in the right panels the respective runs with radiation. The runs without radiation show clear bi-modal ambient density distributions with early SNe typically exploding at high densities similar to the star formation threshold $n_{\rm sink} = 10^3\,{\rm cm}^{-3}$. To highlight this, the blue dashed histograms indicate the ambient densities of the first two SNe in each cluster, which are typically high for *S*, *SW*, and *SWC* at around $\sim 20 - 200\,{\rm cm}^{-3}$. At such high densities, radiation losses are significant for the first SNe in each cluster. The strong clustering (e.g. 184 massive stars per cluster on average in simulation *S*, (see Table 2.2), however, less subsequent SNe explode in previously created bubbles, resulting in very low ambient densities creating the low-density peak.

This is indicated by the grey shaded histograms, which include 80 per cent of all low-density SNe up to their limiting density of $n^{80}_{\rm ambient}$. This density is below $\sim 10^{-2}\,{\rm cm}^{-3}$ for all simulations without radiation. The SN-only run *S* has by far the highest SNR, as well as the broadest distribution with a double-peaked shape. The total number of SNe gets reduced by a factor of ~ 3.7 by the stellar winds (models *SW* and *SWC*). The overall shape of the distribution is, however, very similar to model *S* and the first SNe still explode only at the highest densities. Adding cosmic rays (*SWC*) does not change this feature.

The ambient density distribution changes qualitatively with the inclusion of radiation (*SR, SWR, SWRC*, in the right panels of Fig. 2.10). The bi-modal nature disappears and due to the creation of lower density HII regions already the first SNe can explode in much lower ambient density environments. This is highlighted with blue dashed histograms in the right panels of Fig. 2.10. One might assume that the early creation of HII regions results in even lower density for subsequent supernova explosions. This, however, is not the case as for all radiation models the cluster masses and number of massive star per cluster is significantly reduced. For example, the radiation run *SR* has ~ 15 massive stars per cluster compared to 184 massive stars per cluster in simulation *S* (see Table 2.2). As a result of this strongly reduced clustering less SNe explode in previously created bubbles, which - somewhat counter-intuitively - increases $n^{80}_{\rm ambient}$ by about one order of magnitude compared to the respective simulation without radiation (see Hu et al., 2017, for similar trends in a high-resolution dwarf galaxy simulation). The fraction SNe realised with only momentum injection (unresolved Sedov blast waves at high ambient densities) is below ~ 7.5 per cent for all simulations and never drops below 4.0 per cent (*SWR*, see Table 2.2).

2.5 ISM structure

In Fig. 2.11, we compare the volume-filling factors (VFFs) and mass fractions (MFs) of the mid-plane ISM of our simulations within $z = \pm 250$ pc. We separate the gas into a cold phase ($T \leq 300$ K), a warm phase ($300\,{\rm K} < T \leq 3 \times 10^5$ K), and a hot phase ($T > 3 \times 10^5$ K). The warm phase we further divide into neutral and ionised gas based on the ionisation degree in the simulation cells. The last column in each panel give observational estimates for the solar

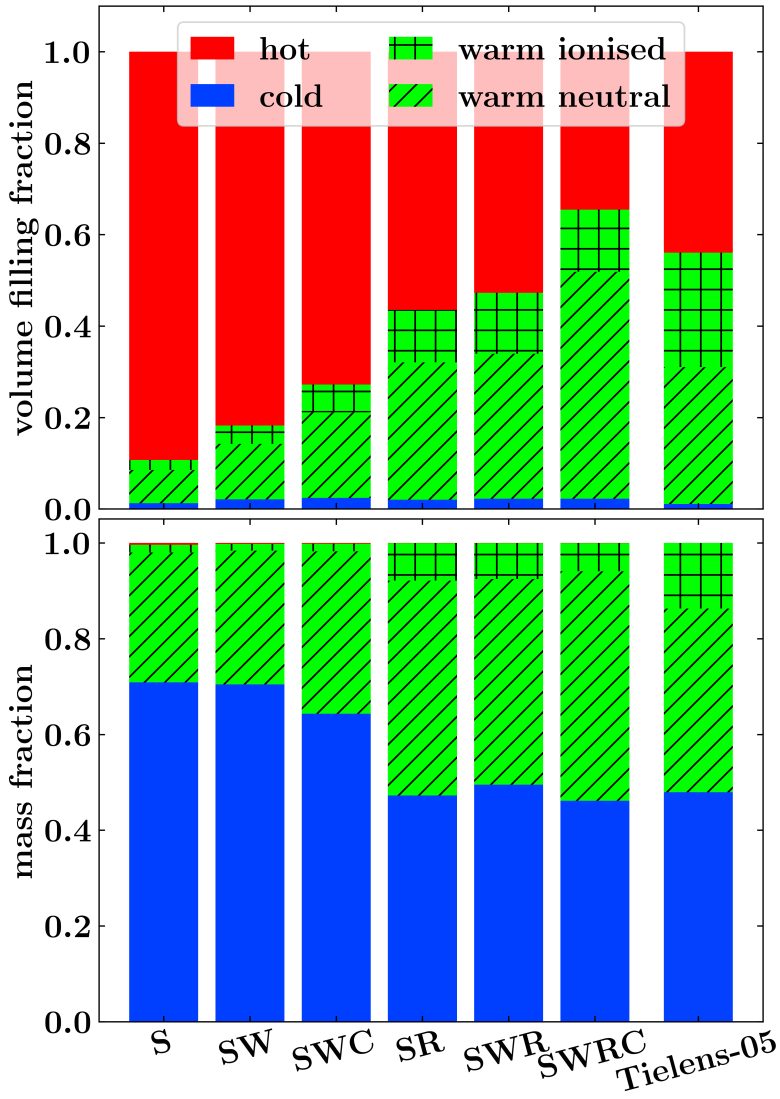

Figure 2.11: Volume-filling factors (VFF, top panel) and mass fractions (MF, bottom panel) of the mid-plane ISM ($z = \pm 250$ pc) for the cold phase ($T_{\rm cold} \leq 3 \times 10^2$ K), the warm phase (3×10^2 K $< T_{\rm warm} \leq 3 \times 10^5$ K), and the hot phase ($T_{\rm hot} > 3 \times 10^5$ K) for all six simulations. The values are time averages from $t = 25 - 100$ Myr. The warm gas phase is separated into neutral gas (diagonal shading) and ionised gas (chequered). Observational estimates for the solar neighbourhood ISM are given in the last columns (Tielens, 2005). The simulation *S* with only SN feedback has the highest hot gas volume-filling factor ~ 90 per cent. The inclusion of radiation strongly increases the VFF of the warm gas phase, also by adding photo-ionised gas, at the expense of the hot gas VFF. The inclusion of CRs further increases the warm gas VFF slightly. The cold gas MFs in runs including radiation are lower by $\sim 10 - 20$ per cent compared to their non-radiation counterparts and agree better with observational estimates.

neighbourhood ISM as stated in Tielens (2005). The VFFs and MFs are temporally averaged over $t = 25 - 100$ Myr. All values are listed in Table 2.3.

Overlapping SN remnants are the main agent for creating the hot gas phase and therefore the volume of the simulation with only SNe (*S*) is dominated by hot gas. The addition of stellar winds and CRs increases the VFF of warm gas up to ~ 25 per cent, with a small (~ 6 per cent) contribution of collisionally ionised warm gas. Ionising radiation has the strongest impact on the mid-plane ISM. Resulting from recombined gas which was ionised in HII regions, the warm gas volume-filling factors increase by a factor ~ 3 compared to the respective simulations without radiation. The volume of the hot phase is reduced accordingly. This leaves the hot gas with a VFF of about 35-55 per cent which is also in line with observations and observation-based models (Ferrière 2001; Kalberla & Kerp 2009 and references therein). Estimates of the cold gas volume-filling factors ($\mathrm{VFF_{cold}}$) are more controversial, ranging from $\mathrm{VFF_{cold}} \sim 5 - 18$ per cent for the mid-plane ISM (Kalberla & Kerp, 2009) down to $\mathrm{VFF_{cold}} \sim 1$ per cent (Tielens, 2005).

Ionising UV radiation has also the strongest impact on the mass fractions of the ISM (MF, the lower panel of Fig. 2.11). The total warm gas MF increases from $\sim 30 - 35$ per cent in non-radiation runs to $\sim 50 - 55$ per cent in the radiation runs *SR*, *SWR*, *SWRC*. The warm ionised MF increases by a factor $\sim 4 - 5$ and the warm neutral gas MF by a factor ~ 1.5. The gas reservoir for the increased mass of warm gas is the cold phase, which gets heated by the introduction of radiative feedback from massive stars. The cold mass fraction therefore decreases from ~ 70 per cent to ~ 50 per cent. CRs slightly decrease the cold gas MF by ~ 5 percentage points in *SW* down to ~ 65 per cent in *SWC*. A similar, albeit weaker, trend can also be seen in the comparison of *SWR* and *SWRC*. The additional CR pressure smooths out the gas (very clearly seen in the outflow structure in Fig. 2.4, left panels), which prevents - to some extent - the creation of cold gas clumps. Instead, the gas is kept in a warm, diffuse regime. Stellar winds do not impact the mass budget of the ISM. The addition of early wind feedback does not significantly change the MFs between *S* and *SW*, or *SR* and *SWR*. The mass in the hot phase is negligible in all models, as well as in observationally motivated estimates. Our models including radiation (*SR*, *SWR*, *SWRC*) are in good agreement with observations, whereas the models without radiation (*S*, *SW*, *SWC*) over-estimate the cold gas MFs, while under-estimating the warm ionised MFs.

We list the average kinetic, thermal, magnetic, and CR energy densities of the mid-plane ISM in Table 2.4 and compare to observational estimates summarised in Draine (2010) and references therein. Direct magnetic field strength measurements of the star-forming ISM via the Zeeman effect are only feasible in the dense ($n \gtrsim 10\,\mathrm{cm^{-3}}$) and cold neutral medium (see e.g. Heiles & Troland, 2005; Crutcher & Kemball, 2019). To better compare with observations, we therefore only average the magnetic energy densities over the atomic hydrogen gas below $T_{\mathrm{cold}} = 300\,\mathrm{K}$ in our mid-plane region. The kinetic, thermal and cosmic ray energy densities are volume-weighted over the full mid-plane ($|z| = 250\,\mathrm{pc}$). Overall, the simulations including ionising UV radiation result in kinetic, thermal, and CR energy densities comparable to local neighbourhood ISM conditions. With only SNe (*S*), the ISM is dominated by the hot phase with high-velocity gas, resulting in too high thermal and kinetic energy (see Walch & Naab, 2015). Only when a warm gas phase is present, generated mostly by radiation, the energy densities become comparable to observations. The CR energy densities in runs *SWC* and *SWRC* are within a factor of ~ 2 close to the canonical local ISM value of $e_{\mathrm{cr}} = 1.39\,\mathrm{erg\,cm^{-3}}$, supporting our model choices for the CR

Table 2.3: Time-averaged ($t = 25 - 100$ Myr) mid-plane ISM ($z = \pm 250$ pc) volume-filling factors and mass fractions of the cold: $T_{\rm cold} \leq 3 \times 10^2$ K, the warm: 3×10^2 K $< T_{\rm warm} \leq 3 \times 10^5$ K, and the hot: $T_{\rm hot} > 3 \times 10^5$ K phase. The warm phase is split into ionised and neutral gas. of. The given uncertainties include 1σ. Observational estimates for the local ISM are taken from Tielens (2005). The simulations are indicated in the first columns.

Run	$\overline{\rm VFF}_{\rm hot}$ [%]	$\overline{\rm VFF}^{\rm ionised}_{\rm warm}$ [%]	$\overline{\rm VFF}^{\rm neutral}_{\rm warm}$ [%]	$\overline{\rm VFF}_{\rm cold}$ [%]
S	89 ± 10	2 ± 2	7 ± 7	1 ± 1
SW	82 ± 7	4 ± 2	12 ± 6	2 ± 1
SWC	73 ± 6	6 ± 2	19 ± 5	2 ± 1
SR	56 ± 16	11 ± 7	30 ± 10	2 ± 1
SWR	53 ± 16	13 ± 9	32 ± 9	2 ± 1
SWRC	35 ± 26	14 ± 7	50 ± 21	2 ± 1
Tielens-05	∼ 50	25	30	1.05
Run	$\overline{\rm MF}_{\rm hot}$ [%]	$\overline{\rm MF}^{\rm ionised}_{\rm warm}$ [%]	$\overline{\rm MF}^{\rm neutral}_{\rm warm}$ [%]	$\overline{\rm MF}_{\rm cold}$
S	0.4 ± 0.3	2 ± 1	27 ± 7	71 ± 7
SW	0.2 ± 0.1	1.4 ± 0.4	28 ± 6	70 ± 6
SWC	0.2 ± 0.1	1.6 ± 0.5	34 ± 4	64 ± 4
SR	0.05 ± 0.02	8 ± 5	45 ± 12	47 ± 14
SWR	0.04 ± 0.01	8 ± 5	43 ± 8	50 ± 11
SWRC	0.03 ± 0.01	6 ± 3	48 ± 11	46 ± 13
Tielens-05	-	14	38	48

injection efficiency and the CR diffusion parameter.

2.6 Implications for galactic outflows

For investigating the outflow energetics, we define an energy loading γ (see e.g. Kim & Ostriker, 2017) as

$$\gamma = \frac{\dot{E}_{\rm out}}{\overline{\dot{E}}_{\rm inj}}, \tag{2.8}$$

where $\dot{E}_{\rm out}$ is the outflowing energy rate measured at $z = \pm 1$ kpc, consisting of thermal, kinetic, magnetic and CR energy, and $\overline{\dot{E}}_{\rm inj}$ is the average energy injection rate into the ISM, consisting of energy injection from SNe, stellar winds, ionising UV radiation and CRs.

Similarly, we define a mass loading η as the ratio of the mass outflow rate, $\dot{M}_{\rm out}$ measured at

Table 2.4: Average mid-plane ($z = \pm 250$ pc) kinetic, thermal, magnetic, and CR energy densities $\overline{e}$ with 1σ each for the six models for $t = 25 - 100$ Myr. To meaningful compare with observations, the magnetic energy densities are measured in cold ($T < 300$ K) neutral hydrogen gas (CNM), whereas the kinetic, thermal and CR energy densities are averaged over the entire mid-plane volume. Literature values - taken from Draine (2010) and references therein - are estimates for solar neighbourhood ISM conditions. Without radiative feedback, especially thermal and kinetic energies are higher than observed.

Run	$\overline{e}_{\rm kin}$ [erg cm^{-3}]	$\overline{e}_{\rm th}$ [erg cm^{-3}]	$\overline{e}_{\rm mag,CNM}$ [erg cm^{-3}]	$\overline{e}_{\rm cr}$ [erg cm^{-3}]
S	1.54 ± 1.31	3.36 ± 2.37	1.16 ± 0.97	-
SW	1.10 ± 0.72	1.50 ± 0.75	0.91 ± 0.55	-
SWC	0.91 ± 0.68	1.13 ± 0.75	0.80 ± 0.56	0.66 ± 0.37
SR	0.49 ± 0.24	0.71 ± 0.21	1.05 ± 0.35	-
SWR	0.42 ± 0.19	0.62 ± 0.23	1.06 ± 0.32	-
SWRC	0.34 ± 0.10	0.51 ± 0.28	0.86 ± 0.43	0.87 ± 0.63
Draine-10	0.22	0.49	0.89	1.39

$z = \pm 1$ kpc divided by the time-averaged instantaneous SFR $\overline{\dot{M}_\star}$,

$$\eta = \frac{\dot{M}_{\rm out}}{\overline{\dot{M}_\star}}. \tag{2.9}$$

Finding a useful working definition for the above loading factors is slightly complicated (see discussion in Kim & Ostriker, 2017). The energy injected into the mid-plane in one time-step does not instantaneously influence the energy outflow at a height of $z = \pm 1$ kpc, just as stars formed in the mid-plane do not correlate with the instantaneous mass outflow rate. One possibility is to introduce a time delay $\Delta t = \Delta z \times \tilde{v}^{-1}$, with a characteristic speed $\tilde{v}$ of the gas in the ISM. This would, however, assume that the gas flows funnel-like straight from the birth site of stars to the outflow region $z = \pm 1$ kpc. In reality, the gas is turbulent and the impact of local and temporal overlapping star formation events is non-linear. Another solution could be the use of moving averages but the choice of the window size is arbitrary and the resulting mean values can vary for more than 60 per cent compared to a global mean. We find that the most robust definition is to take the ratio of the respective outflow rates and the global averaged SFR and energy injection rates, $\overline{\dot{M}_\star}$ and $\overline{\dot{E}}_{\rm inj}$.

Quoted mean values for the energy loading and mass loading are then averaged over $t = 25 - 100$ Myr. To compare all models, we take the averages from the beginning of star formation (which is identical in all six runs), instead of the onset of an outflow. Therefore the averages are also taking into account episodes in which no or very weak outflows are present. This is the case for about ~ 10 per cent of the time in *S*, *SW*, *SWC*, ~ 65 per cent in *SR* and *SWR*, and ~ 40 per cent in *SWRC*. In Table 2.5, we give an overview of the mean SFR surface density $\overline{\Sigma}_{\dot{M}_\star}$, the mean energy loading factors, normalised to SN injection energy $\overline{\gamma}_{\rm sn}$, the mean mass loading factors η, and their fractional compositions from our simulations.

2.6.1 Energy loading

In Fig. 2.12, we present the energy rate budget of our simulations. In the top panel, we show the energy injected into the mid-plane ISM as a function of time. The solid lines show the energy injection rates of only SNe (not including the additional CR energy in the runs *SWC* and *SWRC*). The dashed lines indicate the total injected energy including winds, ionising UV radiation, and the CRs for the respective simulations. In the 2$^{\rm nd}$ panel, we show the same quantities but averaged over $t = 25 - 100\,\mathrm{Myr}$, $\overline{\dot{E}}_{\rm total}$ and $\overline{\dot{E}}_{\rm sn}$. These values are used to compute the energy loading factors. The integrated stellar wind and supernova energy injection rates are comparable, and the CR injection is 10 per cent of the SN rate by construction. The total energy injected in the radiation runs is higher by ~ 2 orders of magnitude. This is caused by the high UV photon luminosity, as expected from single stellar population models (see e.g. Agertz et al., 2013; Peters et al., 2017, for a discussion about wind and UV luminosities). However, in our simulations the injected radiation couples only weakly to the surrounding ISM and to the large-scale gas motions (Peters et al., 2017). For completeness, we present the energy injection by the different mechanisms in Appendix 2.9.2. In the 3$^{\rm rd}$ panel, we show the total energy outflow rates measured at $z = \pm 1$ kpc, and in the bottom panel we show the energy loading γ, measured at $z = \pm 1$ kpc, normalised to the total injected energy (dashed lines) and normalised only to the injected SN energy (solid lines). The models with the highest SN energy injection rate (*S, SW, SWC*) also have the highest energy outflow rate. Phases with SN energy loading values above unity result from the delayed impact of clustered SNe and the breakout of super-shells. Radiation couples inefficiently (runs *SR, SWR, SWRC*) and the total energy loading values are about a factor of 30 lower than the respective no-radiation simulations.

In the following we only refer to average SN energy loading values $\overline{\gamma}_{\rm sn}$ (see Table 2.5) as for the short time-scale simulations presented here SNe are the main driver for outflows. Also, these values can be better compared to the literature as most previous studies only include the SN feedback channel (see e.g. Fielding et al., 2017, 2018; Kim & Ostriker, 2018; Li et al., 2017; Schneider et al., 2020). In the SN-only run (*S*), 34 per cent on average of the injected energy leaves the mid-plane (see Table 2.5). This value decreases slightly to an average energy loading of $\gamma_{\rm sn} = 28 - 32$ per cent when accounting for stellar winds (*SW*, *SWC*). Model *SWC* has a ~ 5 percentage points higher energy loading than its counterpart without CRs (*SW*), because the CR diffuse independent of the bulk gas motion out of the mid-plane ISM and carry most of their energy with them without significant cooling losses. The inclusion of radiation lowers the energy loading significantly to about 1 per cent due to the inefficient conversion of radiation energy to the gas kinetic energy (Haid et al., 2018). Even if all radiation energy was converted into kinetic energy, it might not result in a significant outflow since no hot gas will be generated. Ionising UV radiation only heats the gas to $T \approx 10^4\,\mathrm{K}$ generating velocities of about $v \approx 10 - 20\,\mathrm{kms}^{-1}$. This is insufficient to overcome the external gravitational potential and lift the gas to heights of $z = 1\,\mathrm{kpc}$.

The out-flowing energy is initially dominated by thermal energy in run *S* and becomes comparable to the kinetic energy in the later phases of simulation. A similar behaviour is seen in model *SW*. The energy flux in all radiation runs is dominated by thermal energy. The situation qualitatively changes for runs with CRs. Here the energy flux is dominated by CR energy (see

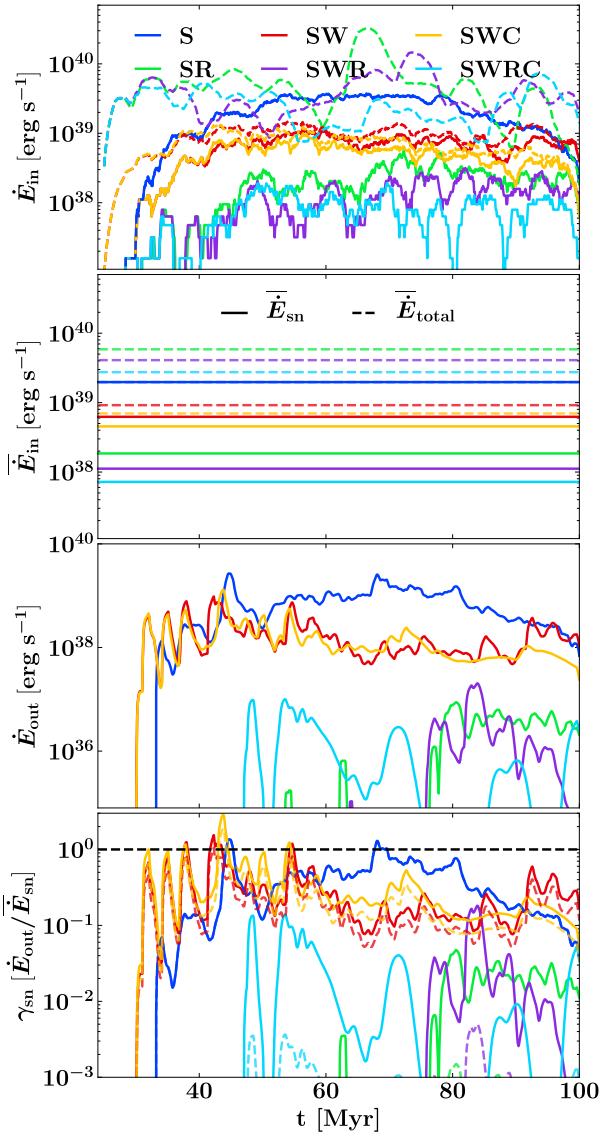

Figure 2.12: Top panel: SN energy injection rates (solid lines) and total energy injection rates (dashed lines) vs. time for the six models. The total energy injection rates include the wind luminosity (models *W*), the UV luminosity (models *R*), and the injected energy in CRs (models *C*). 2$^{\rm nd}$ panel: Mean SN energy injection rates $\overline{\dot{E}}_{\rm sn}$ (solid lines) and average total energy injection rates $\overline{\dot{E}}_{\rm total}$ (dashed lines) for all models, derived from data shown in the top panel averaged over the time interval from 25 Myr to 100 Myr. 3$^{\rm rd}$ panel: Total energy outflow rate measured at $z = \pm 1$ kpc vs. time. Bottom panel: Energy loading γ, measured at $z = \pm 1$ kpc vs. time. The solid lines show $\gamma_{\rm sn}$, which are normalised to the average SN energy injection rate. The dashed lines show $\gamma_{\rm total}$, normalised to the averaged total energy injection rate. The dashed black line indicates an energy loading of unity.

in particular simulation *SWC*). The time evolution of the kinetic, thermal and CR energy flux normalised to the injected SN energy is shown in Fig. 2.17 in Appendix 2.9.1 and the respective fractions of the average SN energy loadings are summarised in Table 2.5. If thermal phases are considered (see Fig. 2.18 in the Appendix and Table 2.5), the energy flux of most simulations is dominated by hot gas. At later times, the energy loading in hot and warm gas become comparable for simulations *S* and *SW*. Adding CRs (run *SWC*) shifts the budget towards warm gas in agreement with previous findings that CRs result in cooler and smoother outflows (Girichidis et al., 2018a).

In Fig. 2.13 we show the average SN energy loading factors $\overline{\gamma}_{\rm sn}$ as a function of the averaged SFR surface density $\overline{\Sigma}_{\dot{M}_\star}$ (top panel), of the average number of massive stars per cluster, the clustering, $\overline{N}_\star$, and of the averaged hot gas volume-filling factor $\overline{\rm VFF}_{\rm hot}$. Error-bars indicate a 1σ standard deviation. Simulations with the highest SFRs also have the highest energy loading factors (top panel of Fig. 2.13). The energy loading of *S*, *SW*, and *SWC* is very similar, reflecting their comparable ambient SN density distributions and high volume-filling factors of the hot phase (see Fig. 2.10 and Fig. 2.11).

In the middle panel of Fig. 2.13, we see that the SN energy loading also correlates with stellar clustering. The energy loading is highest for the SN only model *S*, which has the strongest clustering. Winds (*SW* and *SWC*) reduce the number of massive stars per cluster and $\overline{\gamma}_{\rm sn}$ is a factor of $\sim 1.5-3$ lower. Radiation (*SR*, *SWR* and *SWRC*) furthermore reduces the clustering of massive stars resulting in even lower energy loadings around ~ 1 per cent. This analysis indicates that the clustering of massive stars and therefore of the SNe is an important agent for driving efficient outflows (for similar conclusions see e.g. Smith et al., 2020).

We show the average energy loading $\overline{\gamma}_{\rm sn}$ as a function of the average hot gas volume-filling factor $\overline{\rm VFF}_{\rm hot}$ for the six models in the bottom panel of Fig. 2.13. As discussed above, ionising UV radiation decreases the SFR and the clustering of massive stars. Therefore, the SNR also decreases and fewer SN remnants overlap (see Sec. 2.4.3. This limits the creation of a volume-filling hot phase (see Sec. 2.5). Without additional driving mechanisms, the hot phase is the main agent for accelerating gas out of the mid-plane. On these short time-scales, the outflow driving by CRs has not yet set in.

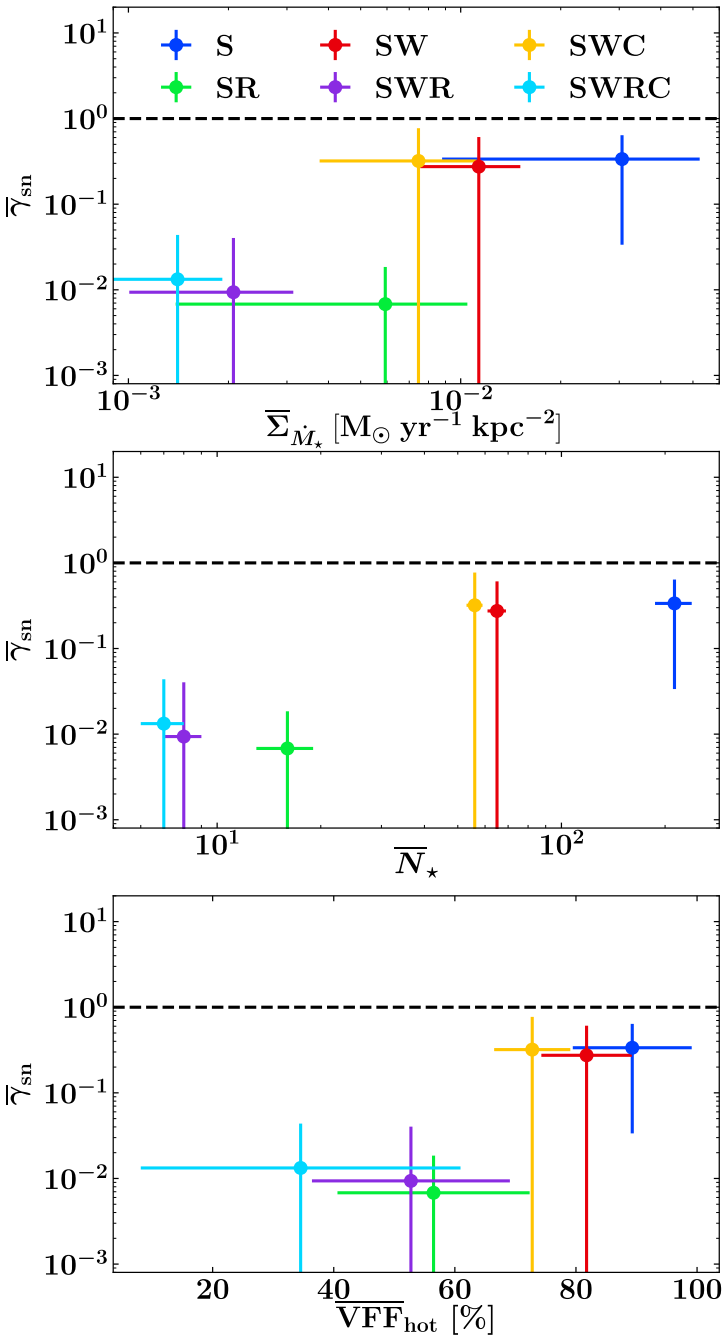

Figure 2.13: Average SN energy loading $\overline{\gamma}_{\rm sn}$ as a function of average SFR surface density (top panel), average number of massive stars per cluster (middle panel) and average hot gas VFF (bottom panel). Each value is given with 1σ scatter. The energy loading correlates with SFR, stellar clustering, and hot gas fraction. We therefore expect typically low energy loading values at disk surface densities $\sim 10 M_\odot\,{\rm pc}^{-2}$ for our simulation with the most complete set of physical models *SWRC*.

2.6.2 Mass loading

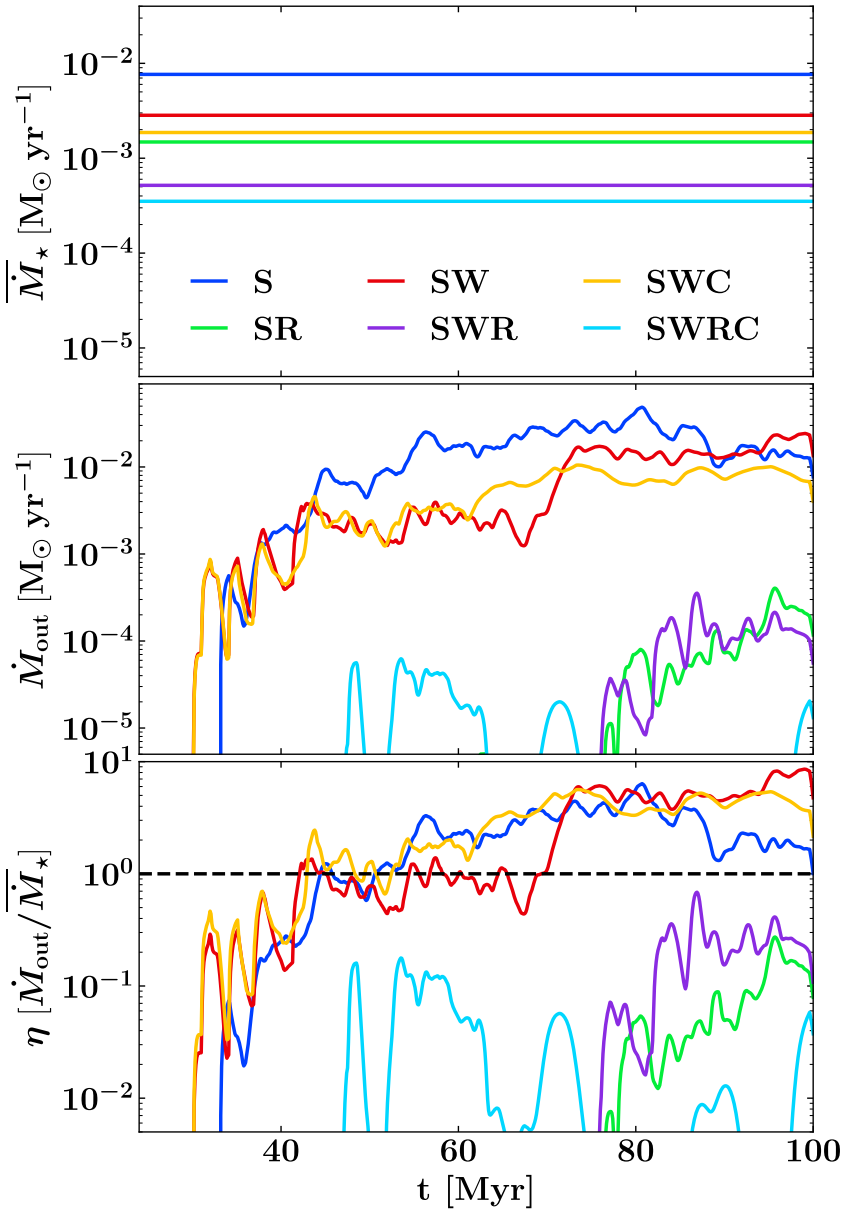

Figure 2.14: Average star formation rates $\overline{\Sigma}_{\rm M_\star}$ (top panel), instantaneous mass outflow rates $\dot{M}_{\rm out}$ through $z = \pm 1$ kpc (middle panel) and mass loading factors $\eta = \dot{M}_{\rm out}/\overline{\dot{M}}_\star$ at $z = \pm 1$ kpc (bottom panel) for the six simulations. Models with the highest SFRs also have the highest mass outflow rats and mass loading factors (*S*, *SW*, *SWC*). Simulations with radiation, including our most complete model (*SWRC*), do not drive strong outflows. CRs only become relevant for outflow driving on longer time-scales not presented in this study (see e.g. Girichidis et al., 2016b, 2018a).

In Fig. 2.14, we show the average star formation rates $\overline{\dot{M}_\star}$ (top panel), mass outflow rates through $z = \pm 1$ kpc (middle panel), and mass loading factors η (bottom panel) for the six models from $t = 25$ Myr to $t = 100$ Myr. Qualitatively, the behaviour of the mass loading is similar to the energy loading discussed above.

Strong outflows are constantly driven by the hot phase generated by clustered SNe (compare with the edge-on view of the gas surface density in Fig. 2.2 and also Fig. 2.11). For models with radiation (*SR*, *SWR*, *SWRC*), the outflow is delayed and the outflow rates are at least one order of magnitude lower due to the lower SFRs, weaker clustering, and correspondingly lower hot volume-filling factors. The trends of increasing average mass loading with increasing SFR, the increasing average number of massive stars in clusters and average hot gas volume-filling factors are summarised in Fig. 2.15. The interpretation of the trends is the same as for the energy loading discussed in the previous section. For the short time-scales after the onset of star formation presented in this study, SNe and their clustering are the main drivers for generating the hot phase which is powering the outflows (see e.g. Martin et al., 2012; Newman et al., 2012; Li & Bryan, 2020). For all simulations, the mass outflow is dominated by hot gas initially with the warm gas taking over soon after the onset of star formation in all simulations. This effect is strongest for *SWC* (see Fig. 2.19 in the Appendix and Table 2.5). This is also the only simulation with a measurable outflow in the cold phase at a very low fraction of 0.3 per cent (see Table 2.5).

The effects of CRs are intricate. They do not directly impact star formation but can have a long-term influence on the outflow. Between *SW* and *SWC* there is not much difference in η because their outflows are driven mostly by the hot phase generated in the mid-plane ISM, which has a comparable VFFs (see Sec. 2.5). The average hot gas VFF of *SWRC*, on the other hand, is a factor of ~ 2 lower which would result in a weaker outflow but the additional pressure gradient of the CRs helps to lift the gas away from the mid-plane, in alignment with observed mass loading factors η of unity and above. On a time-scale for up to 100 Myr CR do not increase the driving of an outflow. However, previous idealised studies without self-consistent star formation indicate that with a longer evolution the additional CR pressure gradient becomes the dominant mechanism of driving outflows (Simpson et al., 2016; Girichidis et al., 2016b, 2018a). We will investigate this further in Chapter 3 in which we focus on the long-term ($t = 250$ Myr) evolution of models *SWR* and *SWRC*, among others.

In Fig. 2.16 we show the average specific energy of the hot and cool gas outflow $\overline{e}_\mathrm{s} = \overline{\dot{E}}_\mathrm{out}/\overline{\dot{M}}_\mathrm{out}$ as a function of the average SFR surface density $\overline{\Sigma}_{\dot{M}_\star}$ for the six models. Here, we define the cool gas phase as the sum of the cold and warm gas as defined in Sec. 2.5 ($T_\mathrm{cool} \leq 3 \times 10^5$ K, $T_\mathrm{hot} > 3 \times 10^5$ K). Even though the total mass and energy outflow rates, as well as the composition of the outflows, vary strongly between the different models (Fig. 2.12, 3$^\mathrm{rd}$ panel and Fig. 2.14, 2$^\mathrm{nd}$ panel), the specific energy of the hot gas outflows only varies by a factor ~ 2. The specific energy of the cool outflow, however, varies by a factor ~ 20. Li & Bryan (2020) compiled a list of the outflow properties in recent small-box ISM simulations with only SN feedback (for a detailed list of considered simulations see their Table 1). Note that the definition of the thermal phases and the height in which the outflows are measured differ slightly in each work but are broadly comparable to ours. Li & Bryan (2020) find that the hot gas outflow specific energy $e_\mathrm{s,hot}$ only varies within a factor 30 ($e_\mathrm{s,hot} \approx 3.16 \times 10^{14} - 10^{16}$ erg g^{-1}), while the SFR surface densities in their examined

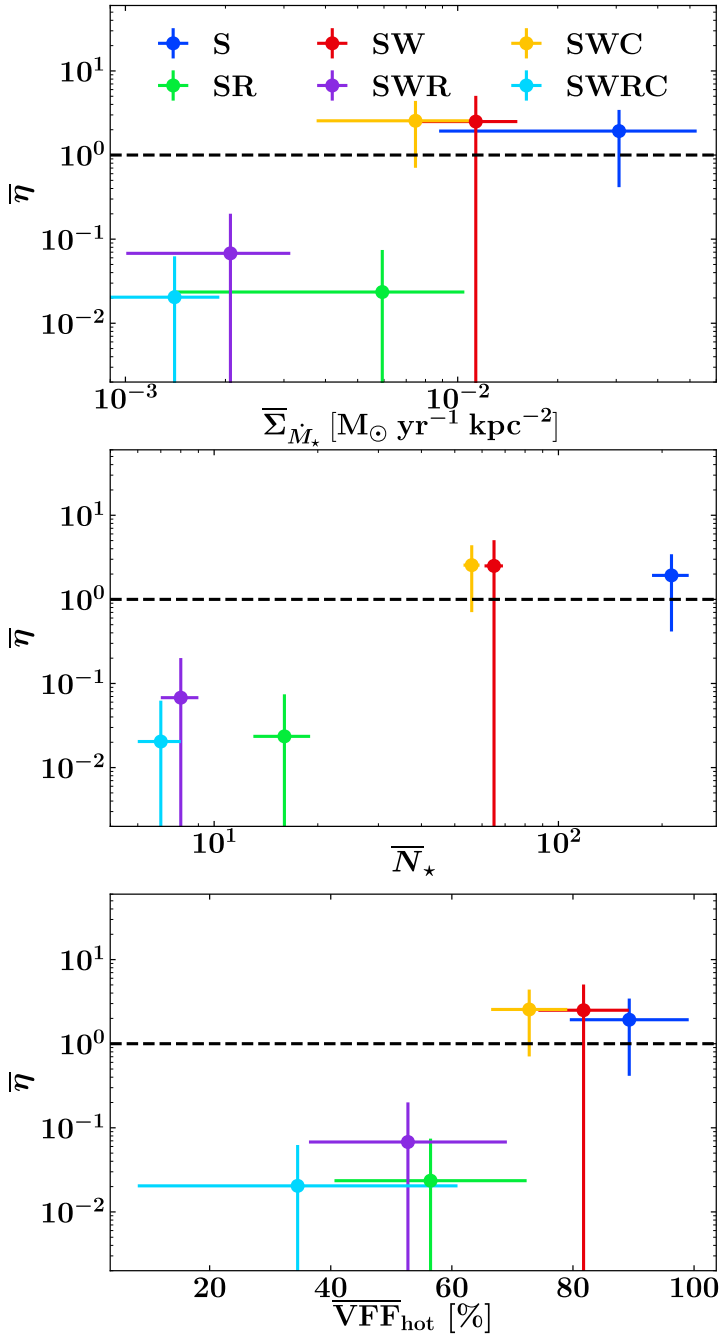

Figure 2.15: Average mass loading $\overline{\eta}$ as a function of SFR surface density (top panel), the average number of massive stars per cluster (middle panel) and averaged hot gas VFF (bottom panel). Each value is given with a 1σ scatter. Similar to the energy loading, the mass loading positively correlates with all three properties.

Table 2.5: Averaged SFR surface densities $\overline{\Sigma}_{\dot{M}_\star}$, averaged SN energy loading $\overline{\gamma}_{\rm sn}$ normalised to only SN injection, and averaged mass loading η with 1σ each for the six models, and the fractions of the energy- and mass loading factors divided into their compositions and thermal phases to the averaged total energy- and mass loading factors, $f_{\gamma_i} = \overline{\gamma_i}/\overline{\gamma_{\rm sn}}$ and $f_{\eta_i} = \overline{\eta_i}/\overline{\eta}$. The indices kin, th and cr denote the energy split into kinetic, thermal and CR energy, respectively, whereas hot, warm and cold divide the gas into thermal phases as described in Sec. 2.5. The time evolutions are presented in the Appendix, Fig. 2.17 to Fig. 2.19.

Run	$\overline{\Sigma}_{\dot{M}_\star}$ [$M_\odot$ yr^{-1} kpc^{-2}]	$\overline{\gamma}_{\rm sn}$ [%]	$\overline{\eta}$	$f_{\gamma_{\rm kin}}$ [%]	$f_{\gamma_{\rm th}}$ [%]	$f_{\gamma_{\rm cr}}$ [%]
S	$(3.1 \pm 2.2) \times 10^{-2}$	33.6 ± 30.3	1.93 ± 1.51	34.8	65.1	-
SW	$(1.1 \pm 0.4) \times 10^{-2}$	27.5 ± 33.4	2.51 ± 2.55	31.3	68.5	-
SWC	$(7.5 \pm 3.7) \times 10^{-3}$	32.0 ± 45.1	2.55 ± 1.85	16.0	47.5	36.4
SR	$(5.9 \pm 4.5) \times 10^{-3}$	0.7 ± 1.2	0.02 ± 0.05	6.6	93.2	-
SWR	$(2.1 \pm 1.1) \times 10^{-3}$	0.9 ± 3.1	0.07 ± 0.13	9.9	89.9	-
SWRC	$(1.4 \pm 0.5) \times 10^{-3}$	1.3 ± 3.0	0.02 ± 0.04	1.5	90.2	8.2
	$f_{\gamma_{\rm hot}}$ [%]	$f_{\gamma_{\rm warm}}$ [%]	$f_{\gamma_{\rm cold}}$ [%]	$f_{\eta_{\rm hot}}$ [%]	$f_{\eta_{\rm warm}}$ [%]	$f_{\eta_{\rm cold}}$ [%]
S	95.6	4.4	0.0	29.0	71.0	0.0
SW	96.1	3.9	0.0	18.2	81.8	0.0
SWC	82.6	17.3	0.2	14.5	85.2	0.3
SR	90.8	9.2	0.0	45.5	54.5	0.0
SWR	98.1	1.9	0.0	35.0	65.0	0.0
SWRC	99.9	0.1	0.0	93.7	6.3	0.0

simulations vary over 4 orders of magnitude between $\Sigma_{\rm M_\star} = 10^{-4} - 1\,{\rm M_\odot\,yr^{-1}\,kpc^{-2}}$, much in agreement with our results. However, they report a large spread for the ratio of the hot and cool outflow specific energy of $e_{\rm s,hot}/e_{\rm s,cool} \approx 10 - 1000$, whereas we find a lower ratio of $e_{\rm s,hot}/e_{\rm s,cool} \approx 50$ for the SN-only model *S*. In all our models the hot gas outflows have higher specific energy than the cool gas outflows and therefore can travel further away from the mid-plane ISM and have a possibly larger impact on the CGM.

2.7 This work in context

Although many recent works studied the solar neighbourhood ISM with its outflow properties, direct comparison is not always feasible, since most studies are omitting some major stellar feedback processes - most notably ionising UV radiation from massive stars and self-gravity - included in our framework. In the following, we will try to contextualise our results by comparing them to some of those recent studies. This comparison, however, is by no means exhaustive.

Butler et al. (2017) simulate a self-gravitating kilo-parsec region of a galactic disc with self-consistent star formation and feedback in form of SN and dissociating and ionising UV radiation,

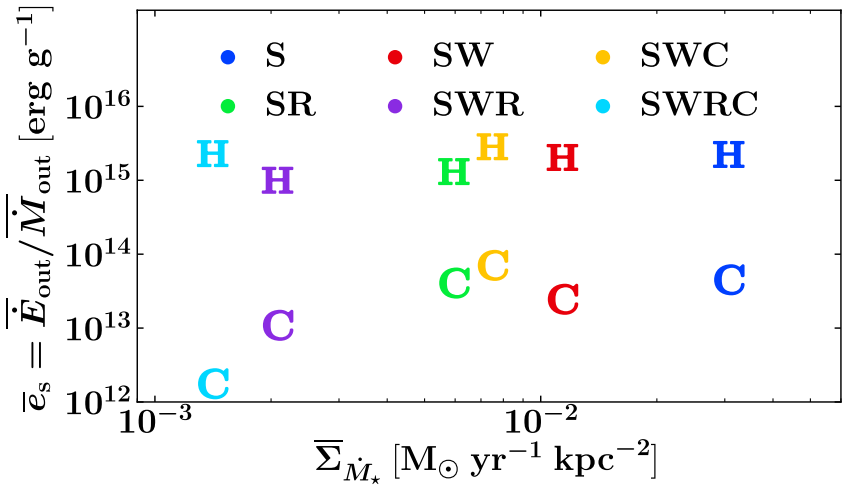

Figure 2.16: Averaged specific energy $\overline{e}_s$ of the hot and cool gas outflow as a function of $\overline{\Sigma}_{\dot{M}_\star}$. Here, we define the cool gas as the combination of our cold and warm phase defined in Sec. 2.5. The specific energy of the hot outflow in our six models is independent of the SFR and the stellar feedback processes.

down to a resolution of $\Delta x = 0.5$ pc. Their setup is inherited from a shearing, global disc simulation with a flat rotation curve. The kpc-sized patch sits at a galactocentric radius of 4.25 kpc with a $\Sigma_{gas} = 17 M_\odot\,pc^{-2}$. The boundary conditions, however, are not of a shearing box. Therefore, they only simulate for 20 Myr, i.e. the flow crossing time of the maximum shear velocity in their setup. They argue that those short time-scales are enough to reach quasi-statistical equilibrium conditions (for a similar conclusion see e.g. Pellegrini et al., 2020). SN feedback is realised by injecting 10^{51} erg of kinetic energy 3 Myr after the birth of an individual massive star. They model H_2 dissociation and photo-ionisation of hydrogen via radiative transfer with a reduced speed of light approximation. They achieve SFR surface densities in agreement with observational data from Bigiel et al. (2008, same data-set as we use for compression in Sec. 2.4.1) with a model including both radiation types and SN. In their analysis, they pick two regions (patches with $400 \times 400\,pc^2$ and $400 \times 600\,pc^2$), comparable in size to our mid-plane ISM definition. Only accounting for SN leads to very high SFR surface densities ($\sim 5 - 50\,M_\odot\,yr^{-1}\,kpc^{-2}$) in those regions, time-averaged from 5 to 10 Myr. However, spatially averaged on a kilo-parsec scale and time-averaged from 15 to 20 Myr, SN alone can already lead to reasonable SFRs in their models. They argue - similar to us - that the star-burst resulting from the lack of early feedback leads to a strong expulsion of gas out of the star-forming regions, which then leads to a regulation of star formation. Radiation is needed to properly model the chemical state and temperature structure of the ISM. Their reported mass fractions of ionised hydrogen is with $\sim 10-15$ per cent comparable to the warm ionised gas mass fraction in our *SR* model of $\overline{MF}^{ionised}_{warm} = (8 \pm 5)$ per cent (see Table 2.3).

Dobbs et al. (2011) simulate the star-forming ISM in disc galaxies including a galactic potential, heating from the ISRF, cooling, self-gravity, H_2 chemistry and SN feedback. They do

not explicitly include star formation via a sub-grid sink particle approach but instead track when a pocket of gas fulfils the criteria for star formation. When this is the case, they realise SNe by injecting thermal energy with 10^{51} erg per 160 $M_\odot$ of new stars that would have been formed multiplied by a star formation efficiency (SFE) ϵ into the medium. Those star formation criteria are very similar to ours (see Sec. 2.1): gas density has to be greater than 10^3 particles per cm^{-1}, the gas flow has to be converging, and it has to be gravitationally bound. With this prescription, they obtain reasonable ISM conditions and SFRs along the Kennicutt-Schmidt relation with only SN feedback but only for star formation efficiencies of $\epsilon \approx 0.05 - 0.2$.

Similarly, Tress et al. (2020) simulate an interacting M51-like galaxy with self-gravity, a non-equilibrium, time-dependent chemical network, self-consistent star formation with sink particles and stellar feedback only in the form of SNe. Also, their sink particle formation prescription and accretion parameters are nearly identical to ours with the criteria mentioned above, with the big difference that they, too, impose an artificial star formation efficiency of $\epsilon = 0.05$. SNe are then realised similarly as we do with thermal energy injection of 10^{51} erg and momentum injection, if the Sedov-Taylor phase is unresolved to prevent over-cooling. Again, this study can reproduce an ISM within observable scatter and a total SFR of 4 $M_\odot\,yr^{-1}$, which is very close to the observed value for M51 of 4.6 $M_\odot\,yr^{-1}$ (Pineda et al., 2018), with only SNe feedback. What Dobbs et al. (2011) and Tress et al. (2020) have in common is that they enforce an artificial SFE ϵ with observationally motivated values to achieve sensible SFRs. However, why this fairly low SFE exists in the first place is not explained. With our study, we provide physical explanations why the star formation is reduced, namely early feedback from massive stars in form of photo-ionisation and stellar winds.

Martizzi et al. (2016), Li et al. (2017), and Fielding et al. (2018) all study stratified disc models, only accounting for SN feedback and without self-gravity. In those simulations, the SNR scales with the SFR inferred from the Kenicutt-Schmidt relation, with one SN exploding per $100 - 150\,M_\odot$ of stars. For a gas surface density range comparable to our $\Sigma_{gas} = 10 M_\odot$ between $\Sigma_{gas} = 5 - 30 M_\odot$ they achieve energy loadings from around $\gamma_{sn} \approx 5$ per cent (Martizzi et al., 2016), $\gamma_{sn} \approx 15$ per cent (Li et al., 2017), up to $\gamma_{sn} \approx 40$ per cent (Fielding et al., 2018). In Li et al. (2017) SNe are distributed evenly in time but randomly in location parallel to the disc. Fielding et al. (2018) seed their SNe clustered in their stratified medium, leading to the creation of super-bubbles and breakouts from the mid-plane ISM. These emphasise the importance of clustered SNe to drive a galactic wind but lack the self-regulation of star formation and are therefore hard to compare with our models.

The galaxy formation simulations by Smith et al. (2020) model isolated galaxies with a virial mass of $M_{vir} = 10^{10}\,M_\odot$, accounting for SN feedback, photoelectric heating from a spatially varying FUV field and photo-ionisation in HII regions around massive stars with an overlapping Strömgren approximation scheme. They find - agreeing with our conclusions - that photo-ionisation has the strongest impact in regulating star formation, insensitive to variations in the star formation threshold density or small-scale efficiency parameters. Furthermore, reducing the clustering of SNe by pre-supernova feedback substantially reduces mass and energy outflow rates. This leads to energy and mass loading factors of $\gamma \sim 10^{-3} - 10^{-2}$ and $\eta \sim 1 - 10$, measured at $z = \pm 1$ kpc, for the simulations with SN, photoelectric heating and photo-ionisation. Compared to the runs with just SN feedback, the star formation as well as the outflow rates drop by ~ 2

orders of magnitude when photo-ionisation is added. Photoelectric heating only plays a minor role and does not influence the result to much extent when added to the models with SN-only feedback.

In the TIGRESS simulation suite (Kim & Ostriker, 2017, 2018) star formation is followed self-consistently via a sub-grid sink particle model comparable to our realisation. Their MHD simulations include self-gravity and stellar feedback in form of SNe and photoelectric heating on dust by temporally varying FUV radiation. They assume an optically thin medium with a uniform source distribution in the mid-plane ISM and vary the heating rate temporally, based on the mean radiation that the massive young stars would produce. However, they do not propagate hydrogen ionising UV radiation from massive stars via direct radiative transfer. The assumption of a optically thin medium does not generally hold and the local effects of shielding are not considered, which might result in an over-estimation of the FUV heating. In a setup with $\Sigma_{\rm gas} \approx 10\,{\rm M}_\odot$, they derive a SFR surface density of $\Sigma_{\dot{M}_\star} \approx 5.13\times10^{-3}\,{\rm M}_\odot\,{\rm yr}^{-1}\,{\rm kpc}^{-2}$, lying remarkably close to the observational motivated value of around $\overline{\Sigma}^{\rm obs}_{\dot{M}_\star} \approx 4.4\times10^{-3}\,{\rm M}_\odot\,{\rm yr}^{-1}\,{\rm kpc}^{-2}$. With this SFR, they achieve moderate mass and energy loading factors of $\eta \approx 1.5$ and $\gamma_{\rm sn} \approx 0.05$. Regarding the mass loading, their findings agree with our SN-only model *S*. The star formation properties and energy loading factor, however, are more similar to our *SR* model in star formation ($\Sigma_{\dot{M}_\star} \approx 5.9\times10^{-3}\,{\rm M}_\odot\,{\rm yr}^{-1}\,{\rm kpc}^{-2}$), and model *SWR* in energy loading ($\overline{\gamma}_{\rm sn} = 0.02$). The possibly boosted FUV heating due the lack of local attenuation might be the reason for the strongly regulated SFR with otherwise only SN feedback. In contrast, we might underestimate the impact of FUV heating by keeping the ISRF at a constant value of $G_0 = 1.7$, independent of the SFR. Another systematic difference compared to our models is the implementation of SNe. For resolved SNe, we inject thermal energy with a fixed radius of 3 grid cells (≈ 12 pc in the mid-plane ISM) around the sink particles while leaving the density structure as it is. On the other hand, Kim & Ostriker (2017) set the ambient density of the SN explosions to the mean value of the injection region, in order to prevent over-cooling. We do not find that this difference in the SN implementation explains the difference in the SFR of about one order of magnitude compared to their models to our model *S*. We refer the reader to Appendix 2.9.3 for a short discussion.

The strong effect of ionising UV radiation is also seen in higher resolution simulations on individual cloud scales (Haid et al., 2019) and is connected to the finding that, in dense media, ionising UV radiation from massive stars has a stronger impact on the environment than stellar winds (Haid et al., 2018). Stellar winds also reduce star formation by limiting star cluster growth (Gatto et al., 2017). However, they do not change the ambient SN densities as dramatically as ionising UV radiation (see Fig. 2.10). We have to note here, that even though we follow a momentum injection scheme for stellar winds the detailed wind bubble structures remain unresolved at the spatial resolution of our simulations. Our conclusions concerning the impact of stellar winds can therefore only be preliminary until higher resolution simulations become available.

Our finding that early feedback in the form of ionising UV radiation and, to a lesser extent, winds is required in order to recover an SFR consistent with the Kennicutt-Schmidt relation is in good agreement with recent observational results pointing towards the importance of early feedback for regulating star formation. In particular, the short feedback time-scales derived by

Chevance et al. (2020b) and Kim et al. (2021) for molecular clouds in nearby spiral galaxies are difficult to make consistent with models in which SN feedback dominates but agree well with the predictions of models in which UV radiation play a central role in cloud destruction (Chevance et al., 2020a).

2.7.1 Possible caveats

We fail to fully capture the cold, molecular phase in our simulations. One explanation is that the H_2 and CO abundances are likely under-resolved with a $\Delta x = 3.9\,\mathrm{pc}$ resolution (Seifried et al., 2017; Joshi et al., 2019) but also that the molecular gas most likely lives in regions which fulfil the accretion criteria of the sink particles with $n_{\mathrm{sink}} \approx 10^3\ \mathrm{cm}^{-3}$ and gets absorbed by them (compare with Tress et al., 2020). However, we need to include the chemical network and follow the evolution of the chemical species to properly model the re-processing of the ionising UV radiation.

Galactic shear is not accounted for in our study, as opposed to e.g. Kim & Ostriker (2017, 2018). There are observational studies of molecular clouds in the Milky Way (Dib et al., 2012) and of a spiral arm segment of M51 (Schinnerer et al., 2017) which do not find strong correlations between star formation activities and shear. On the other hand, theoretical works find a strong impact of differential galactic rotation on the ISM and SFRs (Colling et al., 2018), together with feedback from SNe and HII regions. It is not conclusive how important the inclusion of galactic shear for star formation is. Another effect of large-scale shearing motions is the enhancement the magnetic field strength via small-scale dynamo effects. Earlier studies (Walch & Naab, 2015; Girichidis et al., 2016b; Pardi et al., 2017; Girichidis et al., 2018b) show that the main effect of magnetic fields in our setup is the retardation of star formation by counteracting gravitational collapse with magnetic pressure, relatively independent of the magnetic field strength. Also, the anisotropic CR diffusion is insensitive to the strength of the magnetic field but rather its direction (Girichidis et al., 2018a). We, therefore, argue that the omission of magnetic field replenishment from a small-scale dynamo driven by large-scale shearing motions in our models does not crucially influence our results.

2.8 Summary

We present a suite of six stratified galactic disc simulations (Table 2.1), with initial gas surface densities of $\Sigma_{\mathrm{gas}} = 10\,\mathrm{M}_\odot\,\mathrm{pc}^{-2}$, successively accounting for the inclusion of the dominant energy and momentum injection mechanisms of massive stars and all major thermal and non-thermal components of the ISM. The simulations follow 100 Myr of evolution of a turbulently disturbed disk with time-dependent non-equilibrium chemistry, cooling and heating of the dusty, magnetised and self-gravitating ISM, star cluster formation, ionising UV radiation and stellar winds from massive stars, their SN explosions, as well as injection and propagation of CRs. Our study contains the first ISM simulations with self-consistent star (cluster) formation combined with the injection and transport of CRs together with SN feedback and stellar winds and additional ionising UV radiation. Radiative transfer is computed with the novel radiative transfer method

TreeRay (Wünsch et al., 2021) and the N-body dynamics of the sink particle are computed with a recent 4$^{\rm th}$-order Hermite integrator implementation (Dinnbier & Walch, 2020). We systematically investigate the impact of the aforementioned stellar feedback processes on star formation, the ISM conditions, and outflow properties.

The combination of various feedback mechanism from massive stars has non-linear effects on the ISM, star formation, and outflow properties. Only accounting for SN feedback (model *S*) results in an initial starburst $(3.1 \pm 2.2) \times 10^{-2}$ M$_\odot$ yr^{-1} kpc^{-2} exceeding observed values at similar total gas surface density (Fig. 2.6). The massive star clusters (cluster sink particles with a median mass of 1.6×10^4 M$_\odot$) form with a high number of massive stars, on average $\overline{N}_\star = 184$ (Table 2.2). The most massive clusters grow to 10^5 M$_\odot$, not compatible with estimates for open star cluster masses in the local neighbourhood (Fig. 2.9). This results in strongly clustered SNe with bi-modal ambient density distributions. Early SNe in new clusters explode at high densities ($n_{\rm ambient} \approx 30 - 300\,{\rm cm}^{-3}$). The majority of SNe, however, explode at very low ambient densities ($n^{80}_{\rm ambient} = 4.2 \times 10^{-3}\,{\rm cm}^{-3}$) and generate super-bubbles and a high hot gas volume-filling factor of $\overline{\rm VFF}_{\rm hot} \gtrsim 89$ per cent. As a result, the strong outflows deplete the mid-plane ISM rapidly (compare with Fig. 2.2, left panel) until star formation ceases towards the end of the simulation (Fig. 2.5, upper left panel). These outflows are characterised by an average mass loading factor η of order unity and an average energy loading factor of $\gamma \gtrsim 30$ per cent.

The inclusion of ionising UV radiation from massive stars has strong consequences for star formation as well as ISM phase structure and outflows even though it does not couple efficiently to the ISM (see Walch et al., 2013; Peters et al., 2017; Haid et al., 2018). Ionising UV radiation prevents gas accretion onto cluster sink particles by heating their surrounding ISM, therefore reducing the SFR by about one order of magnitude compared to non-radiation models (see also Peters et al., 2017; Butler et al., 2017). For our models, this effect is independent of the inclusion of stellar winds or cosmic rays. A qualitative comparison of the star cluster masses in our simulations to observational data from Kharchenko et al. (2005) suggests that the accretion limiting effect of ionising UV radiation is needed to achieve star cluster masses comparable to solar neighbourhood conditions (see Fig. 2.9). Additionally, the ambient SN density distribution becomes uni-modal with most SNe exploding at densities below $\lesssim 10^{-1}\,{\rm cm}^{-3}$. As a consequence, ionising UV radiation moves all models into the observed regimes for star formation (see Fig. 2.6) and ISM structure of the solar neighbourhood (see Fig. 2.11). The formation of HII regions right from the birth of the star clusters decreases the ambient ISM densities of the first SNe. The lower average mass of the cluster as well as the lower number of massive stars per cluster result in reduced mass and energy loading factors of $\overline{\eta} \approx 0.01 - 0.04$ and $\overline{\gamma}_{\rm sn} \approx 0.007 - 0.013$ (see Table 2.5). All runs including ionising UV radiation have solar neighbourhood like energy densities for the thermal ($\overline{e}_{\rm th} \sim 0.6\,{\rm erg\,cm}^{-3}$) and kinetic energy ($\overline{e}_{\rm kin} \sim 0.4\,{\rm erg\,cm}^{-3}$), with the most complete model *SWRC* being the closest to estimates for the local star-forming ISM from Draine (2010) (see Table 2.4).

In simulations with the strongest outflows like the SN and stellar wind models (*SW, SWC*) CRs have the same effect as reported in more idealised studies before. As soon as the energy outflow is dominated by CRs the outflow changes from being hot gas dominated to warm gas dominated. Simulations including ionising UV radiation have a much lower star formation rate

and an outflow driving CR pressure gradient cannot build up during our short simulation time of 100 Myr. However, this changes if the simulations are continued and will be discussed in the next chapter with simulated times up to 250 Myr. CRs have no immediate impact on star formation, stellar cluster properties, or the chemical composition. There is a trend for a $\sim$ 40 per cent increase in warm gas volume-filling factors, reflecting the trends seen in the outflow.

Our simulations indicate a qualitative change in the regulation of star formation and the evolution of the star-forming ISM if major stellar feedback processes - in particular the emission of ionising UV radiation - are neglected. If SNe are the only feedback process, star clusters can grow more efficiently leading to a rapid depletion of gas on $\sim$ 100 Myr time-scales. With mass loading factors of order unity, about the same mass is ejected by outflows and also becomes unavailable for star formation. Both, unhindered star cluster growth as well as galactic outflows regulate the ISM baryon budget and therefore star formation. While the picture of regulating star formation via outflows is generally favoured by cosmological galaxy evolution scenarios (see e.g. Somerville & Davé, 2015; Naab & Ostriker, 2017; Tumlinson et al., 2017, for reviews), it breaks down at the low gas surface densities investigated here when including all major feedback processes of massive stars.

The models including ionising UV radiation not only prevent the initial starburst but favour a different characteristic evolution behaviour in general. At such low surface densities, star formation is entirely controlled by pre-supernova feedback from massive stars on the small-scales of forming star clusters, instead of mid-plane out- and inflows. Mass loading and energy loading factors drop by about one order of magnitude (see Table 2.5). Our studies, therefore, support previous investigations showing similar trends. The realistic model, including stellar winds, ionising UV radiation and CR injection and transport results in the most typical gas phase structure, ISM energy densities, and star formation rates (see e.g. Table 2.3, 2.4, 2.5). Even though the results presented here show clear trends they merely present a status report. Future simulations on longer time-scales, higher resolution and even higher fidelity in physical modelling will have to confirm our conclusions.

2.9 Appendix A2

2.9.1 Phase structure of the outflow

We present the time evolutions of the energy-, and mass loading factors divided into the energy components kinetic-, thermal-, and CR energy for $\gamma_{\rm sn}$ (Fig. 2.17) and into the contributions of the hot-, warm-, and cold gas phases for $\gamma_{\rm sn}$ (Fig. 2.18) and η (Fig. 2.19). The averaged quantities are summarised in Table 2.5.

The outflows - if present - in the radiation runs (*SR, SWR, SWRC*) are dominated by by thermal energy ($f_{\gamma_{\rm th}} \gtrsim 89$ per cent. For the runs without radiation and higher SFR (*S, SW*) the ratio between thermal and kinetic energy in the outflow is $\sim 2:1$. The CR run without radiation (*SWC*) starts with a similar ratio but the outflow quickly becomes governed by the CR energy. Due to the lower SFR in *SWRC*, and hence lower CR injection rate, the raise in CR energy in the outflow is only seen at the very end of the simulation (Fig. 2.17).

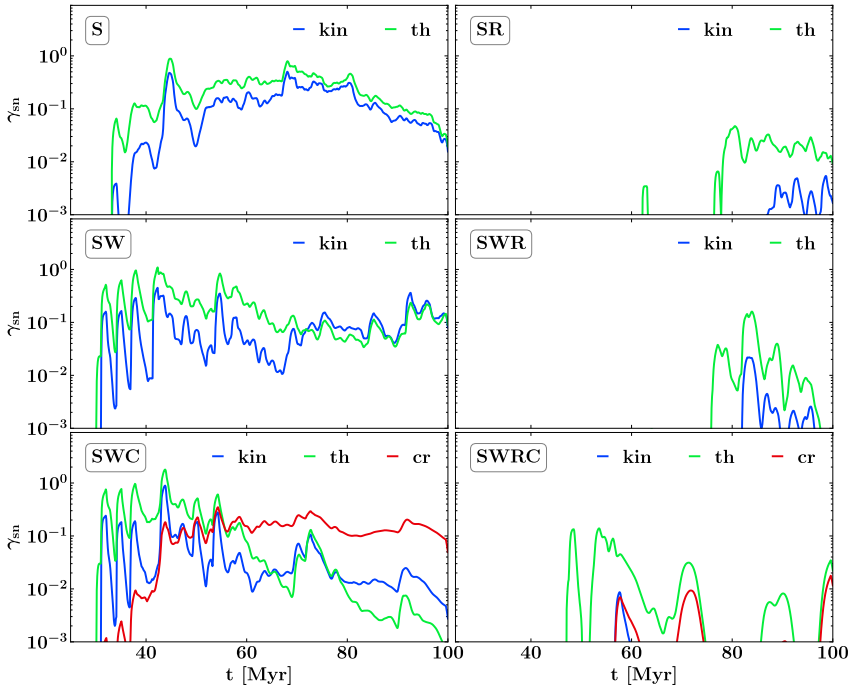

Figure 2.17: Energy loading factors divided into the energy components kinetic- (blue), thermal- (green), and CR (red) energy vs time for the six models.

The thermal composition of the energy outflow (Fig. 2.18) is initially dominated by the fast moving hot gas phase, with the slower moving warm phase gas catching up with some time delay. The same is also true for the mass outflows (Fig. 2.19). A cold gas outflow with a mass loading factor between $\eta \sim 1 - 10$ per cent is only present at later stages in *SWC*, supported by the additional CR pressure gradient. We expect - like it is demonstrated in idealised studies (Girichidis et al., 2016b, 2018a) - that a significant cold, and possibly even molecular, gas outflow will develop later in *SWRC*, when more star formation has happened. This will be studied in Chapter 3.

2.9.2 Energy injection

For completeness, we show the cumulative injected energy $\dot{E}_{\rm inj}$ in our six models as a function of time in Fig. 2.20. As discussed in Sec. 2.6.1, the injected energy by stellar winds and SNe are of the same order of magnitude. The wind injection is continuous throughout a massive star's lifetime, while SN injection is instantaneous at the end of a massive star's lifetime. The total injected CR energy is 10 per cent of the SN energy by construction. The total energy budget is dominated by the UV photons luminosity by up to 2 orders of magnitude in radiation runs *SR, SWR, SWRC*.

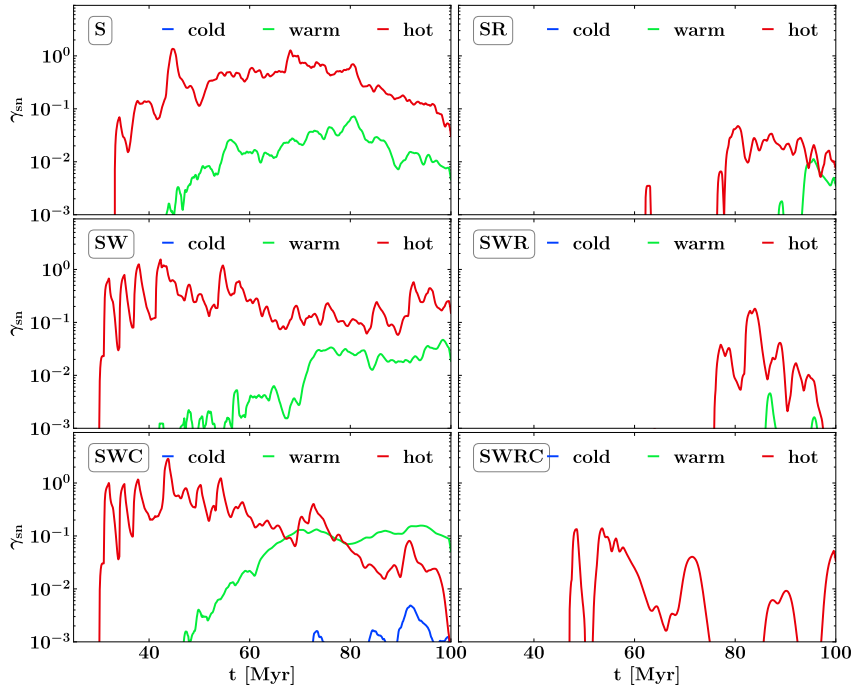

Figure 2.18: Energy loading factors split up into the contributions of hot- (red), warm- (green), and cold (blue) gas vs time for the six models.

2.9.3 Density flattening

We realise SNe with resolved Sedov-Taylor phase by injecting thermal energy (10^{51} erg) in a spherical region with radius of 3 grid cells around the sink particle in which a SN explodes, as described in Sec. 2.1. The density and temperature structure around the particle at the moment of injection is kept intact. However, another possibility is to *flatten* the injection region by setting the mass density, momentum density, and internal energy in that region to their mean values before assigning additional momentum and thermal energy like it is done in Kim & Ostriker (2017, 2018). They argue that this step is needed for self-regulation of the SFR and to prevent over-cooling. We test this with a model S^f, in which we only include SN feedback like in S but set the ambient gas density of the injection region around a SN to the mean value of this region. This results in a reduced SFR surface density by a factor of ~ 1.5, a reduced SN energy loading factor by a factor ~ 2 but nearly identical mass loading factors. The average number of massive stars per cluster is reduced by a factor of ~ 1.6 from 184 in S to 115 in S^f (see Table 2.6 and Fig. 2.21). Those results suggest that *density flattening* is not needed to prevent over-cooling when realising SNe with a fixed injection radius. With density flattening and no other feedback processes but SNe at play, we still achieve a fairly high SFR surface density of $\sim 2\times10^{-2}\,M_\odot\,yr^{-1}\,kpc^{-2}$, which lies in the upper limit regime of observed SFR surface densities for gas surface densities around $10\,M_\odot\,pc^{-2}$ (compare with Fig. 2.6).

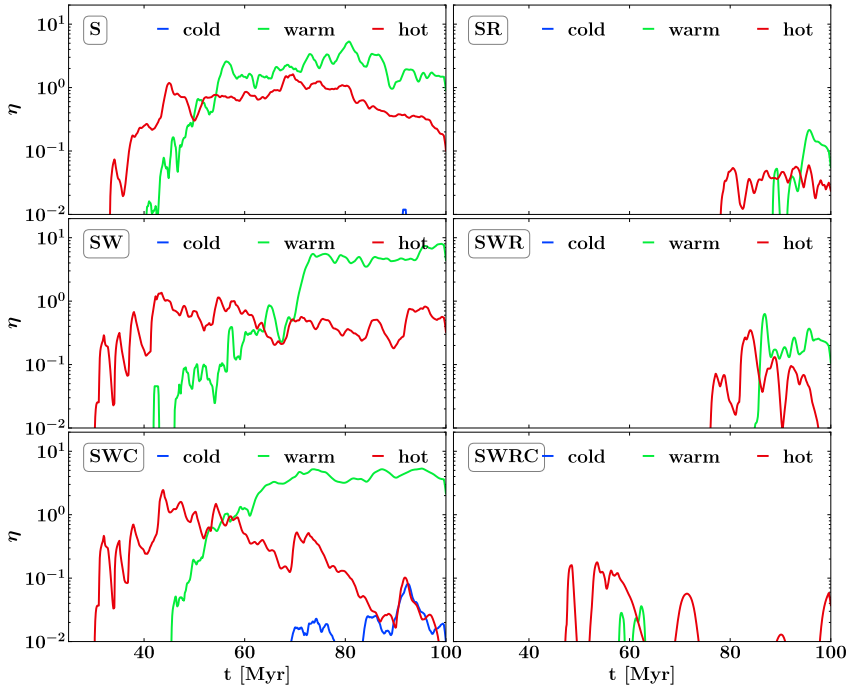

Figure 2.19: Mass loading factors split up into the contributions of hot- (red), warm- (green), and cold (blue) gas vs time for the six models.

Table 2.6: Average SFR surface density, SN energy loading factors, mass loading factor, number of massive stars per cluster for model *S* and a run with all the same parameters but the realisation of density flatting in the SN injection region S^f, each with 1σ.

Run	$\overline{\Sigma}_{\dot{M}_\star}$ [$M_\odot$ yr^{-1} kpc^{-2}]	$\overline{\gamma}_{\rm sn}$ [%]	$\overline{\eta}$	$\overline{N_\star}$
S	$(3.1 \pm 2.2) \times 10^{-2}$	33.6 ± 30.3	1.94 ± 1.51	184
S^f	$(2.0 \pm 1.1) \times 10^{-2}$	18.1 ± 12.2	1.65 ± 1.33	115

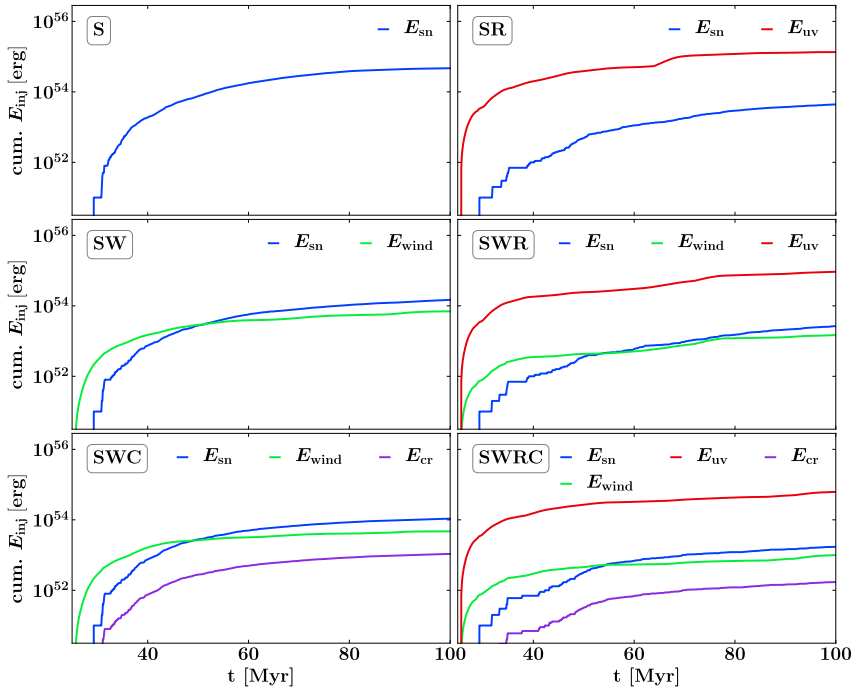

Figure 2.20: Cumulative energy injection over time of the different stellar feedback mechanisms - SNe, winds, UV radiation and CR - in our six models.

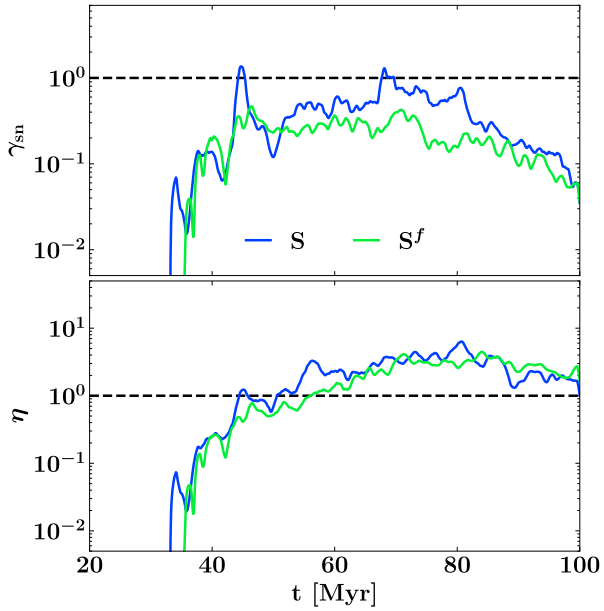

Figure 2.21: Energy- and mass loading factors over time for the two SN-only runs with different approaches of injecting the thermal SN energy into the surrounding medium - with (S^f) and without (S) density flattening of the injection region prior the injection.

Chapter 3

Galactic outflows driven by cosmic rays and runaway stars

In Chapter 3, we will further investigate the long-term impact of CR on the potential to drive and sustain galactic outflows. We also account for type Ia supernova background contribution. This, so far, neglected component might influence the structure and the strength of a galactic outflow since more CRs are getting injected into the domain via diffuse shock acceleration in the remnants of those type Ia SN. Additionally, we introduce a new physical process - runaway stars - and study to what extent do they change the formation of the hot gas phase and support outflows. This chapter will be submitted for publication in *Mon. Not. R. Astron. Soc.*

3.1 Numerical realisation of runaway stars and type Ia SN

In this chapter, we use the same simulation framework as we did in Chapter 2, with the addition of ejecting massive runaway stars out of the star clusters and a type Ia SN component.

The type Ia SN injection works exactly like the type II SN injection described in Sec. 2.1, with the only difference of the time and location of the injection. Type II SN are handled self-consistently by tracking the massive stars in the star cluster sink particle. At the end of the lifetime of a massive star, the thermal energy of 10^{51} erg gets injected around the sink particle with a fixed injection radius of $r_{\rm inj} = 4 \cdot dx \approx 12\,{\rm pc}$, if the Sedov-Taylor phase is resolved. Otherwise, we are using momentum injection. The type Ia SN explosion times and locations are not determined within the simulation, but are predefined. First, we define a fixed SN rate (SNR) equal to ${\rm SNR} = 3\,{\rm Myr}^{-1}$ for simulations with an initial gas surface density $\Sigma_{\rm gas} = 10\,{\rm M}_\odot\,{\rm pc}^{-2}$. This SNR is determined as follows: (*a*) we choose a SFR surface density $\Sigma_{\rm SFR} \approx 6 \times 10^{-3}\,{\rm M}_\odot\,{\rm yr}^{-1}\,{\rm kpc}^{-2}$, motivated by the Kennicutt-Schmidt relation $\Sigma_{\rm SFR} \propto \Sigma_{\rm gas}^{1.4}$ (Kennicutt, 1998; Kennicutt & Evans, 2012), (*b*) we translate $\Sigma_{\rm SFR}$ into a SNR surface density under the assumption of a standard Chabrier IMF, creating 1 SN every $100\,{\rm M}_\odot$ (Chabrier, 2003), (*c*) we scale the $\Sigma_{\rm SNR}$ into a total SNR for our computational domain of $500 \times 500\,{\rm pc}^2$, ${\rm SNR} = 15\,{\rm Myr}^{-1}$, (*d*) and finally arrive at ${\rm SNR}_{\rm Ia} = 3\,{\rm Myr}^{-1}$ with the assumption that 20 per cent of all SNe are type Ia SN (Joung & Mac Low, 2006). The location of the type Ia SN explosions is also predefined and independent of

what is happening in the simulation. We randomly place the SNe in the $x-y-$ plane and use a Gaussian distribution with a scale-height of 325 pc in z (Joung & Mac Low, 2006). CR are accelerated in the remnants of the type Ia SNe just as they are in the type II SNe with a 10 per cent efficency.

As described in the Introduction (Sec. 1.1), runaway stars are likely to be produced by two very different mechanisms, the dynamical ejection scenario (DES, Poveda et al., 1967) in which a massive star can get kicked out of a young star cluster via dynamical n-body encounters, and the binary supernova scenario (BSS, Blaauw, 1964), in which a SN explosion in a binary system kicks out the secondary star. We are considering both scenarios in our study. Observations suggest that $20-40$ per cent of all O stars, whereas less than 5 per cent of all B stars are runaways (Stone, 1991; Tetzlaff et al., 2011). We account for this by considering only O stars ($M > 15\,\mathrm{M}_\odot$) as possible runaway candidates and we choose a total runaway star fraction of 33 per cent of all O stars born in our simulations. Since the total runaway star fraction is not strongly constrained by observations the runaway star fraction implemented in our simulation is a free parameter. Furthermore, we choose $1/3$ of all runaway stars to be ejected by DES. The remaining $2/3$ are launched via BSS (Hoogerwerf et al., 2001).

DES We eject $\sim$ 11 per cent(= 33 per cent $\times\, 1/3$) of all O stars born within the first 3 Myr of a newly formed star cluster. After 3 Myr the runaway star production is halted because the runaway star production rate decreases drastically for more rarefied clusters (Oh et al., 2015), which happens due to cluster expansion by their dynamical evolution.

BSS We assume that all massive stars are part of a binary system and randomly pair every star created in the cluster with another one yet unpaired (Moe & Di Stefano, 2017). When the primary star (i.e. the more massive one) of a binary system explodes as a SN, we kick out the secondary with a certain probability, so that the overall runaway star fraction of O stars ejected via BSS ($\sim$ 22 per cent = 33 per cent $\times\, 2/3$) remains intact. When a star is chosen to become a runaway star we remove it from its parent cluster and spawn a new sink particle representing that runaway star with an isotropic velocity drawn from a Maxwellian distribution with $\sigma_{\mathrm{rnw}} = 30\,\mathrm{km\,s^{-1}}$ (Stone, 1991). We then correct the velocity of the runaway star with the escape velocity of the parent cluster so that the new sink particle attains velocity v_{rnw} at an infinite distance from the parent cluster. All ejected runaway stars interact with their environment via stellar winds and UV radiation and explode as SNe at the end of their lifetime, accelerating CR with 10 per cent efficiency.

3.2 Simulation overview

To study the impact of runaway stars and extended CR acceleration via type Ia SNe on the outflow properties of the galactic patch, we run another set of six simulations in total. Please note that the naming convention of the runs changes compared to the models in Chapter 2 to keep the simulation labels concise. We are considering three runs with CR and three runs without CR. In each group of three, one simulation will include type Ia SNe and one will include runaway stars. All models are simulated for $t = 250$ Myr, more than twice the duration as in the simulations in Chapter 2. The run named **X** is identical (except for the longer simulation time) to *SWR* from the

previous chapter (except for the longest simulation time; compare with Table 2.1). Adding a **C** to the name indicates the inclusion of CR (**XC** is therefore identical to *SWRC*). An additional **I** stands for the type Ia SNe background, whereas an additional **R** indicates the inclusion of runaway stars. All models include type II SNe feedback, stellar winds and ionising UV radiation. See Sec. 2.1 for a description of the feedback modules.

Table 3.1: List of simulations with the included stellar feedback and physical processes. *Type Ia*: Background Type Ia SNe contribution with fixed injection rate of $3\,\mathrm{Myr}^{-1}$, randomly placed in the $x-y-$ plane with Gaussian distribution in z. *Type II*: Type II SNe implemented as thermal energy input. *Winds*: Stellar winds implemented as radial momentum and mass injection. *UV*: Ionising UV radiation (HII regions). *CR*: Injection and transport of non-thermal CRs (10 per cent of the SN energy) at SN explosion sites. *Runaways*: Inclusion of runaway stars launched via the DES and BBS scenario. All runs include Type II SNe, stellar winds and ionising radiation as baseline feedback processes and are labelled with **X**. Runs including the Type Ia SNe background are additionally labelled with **I**. The same is true for CRs, **C**, and runaways stars, **R**.

Label	Type Ia	Type II	Winds	UV	CR	Runaways	t [Myr]
X	×	✓	✓	✓	×	×	250
XI	✓	✓	✓	✓	×	×	250
XR	×	✓	✓	✓	×	✓	250
XC	✓	✓	✓	✓	✓	×	250
XCI	×	✓	✓	✓	✓	×	250
XCR	×	✓	✓	✓	✓	✓	250

In Fig. 3.1, we show the gas column density for the six models of this chapter at a later stage of the simulation at $t = 220\,\mathrm{Myr}$. From left to right: **X** Feedback from type II SNe, stellar winds, and radiation, **XI** additional type Ia SN component with a SNR of $3\,\mathrm{Myr}^{-1}$, **XR** Type II SNe, stellar winds, UV radiation and runaway stars. The next three panels, **XC**, **XCI**, **XCR** are identical to the first three with the difference of added CR acceleration in SN remnants and anisotropic CR diffusion along the magnetic field lines. White circles indicate the position and the mass of star clusters. The blue coloured circles in panels **XR** and **XCR** are individual runaway stars. The strong influence of the CR in driving and sustaining an outflow is immediately evident when comparing the left three panels with the right three panels. Although, with a longer evolution time and more star formation events, the models without CR also manage to create structured outflow, but to a much lesser extent than the CR counterparts. Those trends have already been suggested in Chapter 2. See for example the gas column density for *SWR* in Fig. 2.3 (right panels), which is the identical simulation to **X**, but only up to $t = 100\,\mathrm{Myr}$, and the evolution of *SWRC* (right panels in Fig. 2.4), which is identical to **XC**. Since in Fig. 3.1 we show only one single snapshot out of the total evolution and the evolution of the ISM is very volatile as seen in Chapter 2, we cannot make a quantitative statement about the impact of runaway stars of additional type Ia SNe just by examining the column densities.

3.3 Star formation

In Fig. 3.2, we show the star formation history of the six models as histograms with bin width $\Delta t = 1\,\mathrm{Myr}$. The dashed black line in each panel indicates the mean SFR surface density, Σ_{SFR}, averaged from the onset of star formation at around $t = 20\,\mathrm{Myr}$ until the end of the simulation. Star formation begins $\sim 5\,\mathrm{Myr}$ earlier in simulations with the type Ia SN background since those additional SNe are exploding from the beginning of the simulation onwards, thus already shaping the ISM and triggering star formation. The main driving force for the initial star formation, however, is still gravitational collapse, which is counteracted by the initial turbulent driving (see Sec. 2.2 for details). The coloured shadings represent distinctive *periods* in which the simulation is in. Those periods are defined by the outflow behaviour of each simulation. Blue shading means that at those times the simulation is in an outflow-dominated state. Red shading means the exact opposite, i.e. the simulation is dominated by inflows. A green shading means that the simulation is in a transient state: neither dominated by outflows nor by inflows (for a definition of the periods consult Fig. 3.3).

We list the averaged Σ_{SFR} during those periods in Table 3.2. Except for in **X**, there is no significant difference between Σ_{SFR} during outflow periods and the globally averaged ($t =\sim 20 - 250\,\mathrm{Myr}$) Σ_{SFR}. For some simulations it is slightly higher (**XI**, **XC**) and for others slightly lower (**XR**, **XCI**, **XCR**). **X** has a ~ 2.5 Σ_{SFR} during outflow periods than the overall average. **X** does not include CR, nor an extended SN contribution with type Ia SNe, nor runaway stars. Those three components are all candidates of driving and sustaining prolonged outflows. Therefore, **X**, in which stellar feedback from type II SNe, stellar winds and ionising UV radiation are incorporated, can only influence the ISM and outflow structure directly with the massive stars, which are self-consistently formed with a sub-grid sink particle approach. To affect outflows, the Σ_{SFR} has to be higher than it is in transient periods. During inflow periods Σ_{SFR} is a factor ~ 2 smaller in all simulations, except again for in **X**, which lacks any inflow periods. This can be understood via the scarcity of gas available to form stars. After a prolonged outflow episode, the gas reservoir in the mid-plane ISM is depleted to some extent and a fountain flow has to replenish the gas reservoir first before new star formation can set in.

In Fig. 3.3, we show the net mass loading factor, η_{net}, at a height of $|z| = 1\,\mathrm{kpc}$. This factor is the ratio of the total mass flow through $|z| = 1\,\mathrm{kpc}$ divided by the total average SFR. An outflow period is defined by $\eta_{\mathrm{net}} > 1$. This means that more gas is leaving the mid-plane ISM through $|z| = 1\,\mathrm{kpc}$ than there is gas turned into new stars. On the opposite side, during episodes of $\eta_{\mathrm{net}} < -1$, more gas is falling onto the mid-plane again than new stars are formed. The available gas reservoir replenishes. We define periods with $-1 < \eta_{\mathrm{net}} < 1$ as *transient*. Outflow and inflow periods are following each other periodically, indicated an established fountain flow of gas.

3.4 Supernova properties

We show the ambient SN densities for our six models studied in this chapter in Fig. 3.4, similar to the analysis in Chapter 2 (see Fig. 2.10). The top panels include the runs with just type II SNe and no runaways, **X** left and **XC** with its additional CR on the right. In the middle panels, we

Table 3.2: Average SFR surface densities, $\Sigma_{\rm SFR}$, during the distinctive periods of each simulation (see Fig. 3.3 for definition). The overall averaged $\Sigma_{\rm SFR}$ ($t = \sim 20-250$ Myr) does not significantly differ from the $\Sigma_{\rm SFR}$ during outflow periods, except for the case in *X*, where $\Sigma_{\rm SFR}$ is ~ 2.5 times stronger during the outflow periods. The $\Sigma_{\rm SFR}$ decreases by a factor of ~ 2 in inflow periods for all simulations except for **X**. Due to the absence of an extended outflow period **X** does also lack any periods characterised by an inflow.

Label	global [$M_\odot\,yr^{-1}\,kpc^{-2}$]	outflow [$M_\odot\,yr^{-1}\,kpc^{-2}$]	transient [$M_\odot\,yr^{-1}\,kpc^{-2}$]	inflow [$M_\odot\,yr^{-1}\,kpc^{-2}$]
X	1.7×10^{-3}	4.3×10^{-3}	1.2×10^{-3}	-
XI	1.6×10^{-3}	1.8×10^{-3}	1.9×10^{-3}	5.1×10^{-4}
XR	2.4×10^{-3}	1.5×10^{-3}	3.7×10^{-3}	7.4×10^{-4}
XC	1.7×10^{-3}	2.1×10^{-3}	1.6×10^{-3}	8.8×10^{-4}
XCI	1.5×10^{-3}	1.3×10^{-3}	2.0×10^{-3}	4.5×10^{-4}
XCR	1.6×10^{-3}	1.3×10^{-3}	2.5×10^{-3}	5.9×10^{-4}

show the models with the type Ia SNe background component and the bottom panels include the runaway stars. The solid black histograms show the ambient density distribution of all SNe in each simulation. The grey shaded histograms show the ambient density distribution for 80 per cent of all SNe, ordered from the low-density to high-density. The upper limits of those histograms, n_{80}, give an intuition about the typical density in which a SN explodes and therefore its efficiency in coupling with the surrounding gas dynamics. The thermal energy injected by SNe exploding in a high-density environment gets quickly radiated away and does not contribute to heating the gas (see also the discussion in Chapter 2, Sec. 2.4.3). We are using blue histograms to indicate the contribution of type Ia SNe and green histograms for type II SNe with runaway stars as progenitors (bottom panels). We furthermore show the ambient density distribution for runaway star SNe from runaway stars ejected by BSS (red dashed histogram) and by DES (purple dashed histogram). The models with the type Ia SNe component produce about twice as many SNe as the models without it (see Table 3.3). Initially, we planned to realise 20 per cent of all SNe as type Ia SN (see Sec. 3.1). However, the type Ia SNe background component is independent of the actual dynamics in the simulation and we have to set a fixed SNR at the beginning. We choose this rate to be SNR = $3\,Myr^{-1}$, motivated by observations, (Kennicutt, 1998; Kennicutt & Evans, 2012). A type Ia SNR of SNR = $2\,Myr^{-1}$ would have obtained the aimed-at contribution of 20 per cent concerning to the type II SNR implemented in our simulations. However, this is not an error. The type Ia SNe originate from the old stellar population and it can very well be that the SNR of this component was higher or lower in the past. The ambient density distributions of the type Ia SNe follow the overall distribution. Nonetheless, the typical density of SN explosions decreases by a factor of $\sim 5-10$ from **X** to **XI**, and from **XC** to **XCI**. This is easily understood since the type Ia SNe also explode in the outflow region in a very low-density environment with a predefined Gaussian distribution in the z-direction with a scale-height of 325 pc. Around ~ 12 per cent of all SNe have a runaway star as a progenitor in runs **XR** and **XCR**. This fraction is in good agreement with observed runaway star fractions for massive O and B stars (see e.g. Maíz Apellániz et al.,

2018). An - at first - surprising result is that the runaway stars in our simulations end their lives in an environment which are significantly denser than the environments of their parental star clusters. A naive assumption would be that the runaway stars are born in the dense environments of star formation, then travel through the medium away from the mid-plane ISM, and finally explode in the sparse outflow region above and below the disk. This view, however, neglects two important points which we discussed in Chapter 2: (*a*) early stellar feedback impacts the surrounding of stars and star clusters and regulates star formation even before the first SN explodes, and (*b*) stellar clustering plays a crucial role. As soon as a sufficiently large star cluster starts undergoing its SN phase, overlapping SN remants efficiently evacuate their surroundings and drive the creation of a hot gas-phase. A single runaway star that gets ejected from a cluster travels into a medium outside of the influence of its parental cluster to a typical height of $z_{\rm sn} \approx 200\,{\rm pc}$ above/below the mid-plane (see 3.5). Individual stars ejected via DES - shortly after their formation - can travel up to $z_{\rm sn} \approx 800\,{\rm pc}$ above/below the mid-plane. During this travel time, the original cluster continues heating the surrounding gas via photo-ionisation and ultimately via a multitude of overlapping SN remnants. This leads to a drastic decrease in the ambient densities for the SNe exploding in the cluster. A single runaway star - albeit also ionising its surroundings - does not impact the ambient density around it to the extent a fully developed star cluster does and explodes in more pristine gas above/below the disk.

Table 3.3: Total number of SNe, N, and characteristic ambient density n_{80} for all SNe (subscript *all*), only the type Ia component (subscript *Ia*), and only the type II supernova with a runaway star progenitor (subscript *rnw*). Runaway stars explode in an environment which is denser, than the environment of the star cluster they originated from.

	X	**XI**	**XR**	**XC**	**XCI**	**XCR**
$N_{\rm all}$	716	1509	1097	710	1408	730
$N_{\rm Ia}$	-	692	-	-	695	-
$N_{\rm rnw}$	-	-	144	-	-	89
$n_{\rm all}\,[{\rm cm}^{-3}]$	5.7×10^{-2}	1.4×10^{-1}	3.5×10^{-2}	1.9×10^{-2}	2.2×10^{-1}	5.9×10^{-2}
$n_{\rm Ia}\,[{\rm cm}^{-3}]$	-	2.6×10^{-1}	-	-	3.1×10^{-1}	
$n_{\rm rnw}\,[{\rm cm}^{-3}]$	-	-	5.6×10^{-1}	-	-	1.8×10^{-1}

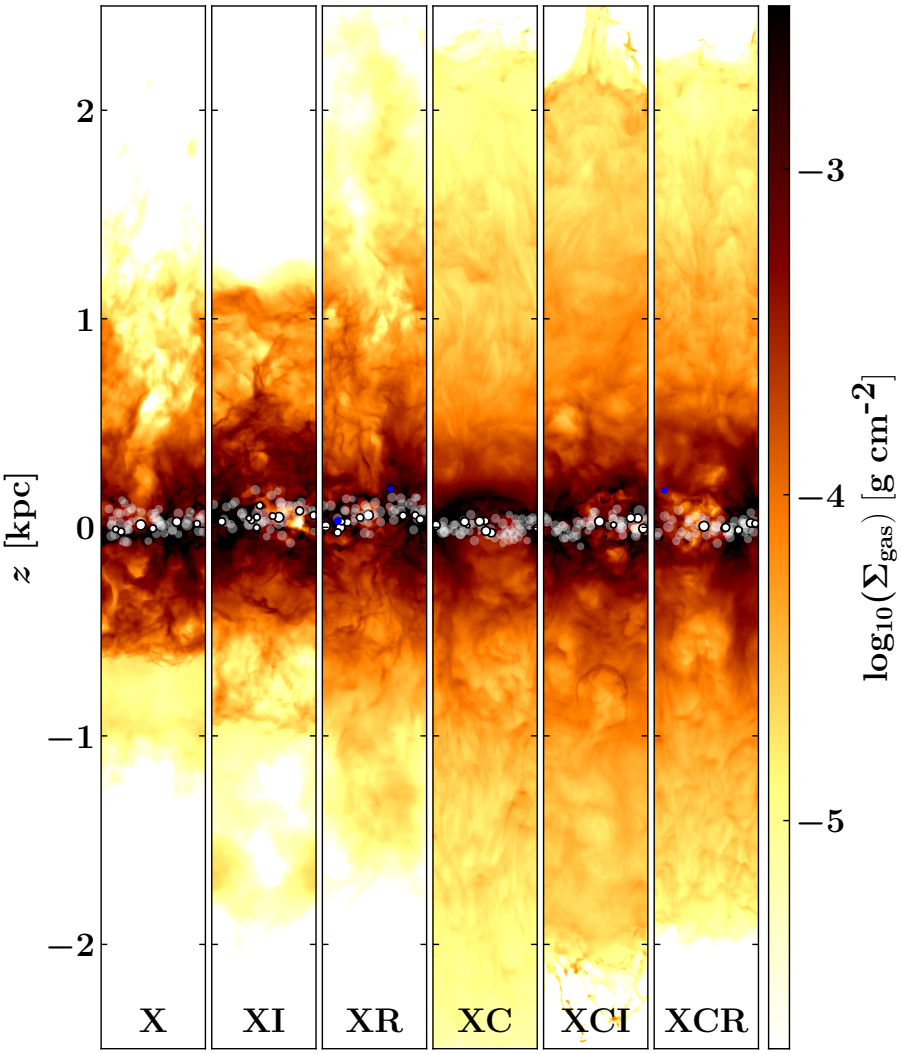

Figure 3.1: Edge-on view of the gas column density, $\Sigma_{\rm gas}$, for the six different models, all taken from a representative snapshot towards the end of the long-term evolution at $t = 220\,$Myr. From left to right: **X**, stellar feedback in the form of winds, ionising radiation and SNe, **XI**, added SNe Type Ia background, **XR**, like **X** but with the inclusion of runaway stars launched by dynamical ejection at the creation of a star cluster (DES) and by kicks from SN in a binary system (BSS). The next three panels, **XC**, **XCI**, **XCR** show simulations with the same configuration but with additional CR injection in SN remnants and anisotropic diffusion. White circles represent star clusters with the size of each circle scaling with the mass of the star cluster. Fully opaque white circles are active star cluster, transparent white circles are older star cluster, containing no active massive star anymore. Blue coloured circles in panel **XR** and **XCR** represent single runaway stars. CRs help driving a very smooth outflow to distances larger than 2 kpc away from the mid-plane. In the absence of CRs, the outflow is more structured and does not efficiently reach the same heights as a CR supported outflow.

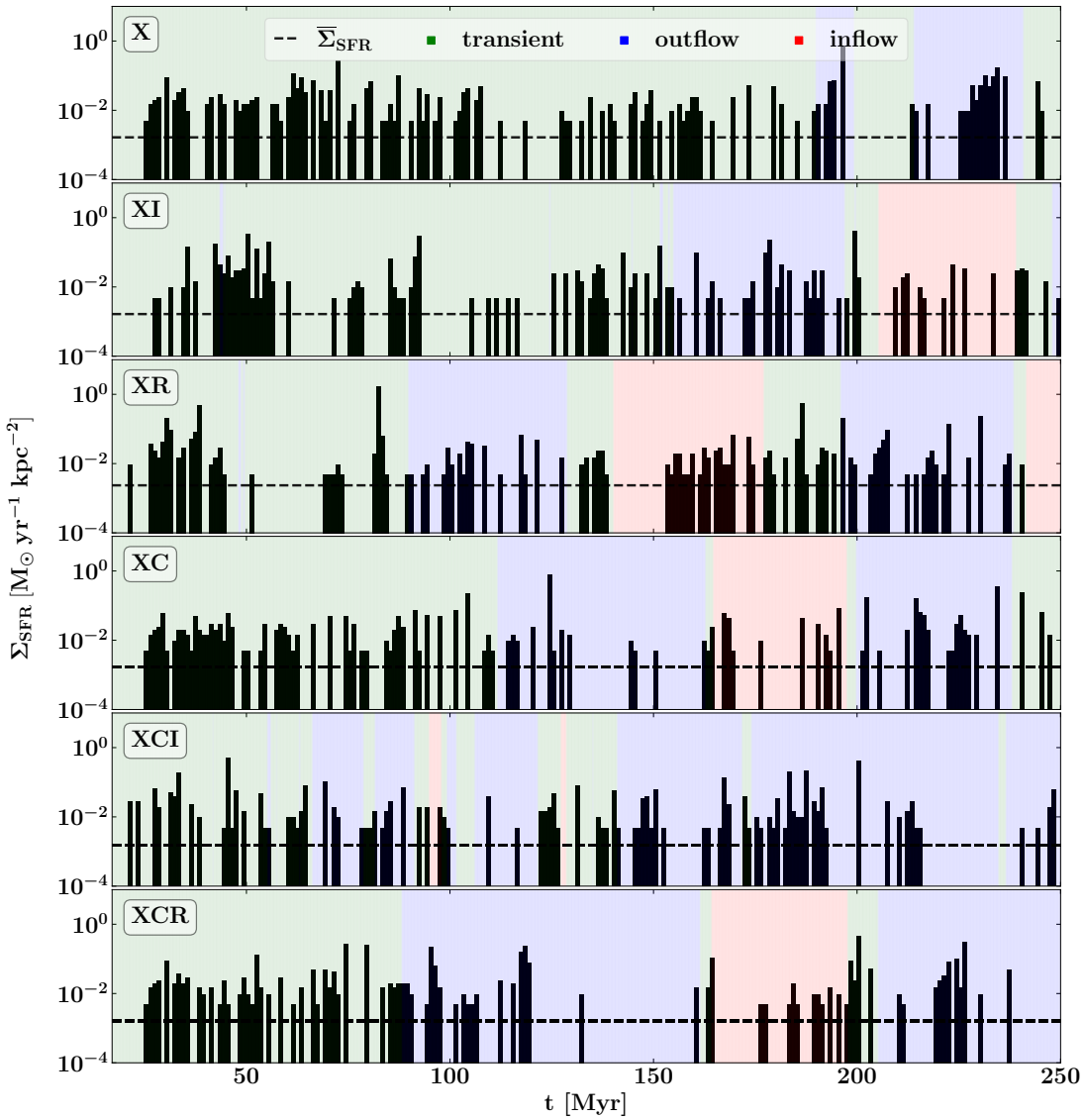

Figure 3.2: Histograms of the SFR surface density, $\Sigma_{\rm SFR}$, with a bin-width of $dt = 1$ Myr. The dashed black lines indicate a mean $\Sigma_{\rm SFR}$, averaged from the onset of star formation at $t \approx 20$ Myr to the end of the simulation at $t = 250$ Myr. The coloured shading indicates the distinctive phase in which the simulation is in - periods dominated by galactic outflow (blue), periods dominated by galactic inflow (red) and transient periods (green, see Fig. 3.3). The average $\Sigma_{\rm SFR}$ is comparable for all six models and the difference in the capabilities to drive outflows stems from the inclusion of CRs and runaway stars.

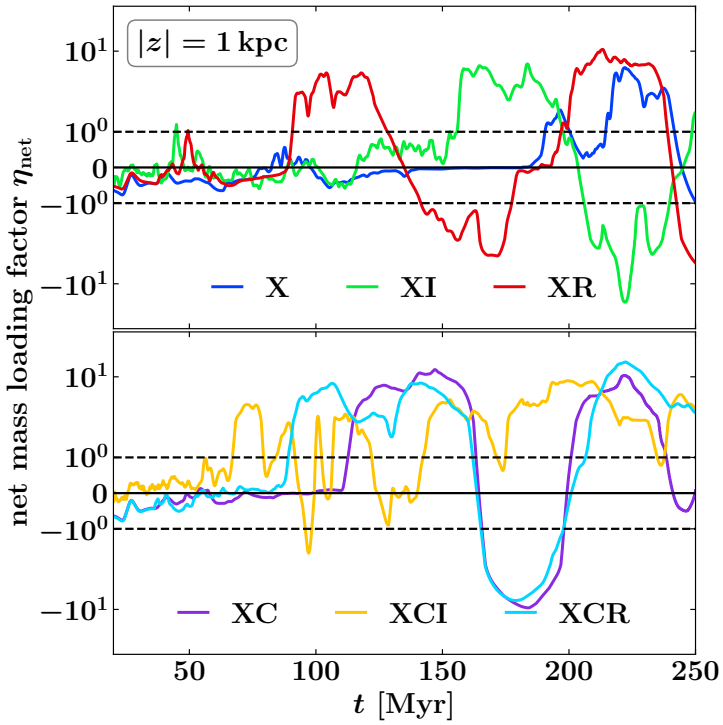

Figure 3.3: Net mass loading factor, $\eta_{\rm net}$, defined as the ratio of the total gas mass flow (inflow and outflow) through $|z| = 1$ kpc and the average SFR. Periods in which $\eta_{\rm net}$ exceeds 1 are considered to be outflow dominated (blue shaded in Fig. 3.2) and periods in which $\eta_{\rm net}$ drops below -1, i.e. more gas enters the system through $|z| = 1$ kpc than gas is transformed into new stars, are considered to be inflow dominated (red shaded in Fig. 3.2). Periods in which $\eta_{\rm net}$ lies between -1 and 1 are labelled *transient* (green shaded in Fig. 3.2).

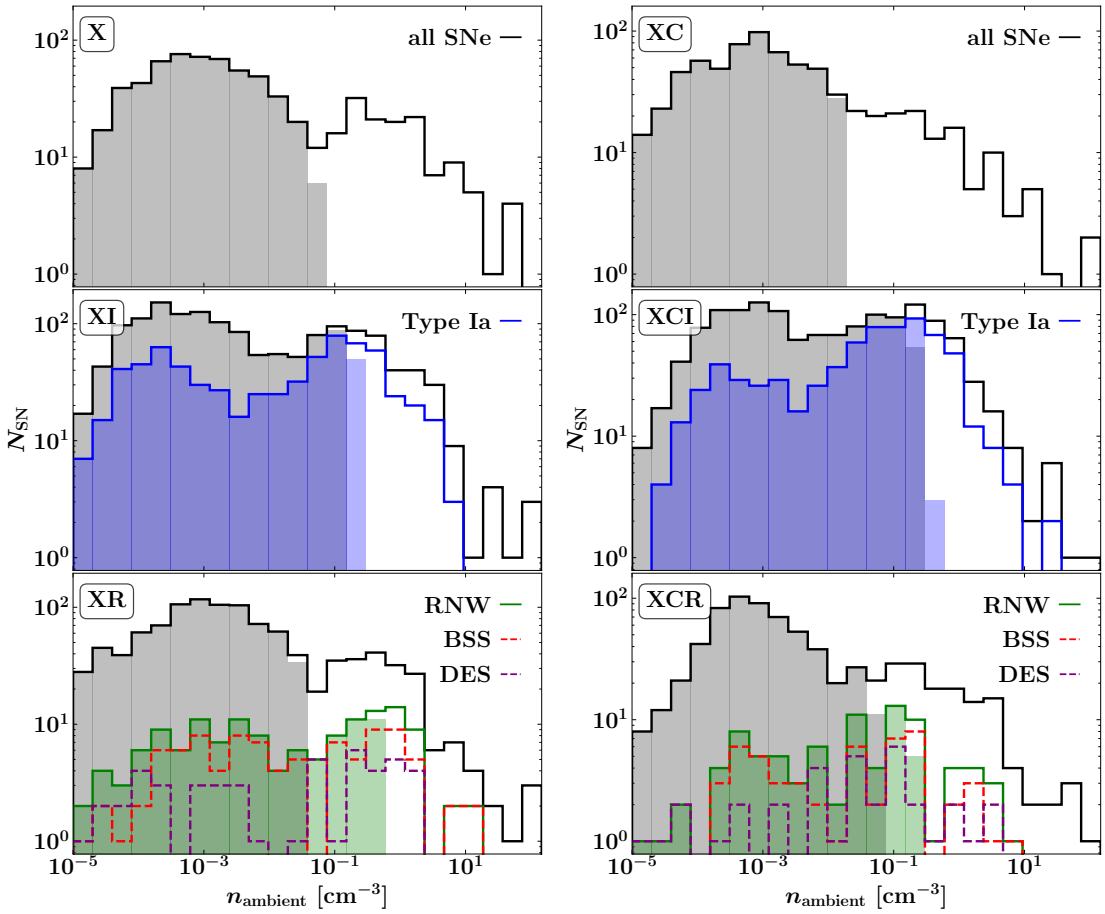

Figure 3.4: Ambient gas densities, $n_{ambient}$, at the explosion sites of SNe. The black histograms compose of all SNe exploded in the simulation. The grey shaded histograms include 80 per cent of all SNe with ascending $n_{ambient}$. This measure gives a typical density, n_{80}, for the SNe and is an estimate of the overall effectiveness of the SNe. The coupling of the SNe energy to the gas dynamics greatly reduces with the increasing density of the environment due to radiative losses. The blue histograms (middle panel) show the distribution of the subset of Type Ia SNe. The shape of their distribution and n_{80} are similar to the SN Type II component, although the total number of SN explosions, N_{SN}, strongly increases. The bottom panel shows $n_{ambient}$ for the models **XR** and **XCR** including runaway stars (green histogram). The overall number of runaway stars created by our model is small. The different ejection mechanisms BSS (red dashed histogram) and DES (purple dashed histogram) do not substantially differ. However, the typical density, n_{80}, for the SNe coming from runaway stars is significantly larger than for the Type II SNe exploding in star clusters. The inclusion of CR does not affect the ambient density distribution of the SNe to much extend and the trends are similar to the case without CRs.

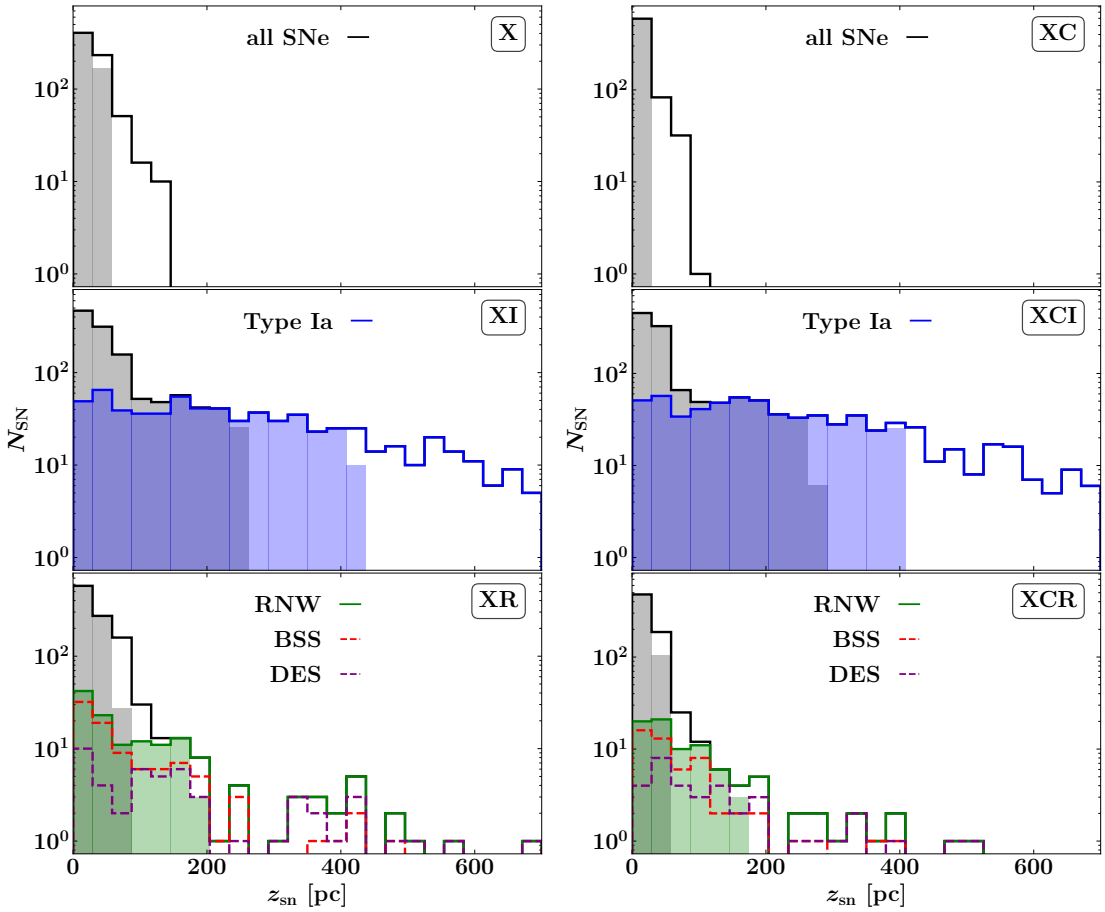

Figure 3.5: Height above/below the mid-plane of the SN explosion sites, z_{sn}. The grey shaded histogram indicates the maximum height in which 80 per cent of all SNe explode. Excluding SNe from runaway stars, all Type II SNe explode within $z_{sn} \approx 100$ pc away from the mid-plane. The star-formation independent contribution of Type Ia SNe greatly extends the scale-height of the SNe up to $z_{sn} \approx 800$ pc. 80 per cent of all runaway stars explode at a height of $z_{sn} \approx 200$ pc, double the value of their Type II counterparts exploding in star clusters. Overall, there is no big difference in the height runaway stars ejected by the two different mechanisms can reach, although there are occurrences of individual runaway stars launched shortly after their birth via DES reaching up to $z_{sn} \approx 800$ pc and depositing their SN energy far into the outflow region.

3.5 Galactic outflows

3.5.1 Mass outflow

We analyse the gas outflow in Fig. 3.6, where we show the mass outflow rates, $\dot{M}_{\rm out}$, measured at $|z| = 1$ kpc (solid lines) and $|z| = 2$ kpc (dashed lines), divided into the three thermal gas-phases, hot ($T > 3 \times 10^5$ K, red lines), warm (300 K $\leq T \leq 3 \times 10^5$ K, green lines), and cold ($T < 300$ K, blue lines). Simulations including CR are shown in the right panels, and without CR are shown on the left. First, we focus on the models without CR. The run without additional type 1a SNe or the inclusion of runaway stars (**x**) drives only a small outflow. It has a weak outflow episode after $\sim$ 80 Myr of star formation (which starts at $\sim$ 20 Myr) and another somewhat stronger outflow episode towards the end of the simulation. Adding the type Ia SNe background (**XI**) does not increase the amplitude of the outflow, but makes the outflow more constant. The outflow sets in earlier due to the energy injection from the type Ia SNe, even before star formation begins. The strongest outflow is driven when accounting for runaway stars (**XR**). Similar to **X**, the outflow is periodic, but with a higher frequency. The total mass transported out of the mid-plane ISM is $\sim$ 5 times higher as in the case without runaway stars. At the height of $|z| = 1$ kpc the ratio of hot to warm gas by mass in the outflow is 2:1. Going further away from the mid-plane, the hot gas-phase has nearly no losses and flows with the same magnitude and only very short delay time through $|z| = 2$ kpc (dashed lines). By contrast, only $\sim$ 10 per cent of the warm gas outflow at $z_{1\rm kpc}$ reaches $z_{2\rm kpc}$. The picture drastically changes when CRs are introduced in the simulations (right panels). The outflow is overall more constant and from a much higher magnitude. Two features are especially different to a non-CR-driven outflow. The gas-phase structure is completely dominated by the warm gas-phase. The outflow is cooler and slower. There is an extended delay between $\sim$ 30 Myr (**XC**) and up to $\sim$ 100 Myr (**XCI**) in the arrival time of the warm gas-phase at $z_{1\rm kpc}$ and $z_{2\rm kpc}$. The second remarkable feature is that even cold gas ($T < 300$ K) is streaming through $z_{2\rm kpc}$ - albeit to a much lesser extent than the warm and hot gas. As discussed in Chapter 2, Sec. 2.4.1, the cold gas-phase can be taken as a proxy for molecular gas. CR can drive and sustain a molecular outflow.

3.5.2 Energy outflow

We repeat the analysis for the mass outflow (Sec. 3.5.1), but this time for the energy outflow, in Fig. 3.7. Overall, the picture is similar to the mass outflow and the conclusions are by large similar. However, we get a new insight by splitting the energy of the outflow not into its thermal phases, but into its components: thermal energy, $E_{\rm th}$, kinetic energy $E_{\rm kin}$ and CR energy, $E_{\rm CR}$. In Fig. 3.8, we show the outflowing energy split into its component. For simulations without CR, the kinetic and thermal energy are in equipartition, a characteristic of a turbulent flow. Most of the energy, however, gets carried out of the ISM via CR (right panel, purple lines). The CR pressure gradient needs to build up over a long time and the CR-driven outflow through $z_{1\rm kpc}$ becomes efficient after $t \approx 100$ Myr. It then takes another $\sim$ 50 Myr for the CR pressure gradient to set in up to a height of $|z| = 2$ kpc but as soon as it is established, the CR diffuse through the medium up to $z_{2\rm kpc}$ with virtually no losses.

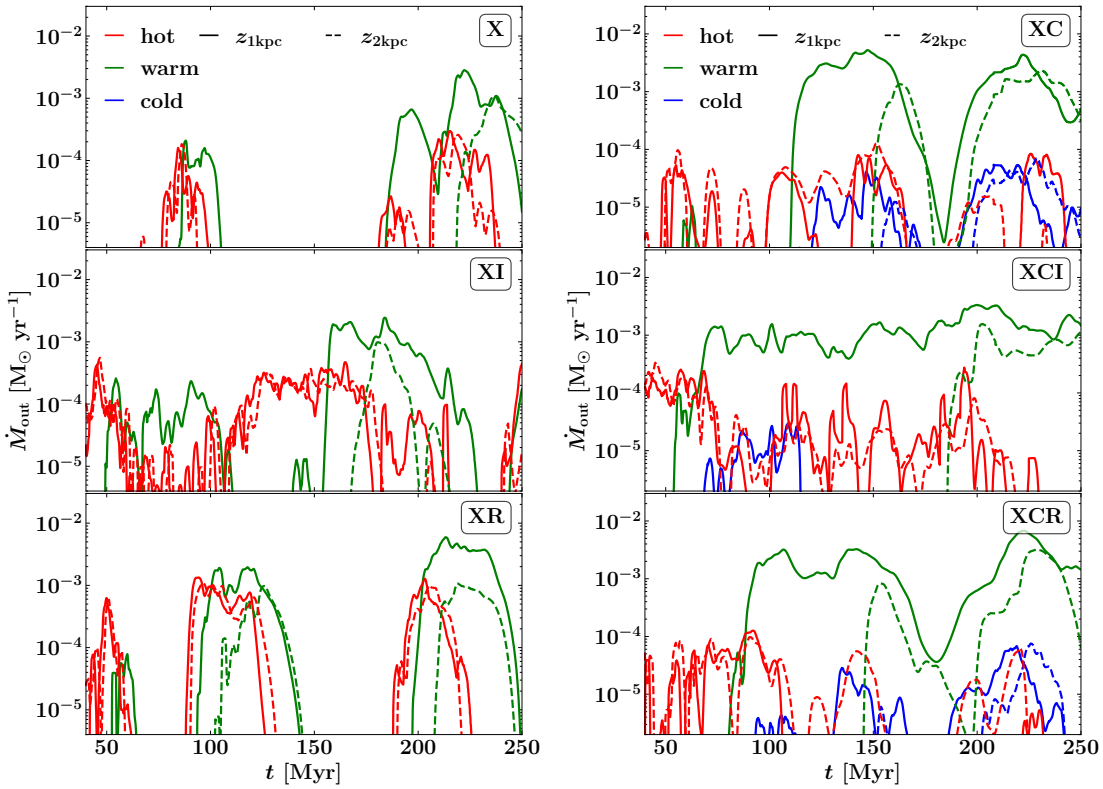

Figure 3.6: *Left* Mass outflow rates, $\dot{M}_{\mathrm{out}}$, through $|z| = 1$ kpc (solid lines) and $|z| = 2$ kpc (dashed lines), split up into the thermal gas components $T > 3 \times 10^5$ K (red), 3×10^3 K $\leq T \leq 3 \times 10^5$ K (green), $T < 300$ K (blue). In the absence of CRs, the outflow is dominated by the hot gas-phase at a height of $|z| = 1$ kpc. Towards a height of $|z| = 2$ kpc, the amount of warm gas decreases while the levels of the hot gas outflow are nearly the same. The overall strongest, albeit episodic, outflow in the models without CR is driven in the model with runaway stars, **XR** (bottom panel). In **XI**, a continuous outflow of hot gas is driven by the additional energy input from the type Ia SNe background. A slower propagating warm gas component is only present episodically and is not sufficiently lifted to heights up to $|z| = 2$ kpc. *Right* The characteristics of the outflow change drastically with the inclusion of CR. At first, the outflow is dominated by the hot gas-phase, similar to the models **X**, **XI**, and **XR**. However, in more developed stages of the simulation, the mass outflow is governed by the warm gas-phase (green lines), supported by the additional CR pressure gradient. This non-thermal energy reservoir does not cool efficiently and can lift the warm gas component even to heights of $|z| = 2$ kpc and above over longer time-scales. Remarkably, even cold gas outflows can be sustained, which are missing entirely in the models without CRs. The total mass outflow rate is for all three models comparable. This indicates that the dominant process to drive outflows is the build-up of the additional CR pressure gradient. However, the CR energy density saturates towards later stages of the simulation and the higher CR injection rate in the models with type Ia SN background (**XCI**) does not affect the amount of outflow compared to the other CR models (**XC**, and **XCR**).

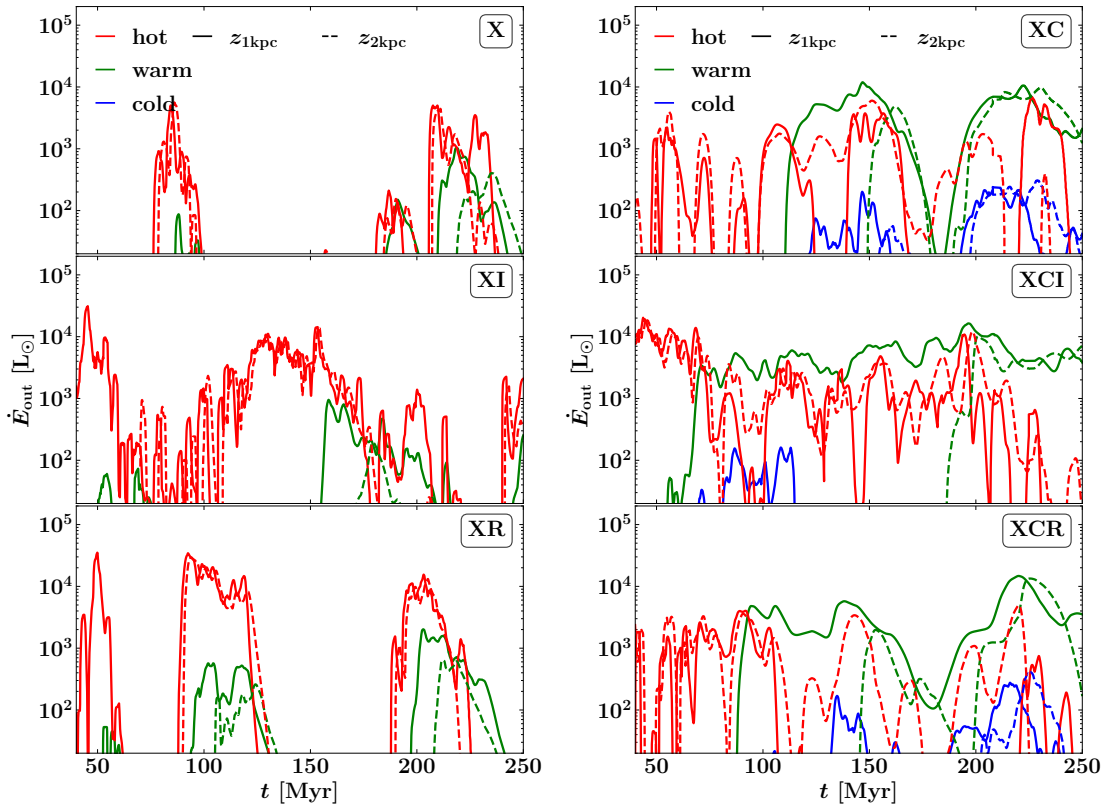

Figure 3.7: As in Fig. 3.6 but for the energy outflow rates, $\dot{E}_{\mathrm{out}}$. *Left* Almost all energy carried out of the ISM through the outflows is in the thermal hot phase and an equal amount of energy streams through $|z| = 1\,\mathrm{kpc}$ as through $|z| = 2\,\mathrm{kpc}$. *Right* An approximately equal amount of energy is carried out of the ISM in the hot gas-phase as in the warm gas-phase through $|z| = 1\,\mathrm{kpc}$.

3.5.3 Loading factors

We are analysing the mass- and energy loading factors at a height of $|z| = 1\,\mathrm{kpc}$ in Fig. 3.9. We are using the same definition for the loading factors as in Chapter 2, Sec. 2.6.1 and Sec. 2.6.2, which is the ratio of the instantaneous total mass outflow over the globally averaged SFR for the mass loading factor, and the ratio of the instantaneous total energy outflow over the globally averaged energy injection from SNe for the energy loading. We could have chosen to split the loading factors into distinctive periods (see Fig. 3.3), but since the average SFR during the transient and outflowing periods are so similar to the global average, we kept the global averaged SFR for simplicity. The most consistent outflows in energy and mass are driven by models with type Ia SN component (**XI**, green lines in Fig. 3.9 and **XCI**, yellow in Fig. 3.9). Runaway stars have the strongest impact on the outflow. We summarise the averaged loading factors in Table 3.4. The loading factors in the long-term evolution of the ISM simulation presented in this chapter differs in some aspects from the short-term evolution of up to $t = 100\,\mathrm{Myr}$ presented in Chapter 2. The average mass loading factor in **X** (= *SWR* in Chapter 2) increases from ~ 0.07 to ~ 0.57. In a similar way, but to a much larger extent, η also increases in **XC** (= *SWRC*) from ~ 0.02 to

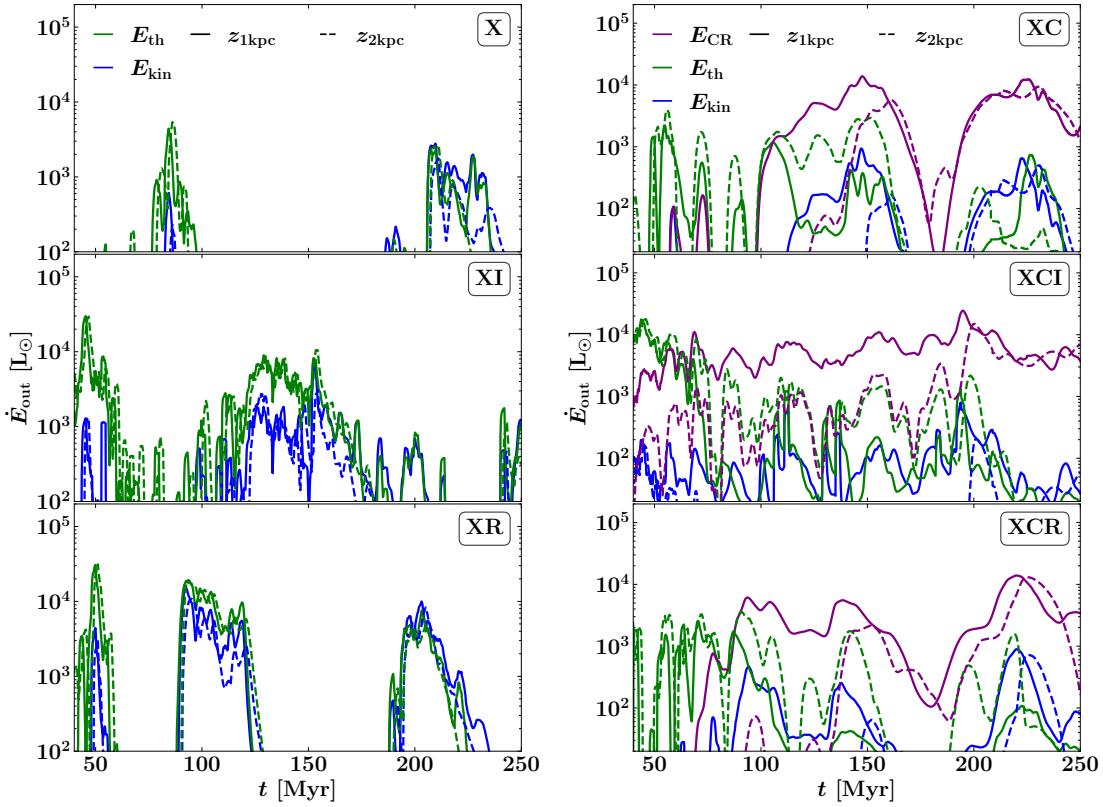

Figure 3.8: *Left* Energy outflow rates, $\dot{E}_{out}$, split up into the different energy components. The thermal and kinetic energy is in equipartition suggesting turbulent, hot, fast-moving outflow. Compare with the more structured outflow in the first three panels of Fig. 3.1. *Right* The kinetic energy component plays a subordinate role compared to the thermal energy, suggesting a a less turbulent and slower moving outflow. The most dominant component in the outflow is the CR energy, E_{CR}. After the CR pressure gradient is fully built up, an equal amount of CR energy diffuses with a short delay through $|z| = 1$ kpc as through $|z| = 2$ kpc.

~ 2.64. This does not come as a surprise. The SFR in models including the crucial ionising UV radiation as early stellar feedback is low and the ISM needs a longer time to self-regulate. The simulations with radiation are still too much influenced by their initial conditions within the first 100 Myr.

Table 3.4: Mass- and energy loading factors averaged over the full range of star formation from $t \sim 20 - 250$ Myr.

	X	XI	XR	XC	XCI	XCR
η_{1kpc}	0.57	0.93	1.58	2.64	2.87	3.21
γ_{1kpc}	0.01	0.04	0.09	0.13	0.14	0.11

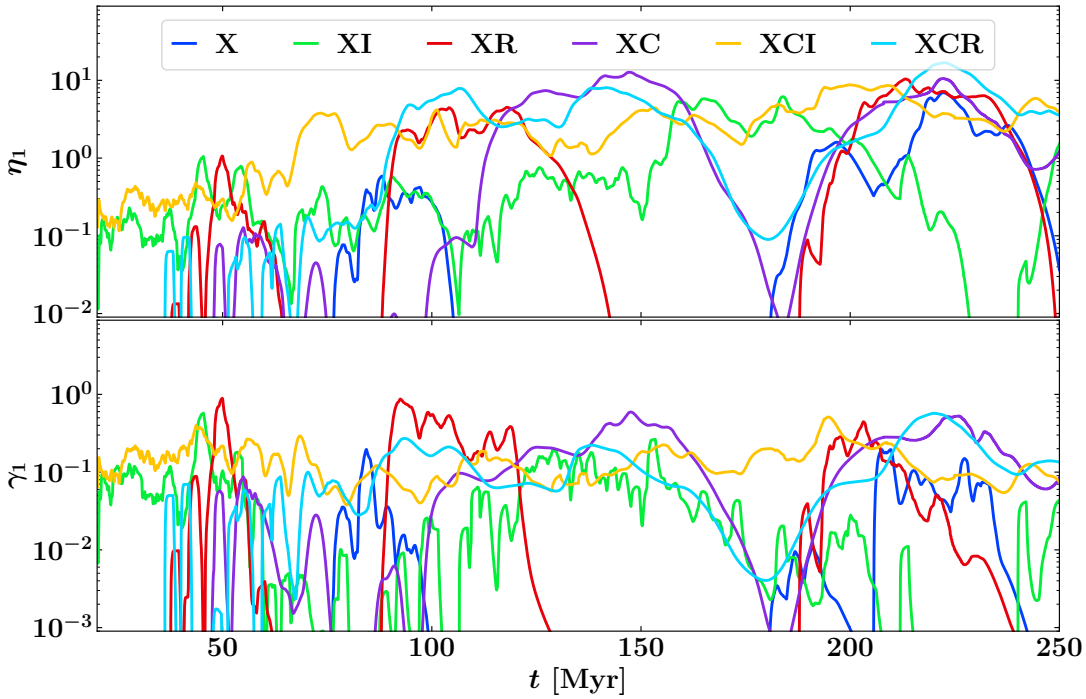

Figure 3.9: *Top panel* Mass loading factor, η_1, measured at $|z| = 1\,\mathrm{kpc}$ as the ratio of the instantaneous outflow rate over the average SFR for all six models. A mass loading above unity means that more gas is leaving the system than it is turned into stars, eventually depleting the gas reservoir. The models without CRs only drive episodic outflows (blue, green and red lines). *Bottom panel* Energy loading factor, γ_1, measured at $|z| = 1\,\mathrm{kpc}$ as the ratio of the instantaneous energy outflow rate over the average energy injection rate by all SNe. The models **XI** and **XCI** have the highest energy injection into the ISM due to the additional type Ia SN component, however, only the models with the CR supported outflow archive constant energy loading factors of $\sim$ 10 per cent.

3.5.4 Structure of the outflows

In the following section, we show the structure and composition of the mid-plane ISM and of the outflow region up to $|z| < 1$ kpc. In Fig. 3.10 shows the energy densities, u. In simulations without CR, the magnetic, kinetic and thermal energy densities are in balance like expected from ISM observations (see e.g. Draine, 2010). The values are slightly higher than in observations (and as in Chapter 2, Table. 2.4). This is because here we are showing the average energy density up to $z_{1\mathrm{kpc}}$, and not just in the mid-plane ISM as in the previous analysis. The behaviour of the kinetic, magnetic, and thermal energy density is the same in the CR runs. Nevertheless, the total energy density in the CR runs is about a factor of 5 higher $u \approx 5\,\mathrm{eV\,cm^{-3}}$ due to the large contribution in CR energy. The CR energy density gradually builds up and saturates after approximately $t \approx 100$ Myr. In the type Ia run (**XCI**), the CR energy density saturates faster due to the additional acceleration of CR in the type Ia SN remnants. The overall CR energy density in this run is about a factor of 2 higher than in **XC** and **XCR**, coinciding with the twice as high overall SNR (see Fig. 3.4 and Table 3.3). This large additional energy reservoir in the CR runs is responsible for sustaining large-scale and long-lived outflows (see also Fig. 3.3).

In Fig. 3.11, we show the volume-filling fractions of the hot (top panel), warm (middle panel), and cold (bottom panel) gas-phase in the region up to $|z| < 1$ kpc. Please note the change in scale in the bottom panel for the cold gas-phase. Due to the low SFR, all models are still influenced by the initial conditions up to $50 - 100$ Myr. Most of the volume in the CR runs is dominated by the warm gas-phase and even up to 1 per cent by the cold gas-phase. The simulations neglecting CR are periodically changing between a mainly hot and a mainly warm gas-phase volume-filling. Counter-intuitively, **XI** with the overall highest SNR from the six simulations studied in this work does not have the highest averaged hot gas volume-filling factor. It is true that the type Ia background provides a constant SNR throughout the simulation, but this rate is still fairly restrained with SNR $= 3\,\mathrm{Myr^{-1}}$, and spread out in the entire ISM + outflow region $|z| < 1$ kpc. Those SNe fuel the hot gas-phase and keep pushing gas out of the mid-plane but in a very stable and moderate way. **XR**, including runaways but without type Ia SNe, behaves differently. There is no support to lift gas away from the mid-plane in episodes without star formation. A fountain flow settles in (compare with Fig. 3.3). All the gas which falls back onto the disk compresses in the mid-plane and triggers a starburst. The resulting SNe are highly concentrated in space and time, even when the overall SNR stays below the one of *XI*. Those overlapping SNe generate peaks in the hot gas volume-filling factors which drive stronger outflows. This keeps the question of why a similar situation does not occur with **X**. The difference occurs because of the very first few runaway stars. In more detail, the runaway stars explode on average in a denser environment than their parent cluster and the thermal energy injected by them couples less efficiently to the ISM gas dynamics. However, the very first runaway stars ejected via DES at the birth of the parental star cluster can propagate into low-density regions end explode there. This is also seen in the ambient density distribution in Fig. 3.4. A small number of DES SNe explode in very low densities around $n \approx 10^{-5} - 10^{-4}$. This generates an extensive hot phase early on (the first peak in the red line in the upper panel of Fig. 3.11). This hot phase in hand drives an outflow which at some point cools, halts, and falls back onto the mid-plane. Resulting from the compression, an - albeit minor - starburst follows which then again drives another fountain flow. This minor

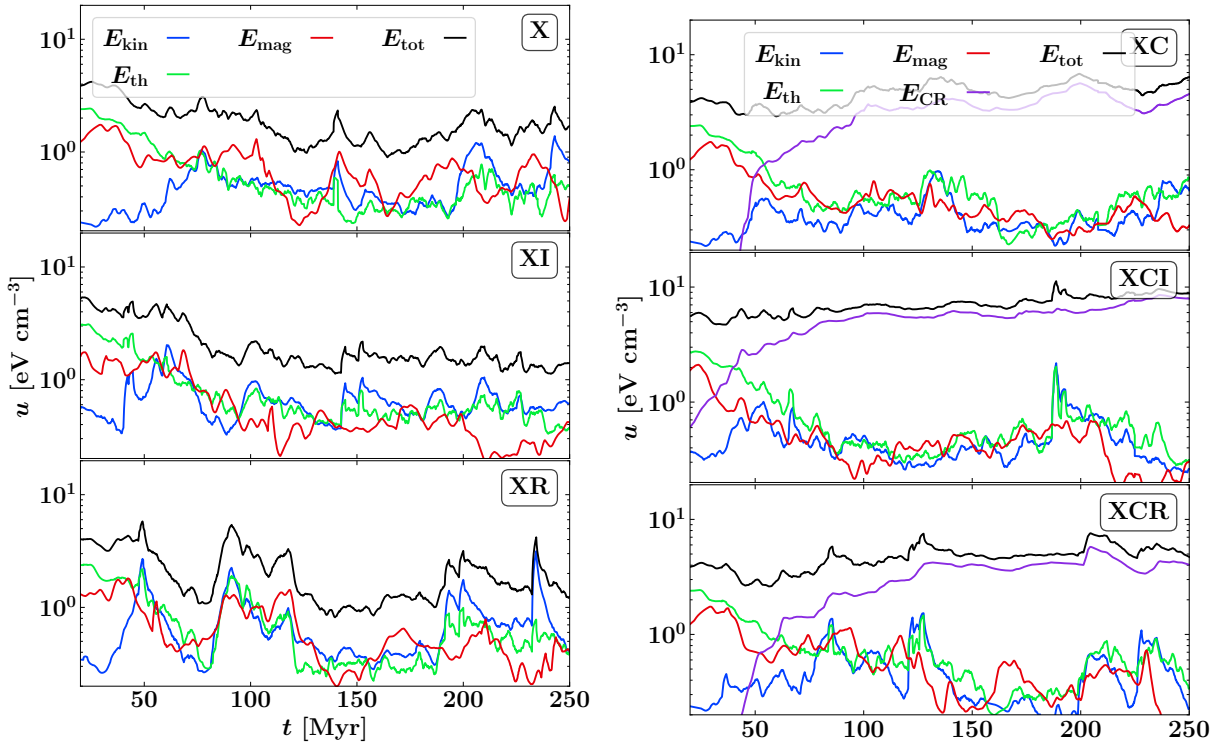

Figure 3.10: Energy densities, u, of the full mid-plane plus outflow region equal to $|z| < 1$ kpc. The black line shows the total energy density whereas the blue, green and red line show the kinetic, thermal and magnetic energy densities, respectively. After $\sim$ 100 Myr, the ISM and extended outflow region settles into an equilibrium state around an total energy density of $u \approx 2-3$ eV cm^{-3}. The CR energy density builds up over a timescale of $\sim$ 100 Myr and then saturates, even though there is a constant acceleration of more CR via SNe, especially in the type Ia model **XCI**.

starburst is also seen in the SFR analysis in Fig. 3.2. In **XR**, shortly before $t = 100$ Myr, there is a strong peak in Σ_{SFR}, followed by an extended outflow periods indicated by the blue shading. Similar trends appear in runs with CR but on a larger time-scale. The periodicity of the fountain flows is longer and the episodes of extended star formation due to compression of gas which falls back onto the mid-plane are less.

Similar to the analysis in Chapter 2 (see Fig. 2.15), we show the average mass loading through $|z| = 1$ kpc, η_{1kpc} as a function of the average hot gas volume-filling factor, VFF_{hot} in Fig. 3.12. However, this time, we are not averaging over the whole computed time, but only take into account values during outflow periods. We aim to analyse the conditions of the outflow during the outflow periods. By doing so, the values presented here are inflated compared to the previous study in Chapter 2, Fig. 2.15. The error bars in the figure represent a standard deviation of 1σ. The largest VFF_{hot}, but also the - by far - largest spread in VFF_{hot}, is present in **XR**. In hand, **XR** drives a strong outflow with an average $\eta_{1kpc} \approx 2-10$. We explained in Fig. 3.11 how **XR** reaches this larger VFF_{hot} compared to **XI** and **X**. The CR runs sustain a similarly η_{1kpc}, if not even larger in the case of **XCR**. However, VFF_{hot} is significantly smaller and close to each

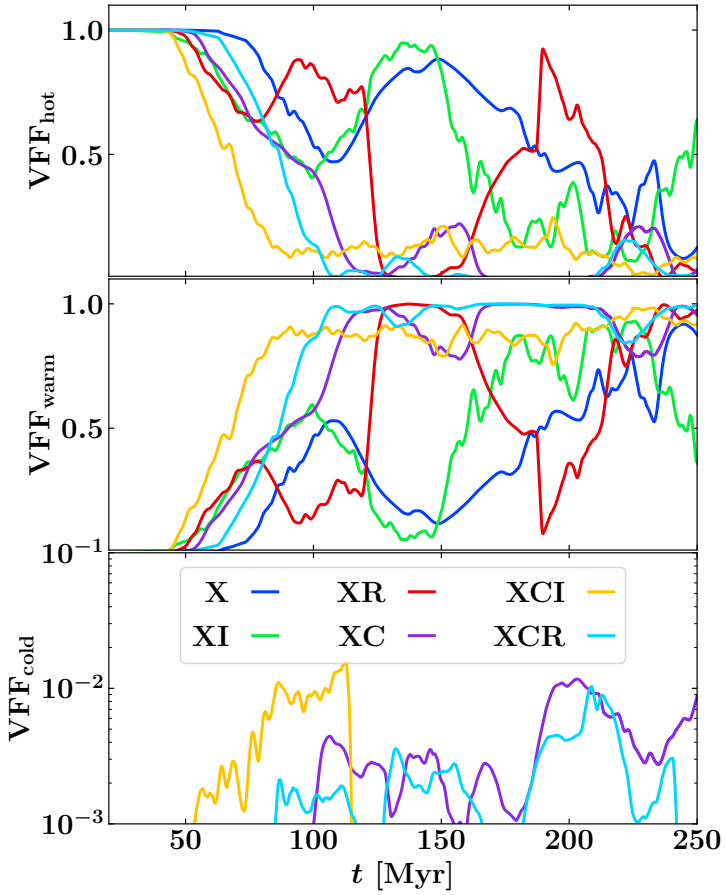

Figure 3.11: Volume-filling factors (VFF) of the outflow region (250 pc < $|z|$ <= 1 kpc) for the hot (top panel), warm (middle panel) and cold (bottom panel) gas-phases. The VFF of the cold gas-phase is negligible, although it reaches peak values around 1 per cent in the CR runs (purple, yellow and cyan line in the bottom panel). During the distinctive outflow periods (see Fig. 3.3) the VFF of the warm gas-phase lies between 85 – 95 per cent while the non-CR runs have a hot gas VFF during outflow periods of 35 – 50 per cent.

other in all three CR runs. The process behind how **XCR** and **XR** archive the highest mass loading factors during outflow periods is the same. However, the fountain flows in the CR run have a longer turnover time and less VFF$_{\rm hot}$ is needed to fuel the outflow. Instead, the outflow is sustained by the long-lived additional CR pressure gradient.

3.5.5 Outflowing gas velocities

The last aspect of the outflow we want to analyse in this work is the gas velocity of the outflow. We are calculating the mass-weighted velocity of the outflowing gas, averaged over the full $|z|$ = 1 kpc and $|z|$ = 2 kpc plane, respectively. This means we are only considering gas with positive z-velocity, v_z, above the disk and negative v_z below the disk. We then collect all snapshots

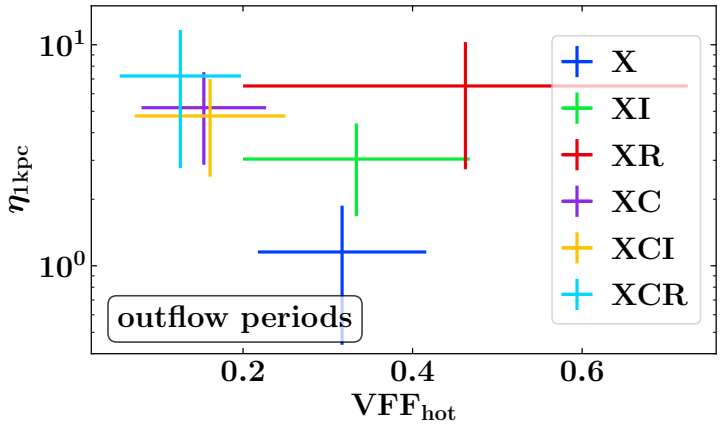

Figure 3.12: Mass loading through the $|z| = 1$ kpc boundary, η_{1kpc} as a function of the hot gas volume-filling factor VFF_hot in the mid-plane plus outflow region up to $|z| < 1$ kpc, averaged exclusively over periods of extended outflow (see Fig. 3.3 for definition). The error bars indicate a standard deviation of 1σ. The largest average VFF_{hot}, but also the largest spread - is present in **XR**. Coming from this is also a high average $\eta_{1kpc} \approx 2 - 10$. CR sustained outflow reaches mass loading factors comparable to **XR**, but with a significantly lower VFF_{hot}. It is important to keep in mind that the values presented here are only showing periods of strong outflows and are therefore to an extent inflated compared to the results from the previous chapter, Fig 2.15. The idea behind this analysis was not to show globally averaged quantities but to present the conditions of outflow during outflow periods.

(with a time resolution of $dt = 0.1$ Myr) which have a net positive outflow and compile the space-averaged, mass-weighted outflow velocities into a box-plot diagram (Fig. 3.13). We group the results for the outflow through z_{1kpc} and z_{2kpc} for each simulation next to each other. The green lines indicate the median outflow velocity and the red lines the mean outflow velocity. The boxes contain 50 per cent of the data. This means that in 50 per cent of the time an outflow occurs, sampled with a time resolution of $dt = 0.1$ Myr, the mass-weighted outflow velocity lies between the upper and the lower boundaries of the black boxes. The antennas have a length of $2 \times IQR$ (interquartile-range), i.e. 2 times the difference between the upper and the lower boundary of the boxes. Outliers, i.e. snapshots with an outflow velocity larger than $2 \times IQR$, are indicated with hollow circles. The horizontal dashed line marks an outflow velocity of 550 km s^{-1}, which is the escape velocity of the Milky Way at solar radius (Kafle et al., 2014).

The mean and median, as well as the spread in outflow velocity increases from the $|z| = 1$ kpc to the $|z| = 2$ kpc boundary for the simulations without CR. It is important to understand that this does not mean that the gas accelerates between z_{1kpc} and z_{2kpc}. There is no process or mechanism which can accelerate that gas further between those boundaries. Even the type Ia SN with the largest distance to the mid-plane explodes at $|z| \approx 800$ pc. The mass-weighted outflowing gas at z_{2kpc} is faster than at z_{1kpc} because the slow-moving, warm gas-phase which is still present at z_{1kpc} does not efficiently reach those heights. The gas which makes it through z_{2kpc} is only the sparse, very hot, very fast-moving gas. Again, the picture is drastically different for the models including

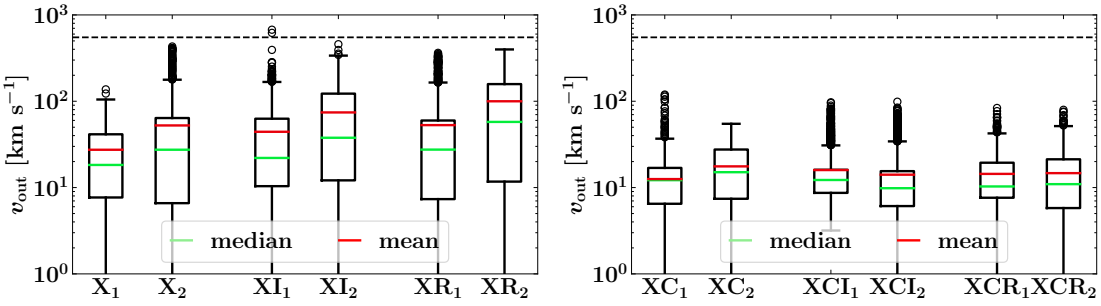

Figure 3.13: *Left* Boxplots of the mass-weighted outflow velocities, $v_{\rm out}$, at the $|z| = 1$ kpc and $|z| = 2$ kpc boundaries (denoted by a subscript 1 and 2, respectively). The green line indicates the median mass-weighted velocity of the outflowing gas, whereas the red line indicates the average mass-weighted velocity. The boxes contain 50 per cent of all data (25$^{\rm th}$ and 75$^{\rm th}$ quartile) and the antennas have the length of 2 × IQR (interquartile-range). Outliers are marked as black circles. The black dashed line indicates an outflow velocity of $v_{\rm out} = 550\,{\rm km\,s^{-1}}$, which is the typical escape velocity of the Milky Way at solar radius (Kafle et al., 2014). The average velocity of the outflowing gas increases from the $|z| = 1$ kpc to the $|z| = 2$ kpc boundary. This makes sense since only the hot, very fast-moving gas component reaches this height and the slower moving, warm gas-phase outflow, which is still present to a smaller extent at the $|z| = 1$ kpc boundary, is already falling back into the mid-plane ISM. Nonetheless, only scattered outliers of the hot gas-phase component reach high enough velocities to leave the system entirely and will fall back onto this disk over time, creating a fountain flow. *Right* mass-weighted outflow velocities, $v_{\rm out}$, for the CR runs. The outflow present in the models including CRs are slower and have a smaller spread than their non-CR supported counterparts (Fig. 3.13, left panel). On average, approximately 10 – 20 per cent of the total gas mass streaming through the $|z| = 1$ kpc boundary also reaches heights of $|z| = 1$ kpc (compare with Fig. 3.6, right panel) with the same velocity distribution, accelerated by the saturated and long-lived CR pressure gradient.

CR (right panel of Fig. 3.13). The median of the mass-weighted outflow velocity is a factor ∼ 2 smaller at about $v_{\rm out} = 10\,{\rm km\,s^{-1}}$ and it has a much smaller spread than the counterparts without CR. Additionally, there is no significant change in the outflow velocities between the $z_{\rm 1kpc}$ and $z_{\rm 2kpc}$ boundaries in the CR models. CR supported outflows are relatively slow, but very steadily propagating. However, none of the CR sustained outflows reach escape velocity in the least. In periods of low star formation, the outflow will ebb down and a large-scale fountain flow with a long turnover time establishes.

3.6 This work in context

The inclusion of runaway stars into high-resolution ISM simulations with self-consistent star formation and complex stellar feedback, extending beyond just thermal feedback from SNe, but also considering stellar winds and - especially - early radiative feedback, has not been accounted for by many ISM simulation frameworks. Nonetheless, we wish to highlight the TIGRESS simulation

suite (Kim & Ostriker, 2017, 2018), as well as recent work by Andersson et al. (2020).

Kim & Ostriker (2017) implement runaway OB stars with BSS ejection and neglect DES. They enforce a binary fraction of OB stars of $f_{\rm bin} = 0.66$ and whenever the primary star of a binary system undergoes a SN explosion, the secondary star is ejected with an isotropic velocity distribution according to a binary population synthesis model with a characteristic velocity of $50\,{\rm km\,s^{-1}}$(Eldridge et al., 2011). Overall, they find that runaway stars only marginally impact the evolution of the ISM and a larger proportion of high-velocity runaway stars would be needed to significantly alter the mass and energy loadings in their simulations. That said, their overall SFR is also a factor of ~ 3 higher than in our models including early feedback. The resulting higher SNR could be enough to generate a large $\rm VFF_{hot}$ which drives warm fountain flows and hot galactic winds so that the impact of runaway stars is indeed negligible.

To a contradicting result come Andersson et al. (2020). They simulate full Milky Way-like galaxies and find that runaway stars in their model nearly double the number of SNe in low-density environments ($10^{-5} < \rho < 10^{-3}$) and that the mass loading factor measured at a height equal to 0.025 times the virial radius of the galaxy increases by an order of magnitude from $\eta \approx 0.5$ to $\eta \approx 5-10$. This result is closer to our findings that the runaway stars boost the mass loading by a factor of ~ 3 from **X** to **XR** and roughly by 20 per cent in the CR runs from 1.58 in **XC** to 3.21 in **XCR**. However, Andersson et al. (2020) find the influence of runaway stars greatly exaggerated compared to our results. Some major differences between their models and ours are: (*a*) The AMR resolution is coarser ($dx_{\rm max} = 8\,{\rm pc}$) because they try to model a full galaxy and not just a galactic patch like we do within the SILCC framework, (*b*) They sample their star-formation from a Kroupa IMF (Kroupa, 2001) - like we do - in a mass range up to $M_\star = 120\,{\rm M_\odot}$, but they discard stars heavier than $40\,{\rm M_\odot}$, arguing that those stars are very rare and their lifetimes short, resulting in a shorter travel distance of the runaways. However, this is a quite crucial point in the realisation of runaways. Andersson et al. (2020) quote an average travel distance of runaways of $d \approx 350\,{\rm pc}$, where we have a shorter distance above/below the mid-plane of $z_{\rm rnw} \approx 200\,{\rm pc}$. We argue an artificial cut-off in the maximum mass of the potential formed runaway stars is nonphysical and creates a bias towards far-travelling runaway stars. (*c*) Andersson et al. (2020) realisation of runaways mimics only the DES mechanism. More evolved runaway stars, which would be launched by BSS, are neglected. This, in hand, increases the lifetime and travel-distance distribution of the runaway stars, again. ((d)) They do include type II SNe and stellar winds but do not account for early feedback in the form of radiation. In addition, they do not report on strong stellar clustering. They mention that their runaway stars leave the dense star-forming regions in their simulations. However, in Chapter 2, we find that as soon as star formation sets in, the environments of the star cluster quickly disperse, the latest when the first SNe explode. Subsequent SNe will go off in a rarefied medium. Runaway stars, especially at later stages in the simulation, travel into regions of more pristine gas and deposit their thermal SNe energy in denser environments. Andersson et al. (2020) acknowledge most of the limitations of their model and stress that their results are first approximations as to how runaway stars affect the physical processes in a full galaxy simulation.

3.7 Summary

In this chapter, we have build upon the results from Chapter 2 and studied the long-term (t = 250 Myr) evolution of CR-supported galactic outflows, as well as the influence of an extended SN component via type Ia SNe and the impact of massive runaway O stars. The expected trends which became apparent in the previous chapter towards the end of the short-term simulations *SWR* and *SWRC* have been confirmed. CR can sustain an long-lived, cool and slow-moving outflow with mass loading factors between $\eta \approx 2.5 - 3.5$ and energy loading factors $\gamma \approx$ 10 per cent. The outflow velocities are around $v_{\mathrm{out}} \approx 10\,\mathrm{km\,s^{-1}}$. This is not fast enough to leave the gravitational potential of the disk and the outflowing gas will fall back onto this disk over time. A warm gas fountain flow with a long turnover time, $t_{\mathrm{to}} \approx 70$ Myr, establishes. The results indicate a qualitative change in the assessment of the impact the runaway stars have on the formation of the ISM and the galactic outflows. We model runaway stars produced by both observationally motivated ejection scenarios, the dynamical ejection scenario (DES Poveda et al., 1967) and the binary supernova scenario (BSS Blaauw, 1964), a observationally motivated velocity distribution of $\sigma_{\mathrm{rnw}} = 30\,\mathrm{km\,s^{-1}}$ (Stone, 1991), and a observationally motivated runaway star fraction $\sim 10 - 20$ per cent (Tetzlaff et al., 2011; Maíz Apellániz et al., 2018). Contrary to common assumption, our experiments suggest that runaway stars in a fully developed ISM do not explode in rarefied environments, but in denser environments, with ambient densities up to an order of magnitude higher than in their parent star clusters. However, they influence the evolution of the ISM early on and imitate a fountain flow earlier than simulation counterparts without runaway stars. This leads to a gas compression in the mid-plane ISM when the fountain flow falls back onto the disk, driving a periodical outflow. Nonetheless, the dynamically strongest impact is provided by the CR rays, which can drive and sustain galactic fountain flows with hot gas volume-filling factors as low as $\mathrm{VFF_{hot}} \approx 15 - 20$ per cent.

Chapter 4

Optical emission line diagnostics for the simulated interstellar medium

In this chapter, we introduce ELD (**e**mission **l**ine **d**iagnostics), a tool to predict (optical) emission lines for the simulated ISM. We apply this tool to a set of our simulations, analyse the results with emission line ratio diagrams (known as BPT diagrams, Baldwin et al. (1981)) and compare our models against observations. This chapter will be submitted for publication in *Mon. Not. R. Astron. Soc.*

4.1 From ISM simulations to emission line diagnostics

To get from ISM simulations like the ones presented in Sec. 2 and Sec. 3 to emission line diagnostics we need to follow three steps:

1. *Read out the simulation*

   For every gas cell in the adaptive mesh refinement (AMR) ISM simulation we record various properties: its position in x, y, z, the hydrogen density, n_{H}, the gas temperature, T, the dust temperature, T_{dust}, the radiation energy and the density of ionising photons, n_{γ}, self-consistently provided by the radiative transfer tool TreeRay (see Sec. 2.1 and Wünsch et al., 2021, for details), and the necessary input parameters to model the shape of the spectrum (see Sec. 4.1.2). We collect this information in a database and group together simulation cells with close to similar parameters to a *model* with a unique identifier. By doing so, we vastly reduce the amount of unique models which have to be accounted for in the post-processing by a factor of ~ 10 to roughly 10^5 models for each snapshot of a simulation.

2. *Feed the input into Cloudy*

   Next, we provide the unique models of the simulation as input parameters for the self-consistent, 1D photo-ionisation code Cloudy (version C17, Ferland et al., 2017). Cloudy is used to simulate the physical conditions of HII regions, active galactic

nuclei and photo-dissociation regions. It has a wide range of micro-physics and molecular physics included and can predict the thermal, ionisation and chemical state of clouds, as well as their observed spectra. To do so, Cloudy needs to know the shape and intensity of the incident radiation field, the chemical composition and the geometry of the system. The normal use-case simulating an HII region, for example, is to set a certain gas density structure and ionisation source. The source can be defined via its luminosity or indirectly via a dimensionless ionisation parameter

$$U = \Phi \cdot n_{\mathrm{H}}^{-1} \cdot c^{-1} = n_{\gamma} \cdot n_{\mathrm{H}}^{-1}, \tag{4.1}$$

with the ionising photon flux, Φ, the speed of light, c, the hydrogen density, n_{H} and the density of ionising photons, n_{γ}. Cloudy then divides the setup into multiple equally sized zones and iteratively solves the 1D radiative transfer equation along the zones until convergence. The thickness of the zones is adaptively chosen by Cloudy to be small enough so that the physical conditions across them are nearly constant. We use Cloudy in a different way for our post-processing. Instead of defining entire HII, regions we provide Cloudy with the gas- and radiation structure of the unique models generated from the ISM simulation. We set the gas density and temperature for each Cloudy simulation to the fixed value coming from the ISM simulation and do not allow Cloudy to evolve those parameters. In the normal use-case, Cloudy would use the self-consistently evolved gas temperature as a stopping criterion. As soon as a zone converged to a temperature below $T_{\mathrm{stop}} = 4000\,\mathrm{K}$, Cloudy would assume to have reached the end of the HII region and stops the calculation. For Cloudy to know when to stop the calculation we have to define the maximum physical size of the model, which is set to the size of the gas cell from the simulation ($dx = 4\,\mathrm{pc}$ in all of our ISM simulations). We also provide Cloudy with the radiation intensity in the gas cell and the shape of the spectrum. We use the Cloudy internal options to add an interstellar radiation field background (ISRF) with adaptive G_0, depending on the initial gas surface density of the ISM simulation, with $G_0 = 1.7$ for $\Sigma_{\mathrm{gas}} = 10\,\mathrm{M}_{\odot}\,\mathrm{pc}^{-2}$ (Draine & Bertoldi, 1996). Also, we add a cosmic microwave background (CMB) component, in addition to the UV radiation proved from the massive stars in our simulations. Furthermore, we add a cosmic ray ionisation rate[1] for neutral atomic hydrogen of $\zeta_{\mathrm{H}} = 3 \times 10^{-17}\,\mathrm{s}^{-1}$ (Goldsmith & Langer, 1978), a micro-turbulent velocity field, $v_{\mathrm{turb}} = 5\,\mathrm{km\,s}^{-1}$, which affects the shielding and pumping of lines, and dust grain physics including sublimation and metal depletion with a fixed dust-to-gas ratio of 1 per cent. We adopt solar metallicity with the same abundances and depletion factors as compiled in Gutkin et al. (2016), based on the works by Caffau et al. (2011) and Bressan et al. (2012) (see Table 4.1). With that input, Cloudy calculates the ionisation states of the species and predicts the strength of the line emission, as well as the continuum emission for every single model.

[1]Even though we do have acceleration and diffusion of CR included self-consistently in our simulations, they are not coupled directly to the chemistry network and do not provide a varying CR ionisation rate. Therefore, we chose to use a fixed CR ionisation rate based on observations.

3. *Process the output*

After CLOUDY is finished, we collect the predicted emission strength of the optical lines and continuum emission of each unique model. To undo the slight loss of information when we bin the individual gas cells of the ISM simulation into unique models, we take the predicted emission for the models and interpolate the result to the actual gas cell properties using the piece-wise, linear interpolation algorithm QHULL (Barber et al., 1996). We then map the emission onto the 3D space of the ISM simulation. Observers, however, cannot measure the emission in 3D space. Therefore, we integrate all emission along a sight-line, seeing the ISM patch face-on (i.e. seeing the $x-y-$ plane and integrating along the $z-$ direction). To account for the fact that the medium is generally not optically thin, we also consider attenuation along the line-of-sight using dust opacity models by Draine (2003). On average, the dust attenuation leads to a decrease in measured line strength of $\sim 5-10$ per cent compared to the predicted emission of each cell. For some sight-lines, however, the attenuation was as strong as 70 per cent. Each line-of-sight has a beamwidth of 4 pc, equal to the grid resolution of the simulation. From this, we can construct emission maps with 128×128 pixels (based on the box size of our ISM simulations of $L_x = L_y = 500$ pc with a resolution of $dx \approx 4$ pc). We show an emission map in Fig. 4.9 and also investigate the impact of larger beamwidths in Sec. 4.2.4.

Table 4.1: List of the interstellar abundances relative to hydrogen, $n_i/n_{\rm H}$, and metal depletion factors, $f^i_{\rm dpl}$, i.e. the fraction of an element i depleted onto dust grains, used for the post-processing with ELD, adopted from Gutkin et al. (2016).

Element	$\log_{10}(n_i/n_{\rm H})$	$(1 - f^i_{\rm dpl})$	Element	$\log_{10}(n_i/n_{\rm H})$	$(1 - f^i_{\rm dpl})$
H	0	1	S	-4.87	1
He	-1.01	1	Cl	-6.53	0.5
Li	-10.99	0.16	Ar	-5.63	1
Be	-10.63	0.6	K	-6.92	0.3
B	-9.47	0.13	Ca	-5.67	0.003
C	-3.53	0.5	Sc	-8.86	0.005
N	-4.32	1	Ti	-7.01	0.008
O	-3.17	0.7	V	-8.03	0.006
F	-7.47	0.3	Cr	-6.36	0.006
Ne	-4.01	1	Mn	-6.64	0.05
Na	-5.70	0.25	Fe	-4.51	0.01
Mg	-4.45	0.2	Co	-7.11	0.01
Al	-5.56	0.02	Ni	-5.78	0.04
Si	-4.48	0.1	Cu	-7.82	0.1
P	-6.57	0.25	Zn	-7.43	0.25

4.1.1 Tests with idealised HII regions

To benchmark and test our post-processing approach we have simulated single HII regions in a controlled setup and applied ELD to them. The idealised simulations are carried out within the SILCC code framework, the same as for the simulations from Sec. 2 and Sec. 3. We place a single star cluster sink particle with mass $M_{\rm cl} = 10^4\,{\rm M}_\odot$ in a homogeneous medium with a mass density $\rho = 2.1 \times 10^{-22}\,{\rm g\,cm^{-3}}$ ($n_{\rm H} \approx 100\,{\rm cm^{-3}}$) and temperature $T \approx 100\,{\rm K}$. We chose this cluster mass for our test experiments as $10^4\,{\rm M}_\odot$ marked to be an upper limit of the cluster mass in our full-scale ISM simulations (see Table 2.2). We let the system evolve for 1 Myr with four different grid resolutions ($dx = 0.5\,{\rm pc} - 4\,{\rm pc}$) and with different model assumptions. We only sample the massive stars in the central star cluster once from a Salpeter IMF (Salpeter, 1955) and use the same configuration for each run. In Fig. 4.1, we show visualisations for the $dx = 2\,{\rm pc}$ (top panels) and $dx = 0.5\,{\rm pc}$ (bottom panels) runs. From left to right, we show the hydrogen number density, $n_{\rm H}$, ionising photon number density, n_γ, and temperature, T.

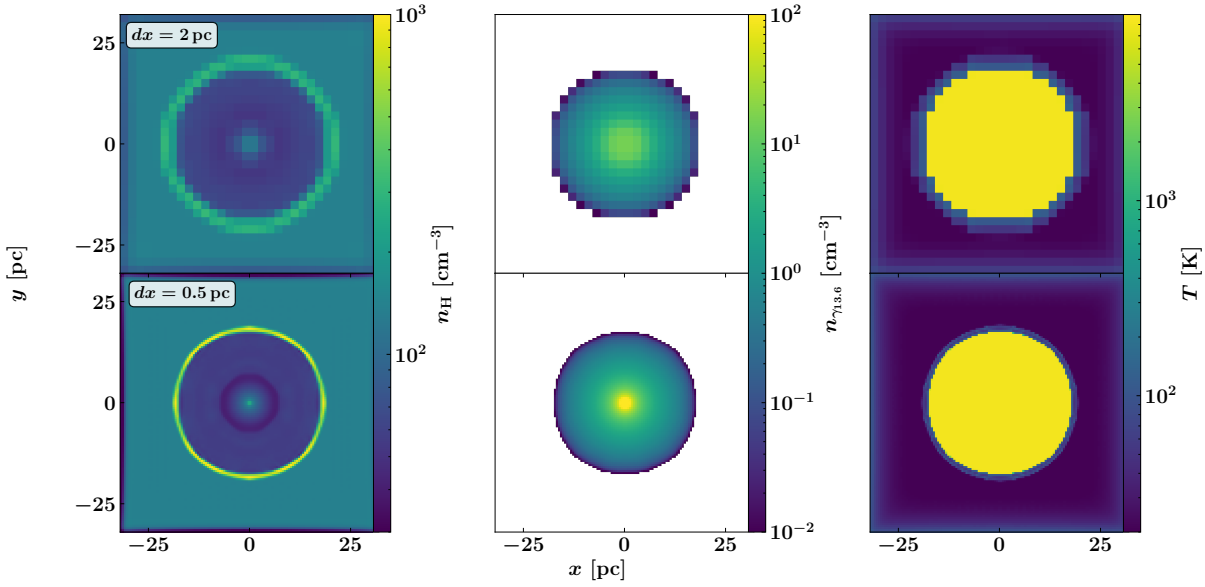

Figure 4.1: Visualisation of experiments with idealised HII regions in an homogeneous medium with ambient gas density $\rho = 2.1 \times 10^{-22}\,{\rm g\,cm^{-3}}$. The mass of the central star cluster is $M_{\rm cl} = 10^4\,{\rm M}_\odot$. Shown are slices through the centre for simulations with grid resolution of $dx = 2\,{\rm pc}$ (top row) and $dx = 0.5\,{\rm pc}$ (bottom row). From left to right: Hydrogen number density, $n_{\rm H}$, ionising photon density, n_γ, and temperature, T. The ionising radiation is able to heat up the HII regions to a typical temperature of $\sim 8000\,{\rm K}$.

After running the idealised experiments we apply our post-processing tool and create diagnostic line ratio diagrams (Baldwin et al., 1981) for the estimated emissions. In Fig. 4.2, we show the [N$_{\rm II}$] / Hα vs [O$_{\rm III}$] / Hβ diagram for the experiment with $M_{\rm cl} = 10^4\,{\rm M}_\odot$, $dx = 0.5\,{\rm pc}$ and using a single stellar population (SSP) model for the ionising spectrum (see Sec. 4.1.2 for more information). The solid black line is the theoretical Kewley et al. (2001) maximum starburst

line, based on the upper limit of purely stellar photo-ionisation models. The dashed black line is an empirical revision of the *Kewley+01* line to further distinguish star-forming galaxies from Seyfert galaxies (Kauffmann et al., 2003). Shown in grey in the background is observational data of nearby galaxies from the Sloan Digital Sky Survey, data release 7 (Abazajian et al., 2009). The galaxies are selected to be in a small redshift range of $0.04 \leq z \leq 0.2$ and with a high signal-to-noise (S/N) ratio for the line ratios. Throughout this chapter, we will always plot the classification lines and observational data into the BPT diagrams for reference. The hexbins, colour-coded with the bin count (Fig. 4.2, left panel), represent the emission line ratios of the individual gas cells in the idealised simulation. For reference, the simulated box consists of a total of $\sim 2 \times 10^6$ cells at a grid resolution of $dx = 0.5$ pc, out of which approximately 1.9×10^5 cells lie within the HII region. The width of the bins is chosen equal to 0.05 dex. The red star indicates the position of the line ratios of the HII region as a whole, i.e. $(\sum_{\text{cells}} [\text{N}_{\text{II}}]) / (\sum_{\text{cells}} \text{H}\alpha)$ vs $(\sum_{\text{cells}} [\text{O}_{\text{III}}]) / (\sum_{\text{cells}} \text{H}\beta)$. In the right panel of 4.2, we show the same experiment, but this time colour-coded with the average ionisation parameter, U, of the simulation cells. When creating the line ratios, we take into account only emission lines with an equivalent width, $EW = \int \frac{F(\lambda) - F_{\text{c}}(\lambda)}{F_{\text{c}}(\lambda)} d\lambda \approx \frac{F_{\text{line}}}{F_{\text{c}}(\lambda)}$, larger than 0.1Å. The optical line emission estimated by our post-processing tool ELD follows the sequence of star-forming galaxies sequence (Kewley et al., 2001; Kauffmann et al., 2003) and and is in good agreement with observations. A clear trend with increasing ionisation parameter is present, which is also predicted by theoretical models (Gutkin et al., 2016), as well as observations (Dopita et al., 2000; Moustakas et al., 2010).

4.1.2 The choice of the ionising spectrum

As described above (Sec. 4.1), one input parameter for the post-processing is the ionising spectrum. At its current state, the radiative transfer tool TreeRay (Wünsch et al., 2021) deployed in the SILCC framework and also used for this work provides one energy bin for the ionising photons, $h\nu = 13.6\,\text{eV}$. Therefore, we have to make assumptions to model the shape of the spectrum. At first approximation, the simplest approach is to model the spectrum of an individual star cluster as a black body with an effective temperature equal to the effective temperature of the most massive star in the cluster (*single BB* hereafter). This assumes that the radiation output of a cluster is dominated by its most massive star. The advantage of this approach is that the spectrum of every cluster can be modelled with just one single number, which makes the iterative procedure of ELD less computationally demanding. However, this assumption does generally not hold, especially not for the more massive clusters in our simulations. For example, the two most massive stars in the $M_{\text{cl}} = 10^4\,\text{M}_\odot$ cluster of the idealised HII region tests add up to only 30 per cent of the total UV luminosity of this cluster. The next improvement would be to model every massive star in each cluster as a black body and add those together (*stacked BB* hereafter). This increases the accuracy of the model, but also the computational load. Binning gas cells into groups with similar post-processing parameters - gas density, gas temperature, dust temperature, radiation energy density and information about the star cluster which irradiates the cell to calculate the shape of the spectrum - to decrease the number of unique models per snapshot becomes less efficient because every star cluster is now modelled with one spectrum per star it

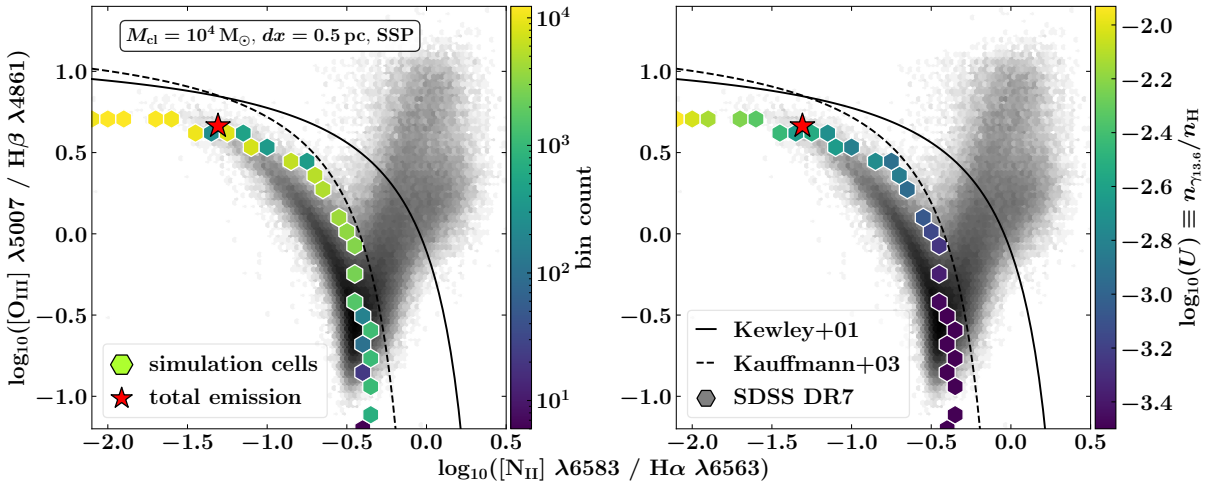

Figure 4.2: *Left* Classic BPT diagram (Baldwin et al., 1981) for a post-processed idealised HII region experiment with $M_{cl} = 10^4\,M_\odot$, $dx = 0.5$ pc and a radiation spectrum generated by a synthetic single stellar population (SSP) model. Shown in grey is optical emission line data from the Sloan Digital Sky Survey data release 7 (SDSS DR7, Abazajian et al., 2009). The solid and dashed black lines represent the maximum starburst limits by Kewley et al. (2001) and Kauffmann et al. (2003), respectively. The hexbins show how many grid cells from the idealised simulation populate certain regions in the BPT diagram, whereas the red star indicates the position of the line ratio of the total emission, i.e. the emission of all cells summed up. *Right* Same as left but colour-coded with the average ionisation parameter, U, in each bin, instead of the bin count. The emission from a single HII region follows the star-forming sequence with increasing ionisation parameter towards regions of high [OIII] and low [NII] emission, as it is also expected from theoretical models (see e.g. Kewley et al., 2019, for a review). Only emission lines with an equivalent width, EW, larger than 0.1Å are taken into account for generating the line ratios.

contains. The biggest shortcoming of the black body approaches, however, is that they stellar atmospheres and other processes like stellar mass loss and rotation in the modelling of the spectra. We ,therefore, improved upon the *stacked BB* ansatz and represented every star of a cluster not as a black body, but with their model atmosphere, using OSTAR2002 (Lanz & Hubeny, 2003), a comprehensive grid of non-LTE, line-blanketed, plane-parallel, hydro-static model atmospheres (*stacked atmospheres* hereafter). Doing so, we strongly increase the validity of our modelled spectra but still have the same problem of the higher computational load. To circumvent this issue we tested a fourth approach in which we model the total spectrum of a star cluster with a single stellar population synthesis model (*SSP* hereafter). We are using the latest version of Bruzual & Charlot (2003) (Charlot & Bruzual, in prep.), with updated spectra for Wolf-Rayet stars (Gräfener et al., 2002) and main-sequence massive stars (Chen et al., 2015). The stars in this model are at solar metallicity and sampled from a Kroupa IMF (Kroupa, 2001) with an upper mass cut-off of $m_{up} = 120\,M_\odot$ (see also Plat et al., 2019). Using a single stellar population model has the advantage that the predicted spectrum of the model is only dependent on the age of the cluster

and its mass. However, scaling the mass of the cluster up or down only impacts the intensity of the resulting spectrum, not its shape. Since the intensity of the radiation field is already provided to CLOUDY as input from our ISM simulations directly (via TREERAY), we only need to know the shape of the spectrum from *SSP* and therefore, we can model each star cluster just with one parameter, its age. This approach provides a more realistic and accurate model than the single black body approach but with no added computational cost.

In Fig. 4.3, we show the shape of the different realisations for the spectrum of the $M_{\rm cl} = 10^4\,{\rm M}_\odot$ cluster. Vertical black lines indicate ionisation energies for a selection of optical emission lines relevant to our study. The most striking difference is the lack of the Lyman break when modelling the spectrum with black bodies compared to the inclusion of stellar atmospheres. This leads to an over-production of photons around the Lyman limit, which coincides with the transition energy for $[{\rm N_I}] \rightarrow [{\rm N_{II}}]$, resulting in a higher $[{\rm N_{II}}]$ emission. The single stellar population model (*SSP*), which only takes the mass and age of the star cluster as an input, produces a remarkably similar spectrum to *stacked atmospheres*, which creates a model atmosphere for each star in the cluster.

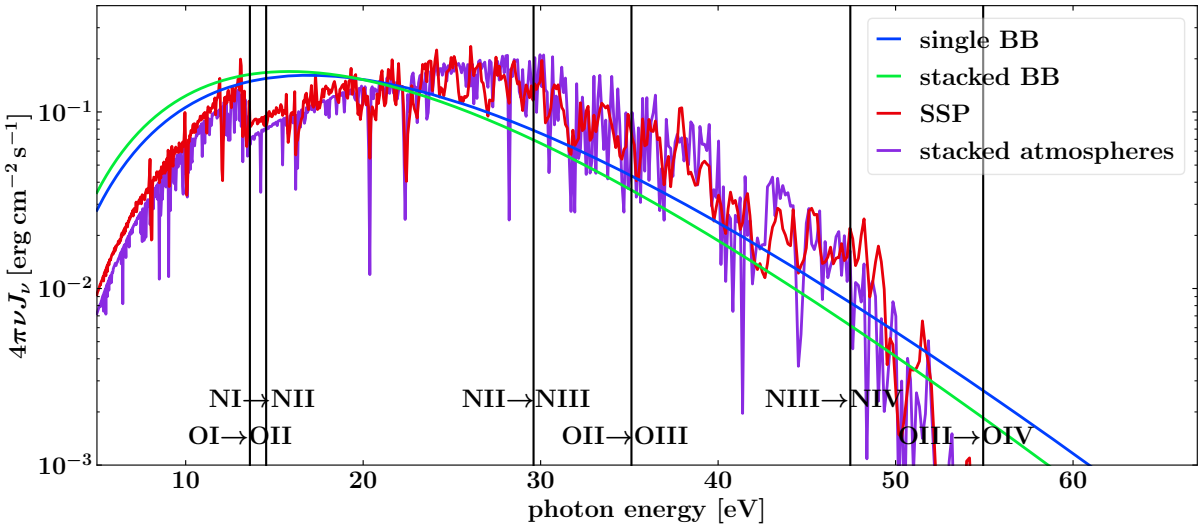

Figure 4.3: Exemplary electromagnetic spectrum for a $10^4\,{\rm M}_\odot$ cluster with four different realisations (see text). Vertical black lines indicate ionisation energies for different relevant species. An important difference between the single stellar population (SSP - red line) and the stacked stellar model atmospheres (purple lines) to the simplified black body assumption (blue and green lines) is the cut at the Lyman limit, which lies at the important transition for optical emission diagnostics of $[{\rm N_I}]$ to $[{\rm N_{II}}]$.

We show how the different choices for the spectrum affect the positions of the HII region in the BPT diagram in Fig. 4.4. As expected from Fig. 4.3, modelling the spectrum with just black bodies results in higher $[{\rm N_{II}}]$ and lower $[{\rm O_{III}}]$ emission, moving the position in the line ratio diagram to the right and the bottom. The output of Hα and Hβ is only marginally affected. Within an observational context, all four different realisations for the ionising spectrum of the star

cluster are sensible. We choose to use *SSP* for the post-processing of our high-resolution ISM simulations because it is the most sophisticated approach for the smallest computational cost.

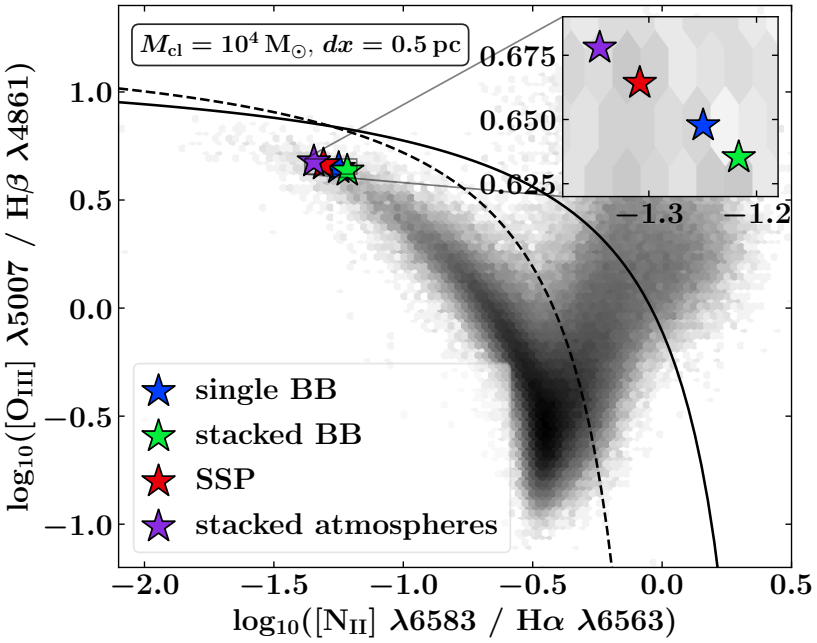

Figure 4.4: BPT diagnostics test for the idealised HII region with a $10^4\,M_\odot$ cluster with different spectra realisations (see Fig. 4.3). The stars represent the line ratios of the total emission. Models with the simple black body assumption have up to 25 per cent more emission in [N_{II}], and 10 per cent less in [O_{III}], explaining the shift to the lower right within the BPT diagram compared to the otherwise identical model with stellar atmospheres.

We show the full input spectrum and predicted emission of the idealised HII region test over a wavelength range of $\lambda = 50 - 10^8$ Å in Fig. 4.5. The cosmic microwave background (CMB) and interstellar radiation field (ISRF) components are provided by Cloudy. The CMB component is a black body radiation field in strict thermodynamic equilibrium with an effective temperature of $T_{CMB} = 2.725$ K (Mather et al., 1999). The ISRF component is taken from the un-extinguished local interstellar radiation field given in Black (1987) together with the galactic background radiation field given by Draine & Bertoldi (1996). The ionising UV radiation component (red line in the upper panel of Fig. 4.5) is the output from the *SSP* for a $M_{cl} = 10^4\,M_\odot$ star cluster with an age of $t = 1$ Myr. The full predicted emission is shown in the bottom panel of Fig. 4.5. Note that there are many emission lines predicted (blue line) whose strength is below the continuum emission (red line). An observer would not be able to detect those lines under the continuum. We, therefore, have to apply an emission strength cut-off to the lines we are considering for the post-processing. We choose to only consider emission lines with an equivalent width, EW, greater than $EW > 0.1$ Å. This relates every emission line to the strength of the continuum at the line's wavelength and provides a better measure than for example a cut-off in absolute line strength.

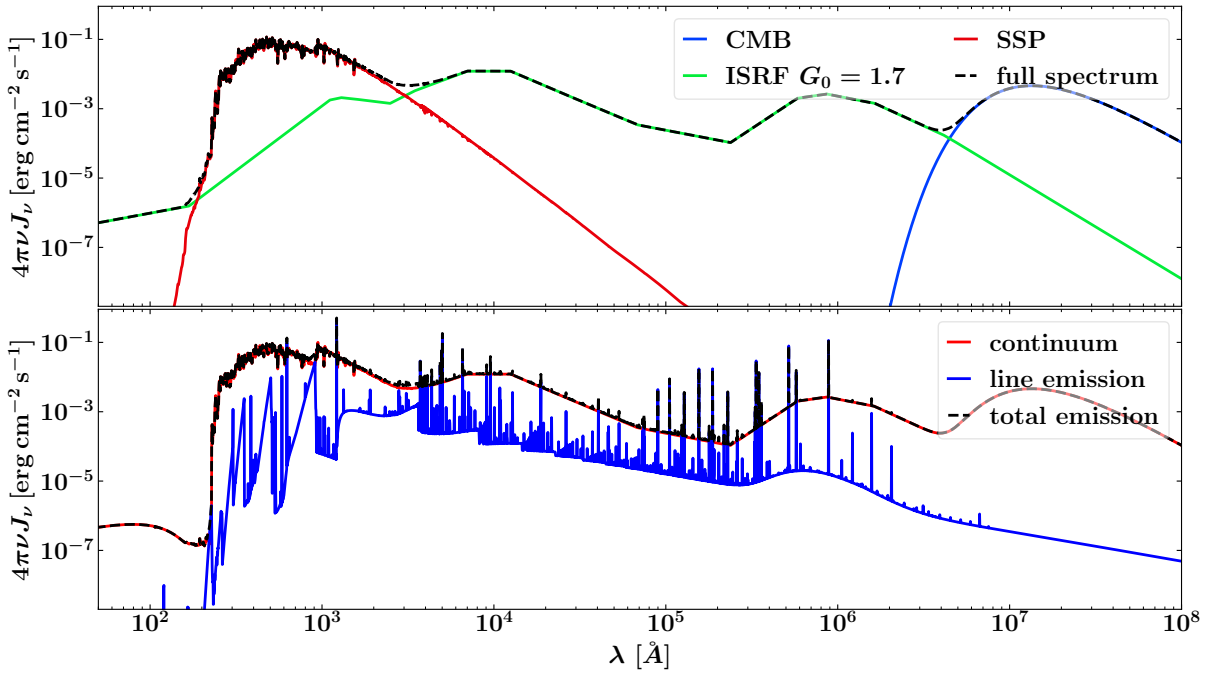

Figure 4.5: *Top* Full spectrum provided to the photo-ionisation code CLOUDY, using *SSP* for the idealised HII region test with a $M_{\rm cl} = 10^4\,{\rm M}_\odot$ central star cluster. *Bottom* The resulting emission. Note that *Cloudy* predicts emission lines below the continuum level, underlining the importance of an cut-off in equivalent width, EW, for the emission lines.

4.1.3 Resolution studies

In Fig. 4.6, we investigate how the predicted emission line ratios change with the varying resolution of the underlying AMR simulation. For this, we run the idealised HII region test with four different grid resolutions, spanning from $dx = 0.5\,{\rm pc}$ to $dx = 4\,{\rm pc}$. The latter will be the resolution of our ISM simulations we wish to post-process with ELD. The colour-coded hexbins again represent the bin count, the coloured stars show the position of the total emission within the BPT diagram. The size of the hexbins changes with the resolution but only for better visualisation purposes. The main effect of a higher resolution in our study is the capability to better resolve higher densities in the shell of the HII regions. The highest hydrogen number density in the shell of the $dx = 4\,{\rm pc}$ test is $n_{\rm H} \approx 280\,{\rm cm}^{-3}$, whereas the $dx = 0.5\,{\rm pc}$ reaches $n_{\rm H} \approx 980\,{\rm cm}^{-3}$. Similarly, the photon density right at the core of the HII region differs between the two resolutions up to a factor of ~ 10. The temperature structure is mostly unaffected by the resolution. Overall, the dependence of the resolution is only marginally and the line ratios only differ by ~ 3 per cent between the highest ($dx = 0.5\,{\rm pc}$) and the lowest ($dx = 4\,{\rm pc}$) resolution tested here. We can safely say that the HII regions in our $dx = 4\,{\rm pc}$ ISM simulations are sufficiently converging for meaningful post-processing.

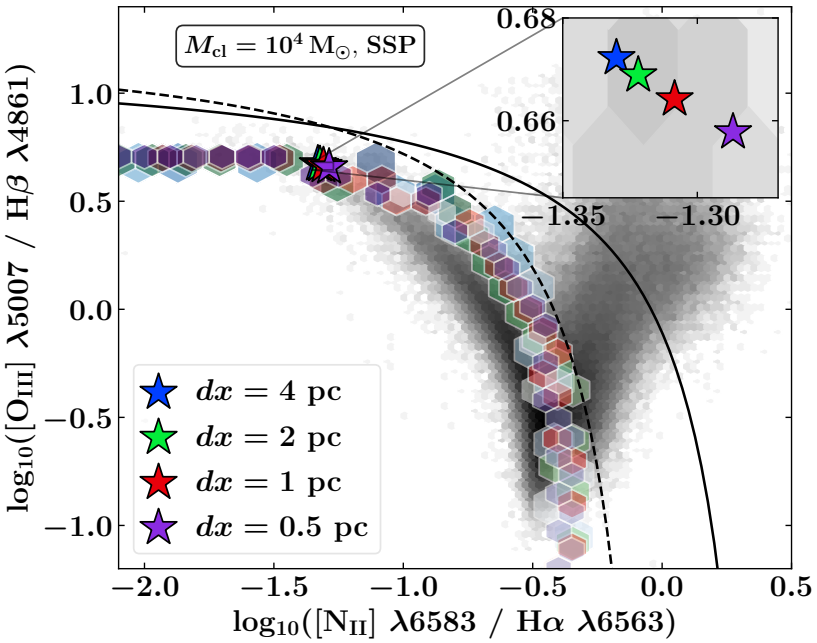

Figure 4.6: Resolution study for the idealised HII region with a $10^4\,{\rm M}_\odot$ cluster, using the SSP realisation for the radiation spectrum. The bin width of the transparent hexbins scales with the resolution. This is only for visualisation purposes and has no physical meaning in this case. The difference of the position in the BPT diagram only changes slightly with increasing resolution of the underlying simulation and is at a resolution of $dx = 4\,{\rm pc}$ sufficiently converged, which is the resolution of our high-resolution ISM simulations.

4.2 Optical emission line diagnostics for the simulated ISM

We apply ELD to four full-scale ISM simulations at two different snapshots each. The simulations differ by their initial gas surface density with $\Sigma_{\rm gas} = 10\,{\rm M}_\odot\,{\rm pc}^{-2}$ (labelled *s010)*, $\Sigma_{\rm gas} = 30\,{\rm M}_\odot\,{\rm pc}^{-2}$ (labelled *s030)*, $\Sigma_{\rm gas} = 50\,{\rm M}_\odot\,{\rm pc}^{-2}$ (labelled *s050)*, and $\Sigma_{\rm gas} = 100\,{\rm M}_\odot\,{\rm pc}^{-2}$ (labelled *s100*). All simulations include stellar feedback in form of SN, stellar winds and ionising UV radiation, as well as CR acceleration in SN remnants and anisotropic CR diffusion, an SN type Ia background, and runaway stars. The type Ia SN rates scale with the gas surface density and are 3.0, 14.0, 28.6, 75.4 ${\rm Myr}^{-1}$, respectively. We also increase the strength of the interstellar radiation field up to $G_0 = 42.7$, the CR ionisation rate up to $\zeta_{\rm H} = 3 \times 10^{-16}\,{\rm s}^{-1}$, and the initial magnetic field strength from $|\mathbf{B}_{\rm s010}| = 6\,\mu{\rm G}$ up to $|\mathbf{B}_{\rm s100}| = 19\,\mu{\rm G}$. To aid the reader's comprehension: The run *s010* would be labelled as **XCIR** in the naming convention of Chapter 3 or *SWRC-typeIa-runaways* in the naming convention of Chapter 2. The two snapshots for each simulation are taken 25 Myr and 50 Myr after the onset of star formation, indicated as t_{25} and t_{50}.

We list average star formation and SN rates for the four simulations in Table 4.2. All rates are averaged over a time span of 25 Myr. Star formation and SN rates increase non-linear with increasing gas surface density. The simulation with the lowest surface density, *s010*, did not

Table 4.2: Initial gas surface densities, initial $\Sigma_{\rm gas}$, average SFR surface densities, $\Sigma_{\rm SFR}$, and average SN rates (SNR) for the post-processed ISM simulations. The star formation and SN rates marked with t_{25} are averaged over the first 25 Myr after the onset of star formation, whereas rates labelled with t_{50} are averaged starting from 25 Myr after the onset of star formation until 50 Myr after the onset of star formation.

Label	initial $\Sigma_{\rm gas}$ $[{\rm M}_\odot\,{\rm pc}^{-2}]$	$\Sigma_{\rm SFR}^{t25}$ $[{\rm M}_\odot\,{\rm yr}^{-1}\,{\rm pc}^{-2}]$	$\Sigma_{\rm SFR}^{t50}$ $[{\rm M}_\odot\,{\rm yr}^{-1}\,{\rm pc}^{-2}]$	SNR^{t25} $[{\rm Myr}^{-1}]$	SNR^{t50} $[{\rm Myr}^{-1}]$
s010	10	6.3×10^{-4}	1.9×10^{-4}	4.6	7.2
s030	30	1.0×10^{-2}	4.7×10^{-3}	66.1	67.3
s050	50	1.3×10^{-2}	5.5×10^{-3}	82.2	101.3
s100	100	2.3×10^{-2}	4.5×10^{-2}	241.5	329.2

evolve through many cycles of star formation up until t_{25}, which lead to lower emission and a less reliable signal for the BPT analysis.

In Fig. 4.7 and Fig. 4.8, we show visualisations for the gas column density, $\Sigma_{\rm gas}$ (top row), and ionising photon energy column density, $\Sigma\gamma$ (bottom row), for the four simulations at t_{25} and t_{50}, respectively. The white circles represent star clusters. The size of a circle scales with the mass of the cluster it is representing. Please note that the size of this representation is not a depiction of the physical size of the star cluster. Individual OB runaway stars are shown with smaller black circles. The massive runaway stars carry their HII regions with them into regions otherwise devoid of ionised gas (Fig. 4.8, bottom right panel).

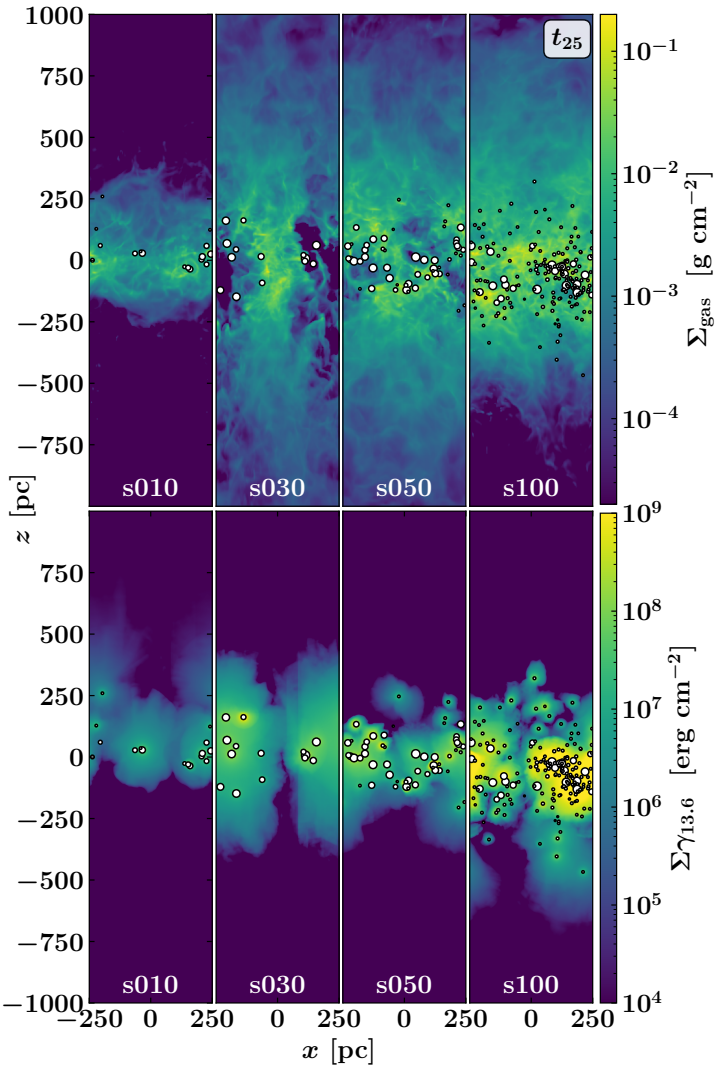

Figure 4.7: *Top panel* Edge-on view of the total gas column density, $\Sigma_{\rm gas}$, for the four full-scale ISM simulations we are using for our analysis (see Rathjen et al., 2021, and Rathjen et al., in prep.). The initial gas surface densities are $10, 30, 50, 100\,{\rm M}_\odot\,{\rm pc}^{-2}$, respectively from left to right. The runs are labelled *s010*, *s030*, *s050* and *s100*. The snapshots are taken at individual times for each simulation, always 25 Myr after the onset of star formation. The white circles represent star clusters, whereas the size of the circle scales with the mass of the cluster. Typical cluster masses range between $10^3 - 10^4\,{\rm M}_\odot$. Smaller black circles represent single runaway OB-stars. *Bottom panel* Same as above, but with the energy column density of the ionising photons, $\Sigma\gamma$. The mid-plane ISM is interspersed with hydrogen ionising radiation. Runaway stars carry their own HII regions to larger scale-heights and are an important contribution to the overall emission. We only show the simulation box up to $|z| = 1$ kpc for visualisation purposes. The full box reaches up to $|z| = 4$ kpc.

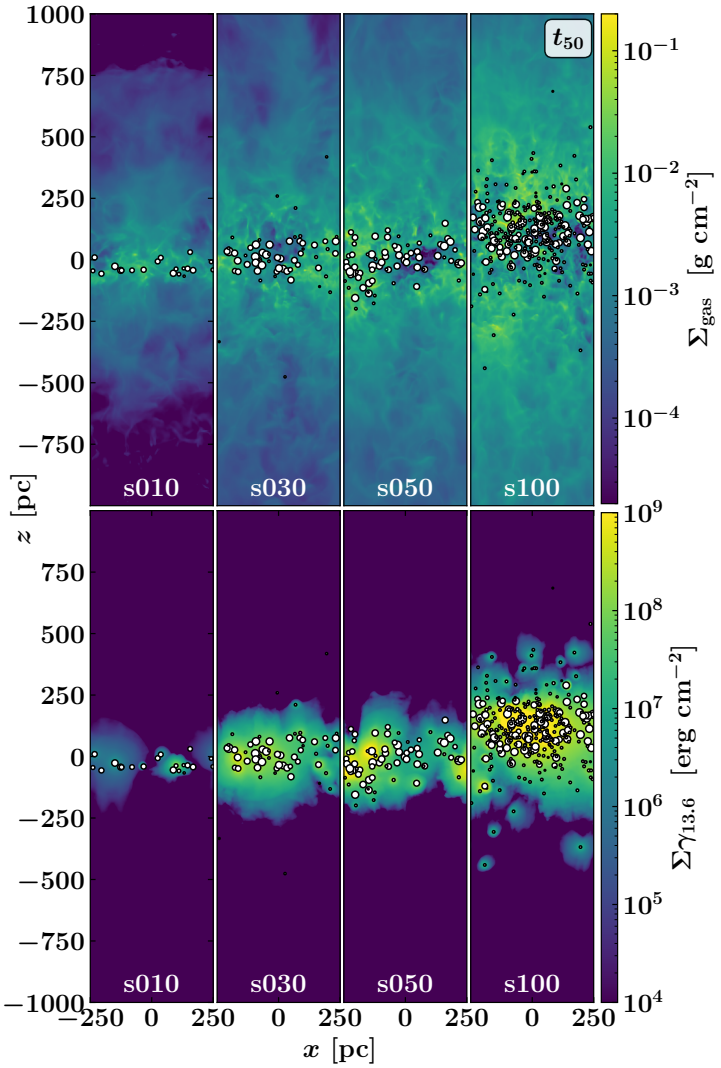

Figure 4.8: Same as Fig. 4.7, but for a snapshot 50 Myr after the onset of star formation (labelled t_{50} further on). The higher initial surface density runs have already driven strong outflows and the mid-plane ISM evolved through multiple cycles of star formation. Overlapping supernova remnants - especially in run *s100* - can shock-heat the gas to high temperatures and be the source of additional emission. We only show the simulation box up to $|z| = 1$ kpc for visualisation purposes. The full box reaches up to $|z| = 4$ kpc.

4.2.1 Emission maps

ELD predicts emission lines for every single cell in the simulations exposed to ionising radiation. However, observers mostly have only access to integrated emission along a line-of-sight. Hence, we take the 3D emission information and project it onto a 2D emission map (Fig. 4.9). We divide the $x-y-$ plane into $4 \times 4\,\mathrm{pc}^2$ pixels and integrate the emission along the $z-$ axis. This is equivalent to seeing the simulated galactic patch face-on (contrary to the edge-on visualisation of Fig. 4.7 and Fig. 4.8). Close to star formation and SN explosion sites, the medium can be assumed to be optically thin. Still, this assumption does not generally hold. Therefore, we account for attenuation through absorption by dust. We are taking the dust absorption cross-section per mass of dust, κ_{abs}, from Draine (2003) for a dust size distribution for the carbonaceous - silicate - model for interstellar dust by Weingartner & Draine (2001). We can directly convert the gas column density into a dust column density since we obtain a constant dust-to-gas ratio of 1 per cent in the chemical network of our simulations. We then can calculate the dust absorption for each cell in our simulation along the line-of-sight. The effect of dust absorption can lead to an attenuation of the optical emission down to ~ 30 per cent for individual line-of-sights at a $dx = 4\,\mathrm{pc}$ observing beam resolution. On average, the optical lines are attenuated by $\sim 5-10$ per cent, compared to the un-attenuated value. In Fig. 4.9, we show an emission map in EW for *s100*, t_{50}. We present the emission maps for the other simulations and snapshots in the Appendix 4.4 to not hinder the reading flow of this section.

4.2.2 BPT analysis

We create classic BPT diagrams for the emission in our ISM simulations as predicted by our post-processing tool ELD. The upper half of Fig. 4.10 shows the simulations at t_{25}, the lower half at t_{50}. Each sub-figure is divided into four panels, showing *s010*, *s030*, *s050*, and *s100*, from top to bottom, left to right. Each hexbin does not represent a single cell in the simulation (like in Fig. 4.2), but instead a single line-of-sight of the emission map (Fig. 4.9). The colour-coding again indicates the bin count, i.e. how many line-of-sights are at a certain position in the BPT diagram. We do not include every pixel from the emission map, but only account for line-of-sights in which the integrated, dust-attenuated, emission for all four optical lines of interest ([$\mathrm{N_{II}}$], Hα, [$\mathrm{O_{III}}$], Hβ) have an equivalent width $EW > 0.1$ Å. When we sum up all emission above the EW limit for the optical lines and calculate the line ratios from those values, we land at the position in the BPT diagram marked with the red star in each panel of Fig. 4.10. We also show the classification lines by Kewley et al. (2001) (solid black line) and Kauffmann et al. (2003) (dashed black line), as well as the line ratios of the nearby SDSS DR7 galaxies (Abazajian et al., 2009). Applying the cut-off in EW reduces the number of sight-lines with strong enough emission to be properly distinguishable from the continuum to only $\sim 1-5$ per cent in *s010*, $\sim 10-35$ per cent in *s030*, $\sim 35-45$ per cent in *s050*, and $\sim 70-90$ per cent in *s100*. With increasing gas surface density and following from this, increasing star formation (compare also with the values in Table 4.2), the emission strength increases. The total emission (red stars) lies within the sequence of star-forming galaxies and overall we find the characteristic curved shape in the BPT diagram (also seen in the idealised tests with one single HII region in an uniform medium, Fig. 4.2).

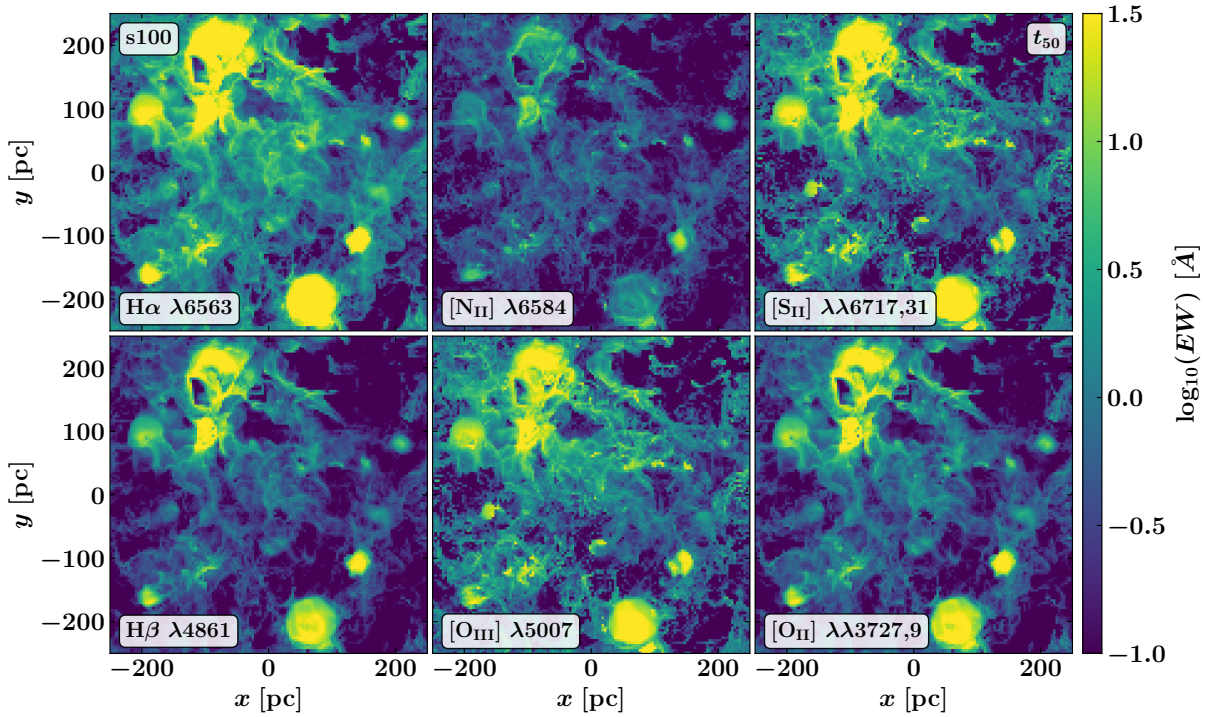

Figure 4.9: Emission maps of the optical lines Hα λ6563, [N$_{\rm II}$] λ6584, [S$_{\rm II}$] $\lambda\lambda$6717, 31 (top row, left to right), Hβ λ4861, [O$_{\rm III}$] λ5007, [O$_{\rm II}$] $\lambda\lambda$3727, 9 (bottom row, left to right) for *s100* at t_{50}. We show the equivalent width, EW, of those lines as a measure of the line strength in respect to the continuum background. As seen in Fig. 4.5, showing the EW gives a better feeling for the emission for each line since Cloudy also predicts line emission below the continuum level. An observer would not be able to distinguish this line emission from the continuum. Emission maps for the other runs with different surface densities and snapshots are in the Appendix, Fig. A4.15 to Fig. A4.18. Each $4 \times 4\,\mathrm{pc}^2$ pixel in the emission map is the integrated emission along the z-axis (i.e. the emitting patch of the galaxy is seen face-on), attenuated along the line-of-sight with a dust opacity model by Draine (2003), based on the dust size distribution by Weingartner & Draine (2001).

Nonetheless, especially *s100*, t_{50} exhibits sight-lines with strong [N$_{\rm II}$] and [O$_{\rm III}$] emission, which locates in the top right of the BPT, across the classification line for star-forming galaxies. This region in the BPT cannot be populated by pure stellar population synthesis and photo-ionisation models (Kewley et al., 2001) and has to originate from either wind-induced shocks, created from overlapping SN remnants and wind-blown bubbles from massive stars, or from AGN driven winds (see Kewley et al., 2019, and references therein). We further analyse the origin of the possibly *shock*-emission in Sec. 4.2.3 and discuss the ability to detect this emission in Sec. 4.2.4.

We compile the results of the BPT analyse for each simulation and snapshot in Fig. 4.11. The colours represent the different simulations and the symbols represent the snapshots at different times, the star for t_{25} and the cross for t_{50}. For *s010*, t_{25}, the overall rate of star formation is still

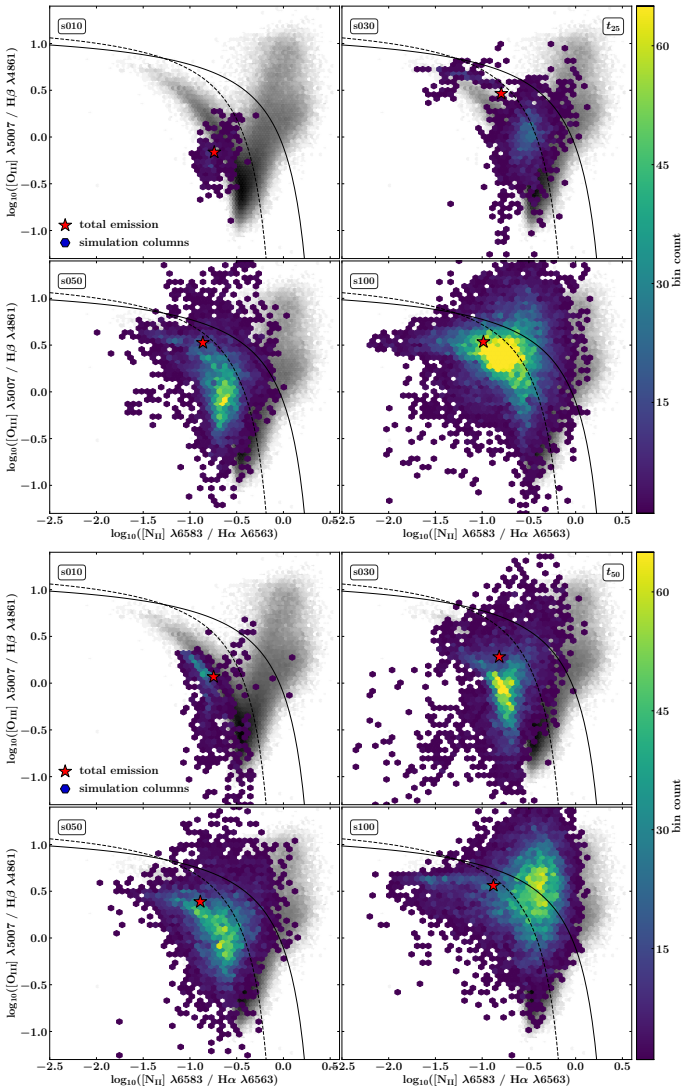

Figure 4.10: Optical emission line diagnostics with classic BPT diagrams (Baldwin et al., 1981) for *s010*, *s030*, *s050*, *s100* at t_{25} (top panels) and t_{50} (bottom panels). The line ratios are calculated from the dust-attenuated, line-of-sight integrated emission in each $dx = 4$ pc pixel (see Fig. 4.9). The colour-coding of the hexbins represent the count of pixels in that region of the BPT diagram with a bin width of 0.05 dex. The solid and dashed lines are the maximum starburst models by Kewley et al. (2001) and Kauffmann et al. (2003), respectively, the observational data data shown with grey hexbins is from SDSS DR7 (Abazajian et al., 2009). The red star represents the position of the line ratio of the total emission of the galactic patch (i.e. the emission one would observe with a beam-width of $500 \times 500\,\mathrm{pc}^2$). All of our models observed as a whole lie on the star forming sequence (position of the red star). The population of the upper right part of the BPT diagram suggests that the contribution of - possibly - shock-heated gas increases with increases gas surface densities.

low and the ISM is not fully evolved yet (see also Table 4.2). This becomes apparent also in the emission line ratio diagnostics. The total emission lies slightly below the star formation sequence (also known as HII region abundance sequence) of the SDSS data (blue star in Fig. 4.11). The snapshot 25 Myr later (*s010*, t_{50}, blue cross) moves straight up into the HII region sequence. A trend like this is explained with an increase in the ionisation parameter, U, by theoretical models (Kewley et al., 2006), which is in line with our simulation having a more evolved ISM with more total star formation events at later times. Runs *s030* and *s050* behave the exact opposite and move a bit down in the BPT diagram (green and red crosses in Fig. 4.11). Their average SFR in the first 25 Myr is rather high around $10^{-2}\,\mathrm{M_\odot\,yr^{-1}\,pc^{-2}}$ and drops down by a factor ~ 2 in the following 25 Myr window. Their average SN rate for the same time windows stays fairly constant in the case of *s030* or slightly increases ($\sim$ 20 per cent) in the case of *s050*. This phenomenon of a rather strong starburst at the beginning of the simulation which then ebbs down and regulates itself over time is a common characteristic in our ISM simulations within the SILCC framework and is mostly caused by the initial conditions of the simulation. Only for *s100* does the SFR increase by about a factor of 2 between the t_{25} average and the t_{50} average. The SNR increases as well by $\sim$ 35 per cent. Having so many SN events in a confined space and time leads to a strong overlap of SN remnants which in hand creates super-bubbles, heating the gas beyond 10^6 K and creating a large volume-filling fraction for the hot gas phase of the ISM and outflow region (compare with the overview visualisation in Fig. 4.8 and see also Sec. 2.3 and Rathjen et al. (2021)). This drives strong star-burst driven shocks whose impact we analyse in Sec. 4.2.3. It is important to have the ISM regulate itself consistently through multiple episodes of star formation (see also Rathjen et al., 2021, and Rathjen et al., in prep.). Hence, moving forward we focus our analysis on *s100*, t_{50}.

4.2.3 Origin of emission

To verify that the emission in our simulations which lies outside of the star formation sequence is indeed emission originating from shock-heated gas and not HII regions, we analyse the density-temperature phase structure of the emitting gas. Typical HII regions have a temperature of $T \approx 8000$ K and a density structure between $n_\mathrm{H} \approx 10 - 1000\,\mathrm{cm^{-3}}$ (compare with our idealised HII region tests in Sec. 4.1.1). The only physical process within the SILCC framework and in our simulations which can heat the gas above this temperature is shocks driven by overlapping SN remnants and wind-driven bubbles from massive stars. On the left panel of Fig. 4.12 from top to bottom, we show the density-temperature phase diagrams of the emitting gas for *s010*, *s030*, *s050*, and *s100*. In the middle panel, we include only the gas of which the sight-lines emission is positioned above the Kewley et al. (2001) classification line (i.e. a significant fraction of the emission must originate from either AGN - which are not present in our simulations - or shock-heated gas). In the right panel, we show the phase structure of the emission which lies below the Kauffmann et al. (2003) classification line and is therefore considered to be originating from HII regions. The horizontal dashed black line in each panel indicates $T = 9000$ K, a temperature that lies slightly beyond the typical temperature the gas can get heated by ionisation.

There is a very clear and striking cut between the possibly shock-heated gas emission (middle panel of Fig. 4.12) and the HII region emission. The total mass of gas in the upper right part of

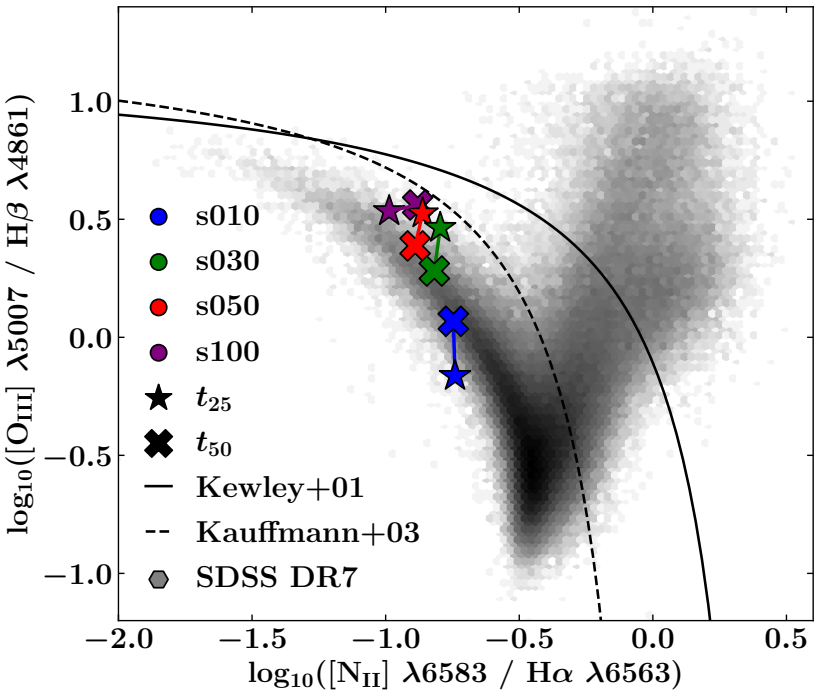

Figure 4.11: Compilation of the BPT diagnostics for the eight models analysed in this work. Stars represent the snapshots t_{25} and crosses the snapshots after 50 Myr of star formation, t_{50}. *s010* lies a bit below the star forming sequence at t_{25}. This behaviour is still influenced from the initial condition of the numerical simulation. Not much star formation has happened for the low surface density up to that time and the entire system is still influenced by the initial conditions of the MHD simulation. With increasing initial surface density the SFR increases, too, so that models *s030*, *s050* and *s100* already have a developed and self-regulated ISM at t_{25} and are therefore more robust.

the BPT diagram (Fig. 4.10) increases with increasing initial gas surface density. With a SNR of only less than 10 SN Myr^{-1} no strong shocks are present in *s010* and hence, we do not see emission above the Kewley et al. (2001) line. Nearly all gas which creates emission above the maximum starburst line lies at temperatures above $T = 9000$ K and densities below the typical minimum density of an idealised HII region of $n_{\mathrm{H}} = 10\,\mathrm{cm}^{-3}$. This establishes that the part of the emission which lies in the upper right region of the BPT diagram originates indeed from fast radiative shocks and not directly from HII regions like it is also informed by theoretical models (see e.g. Kewley et al., 2019, for a review). Nonetheless, we want to note that optical diagnostics is not the most suitable tool for detecting shock emission and separating between AGN excited emission and radiative shocks. For real observations of galaxies - where an AGN contribution cannot be simply excluded like in our case - additional information such as statistics about the velocity dispersion of the emitting gas is needed to make a founded classification of the excitation source.

Finally, we analyse the total percentage of the shocked-emission. In Fig. 4.13, we show

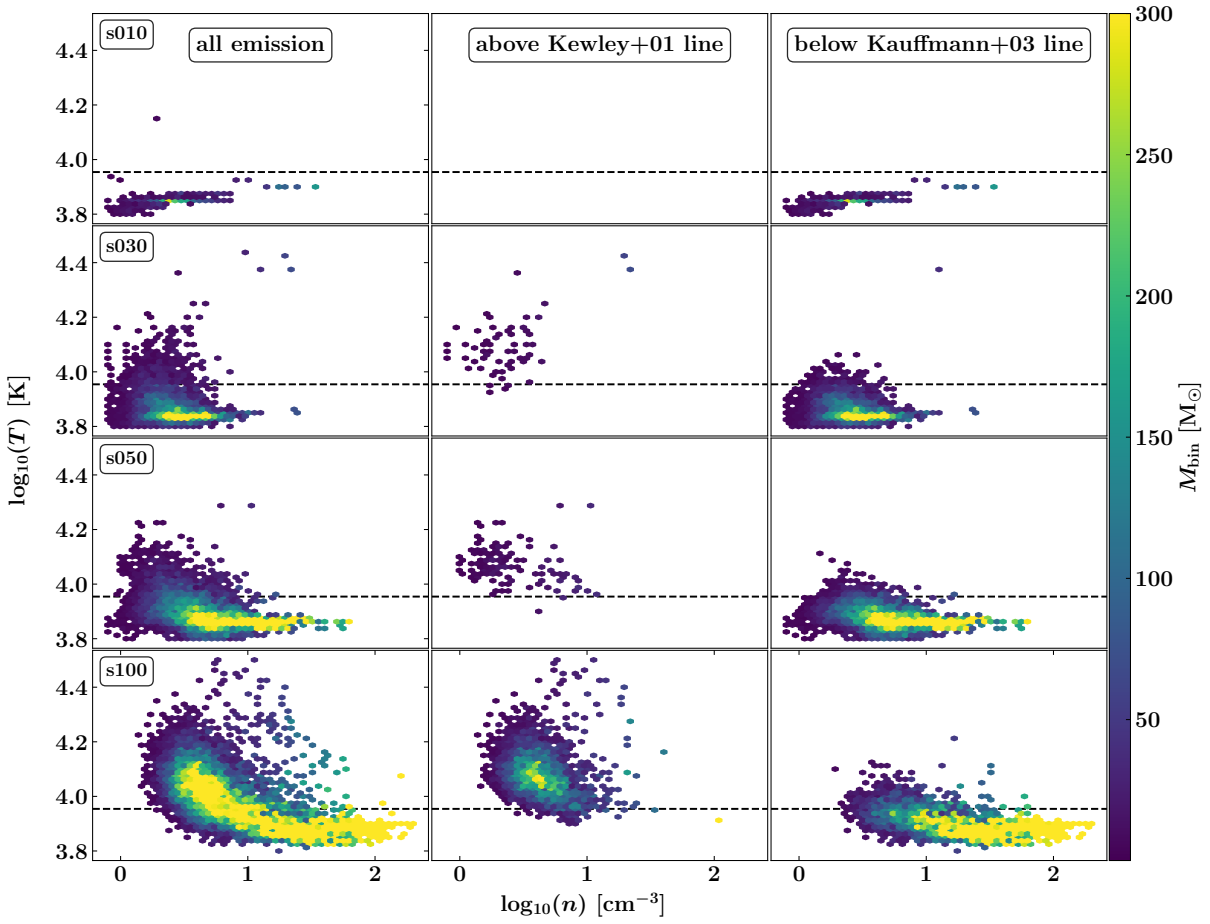

Figure 4.12: Density-temperature phase diagrams for the emitting gas in the simulations, colour-coded by total gas mass in each bin. *Left* All emitting gas columns are taken into account. *Middle* Only the columns which lie above the Kewley et al. (2001) line in the BPT diagram are taken into account (see Fig. 4.10). *Right* Only the columns which lie below the Kauffmann et al. (2003) line are taken into account. The dashed black line is at $T = 9000\,\mathrm{K}$, a temperature above the typical temperature of HII regions (compare also with Fig. 4.1). Emission line ratios above the maximum starburst model lines are considered to originate either from AGN (Thomas et al., 2016) or fast radiative shocks (Allen et al., 2008). Nearly all emission from this region in the BPT diagram in our models comes from gas above the typical density and temperature of HII regions and can safely be assumed to originate from shock-heated gas. The number of line ratios excited by shock-heated gas increases with increasing initial gas surface density.

the total emission flux above the *EW* cut-off of 0.1 Å for the two snapshots we have been using throughout our analysis (top panel: t_{25}, bottom panel: t_{50}) for the four relevant optical emission lines as a function of the initial gas surface density (solid lines). With dashed lines, we show the flux of the emission above the starburst classification line by Kewley et al. (2001). The total emission increases nearly linearly with the gas surface density, which correlates with the

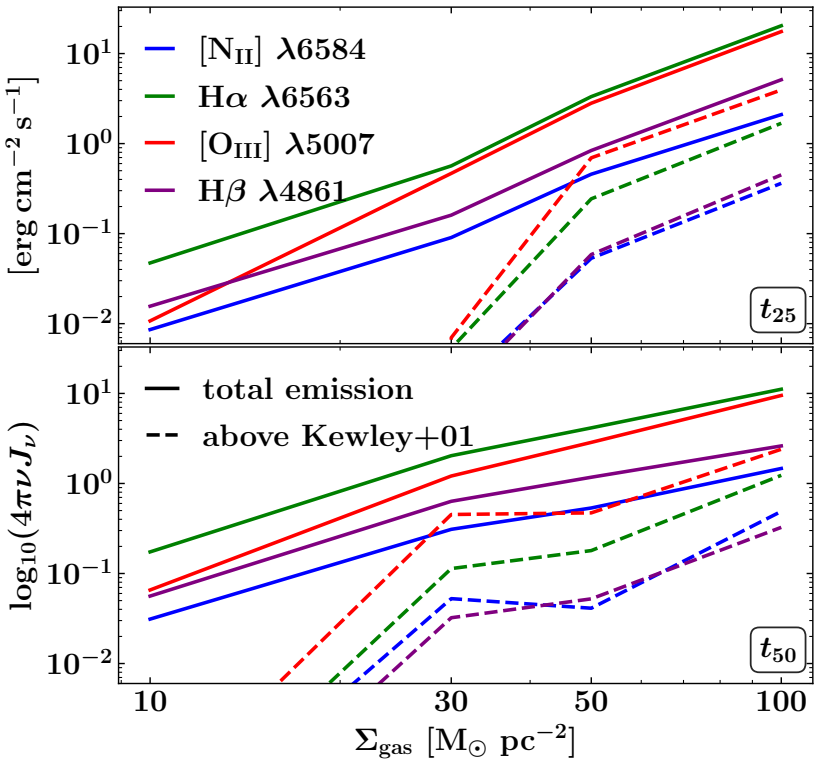

Figure 4.13: The total emission of the four optical lines investigated in this work increases nearly linearly with the gas surface density of the respective models, whereas possibly shock-heated gas emission only becomes relevant for higher surface densities, where it can amount up to 30 per cent of the total emission for individual lines.

star formation activity. Between $\sim 25-33$ per cent of the nitrogen and oxygen emission comes from the radiative shock component at the highest surface density, *s100*, whereas the amount of shock-emission at $\Sigma_{\mathrm{gas}} = 10\,\mathrm{M_\odot\,pc^{-2}}$ is basically zero. The hydrogen recombination lines are affected to a lesser extent by the shock-heated gas.

4.2.4 Impact of beam resolution

So far, we have presented the emission of the ISM measured in columns of $4 \times 4\,\mathrm{pc}^2$ beam size - limited by the maximum resolution of our ISM simulation, as well as the line ratio for the total emission, i.e. measuring the galactic patch of our simulation with a $500 \times 500\,\mathrm{pc}^2$ beam - the total box size in x and y of our domain. Now, we want to illustrate at the example of *s100*, t_{50} how the BPT diagram would look like with different observational capabilities.

In Fig. 4.14, we show a total of four BPT diagrams viewed by four different beamwidths, dx = 4, 32, 128, 256, pc (top left, top right, bottom left, bottom right). Above each BPT diagram, we show emission line ratio maps for [N II] λ6584 / Hα λ6563 (labelled BPT: x, top left of each BPT) and [O III] λ5007 / Hβ λ4861 (labelled BPT: y, top right of each BPT). White regions

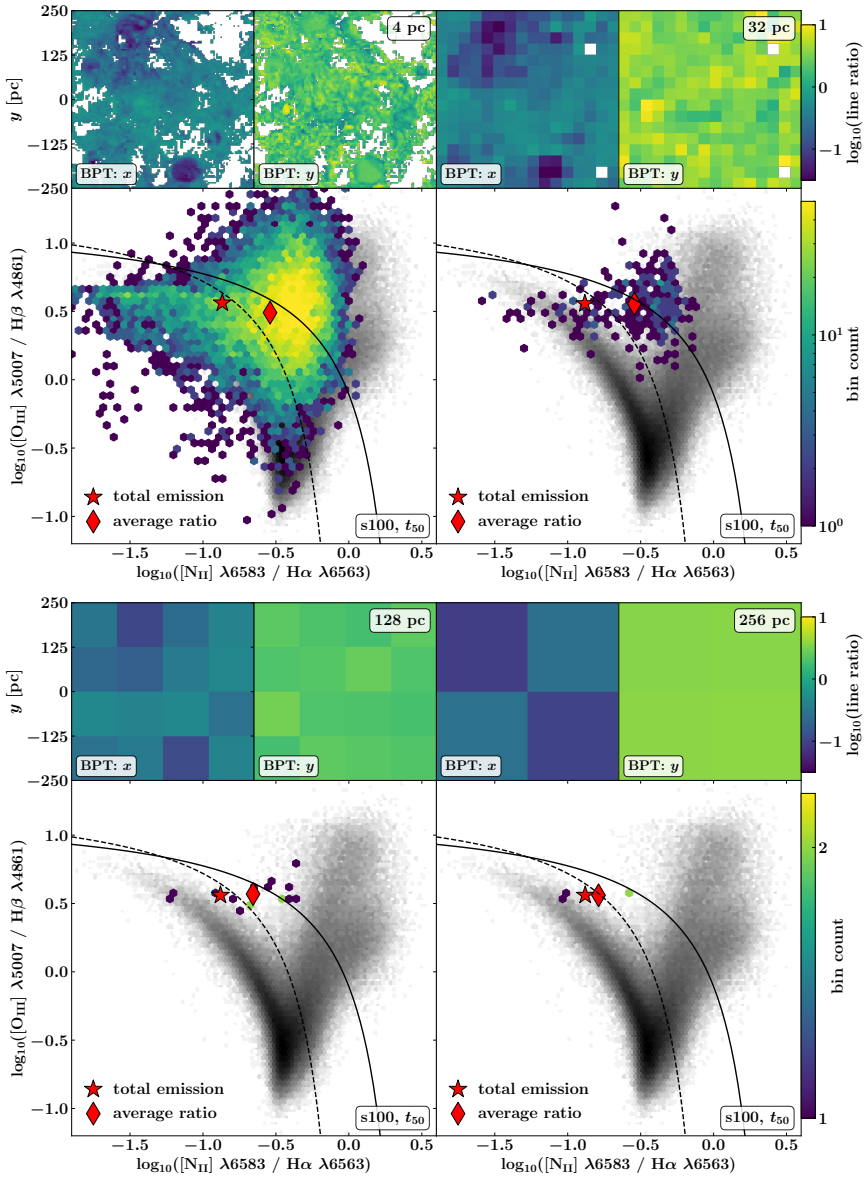

Figure 4.14: Study to understand the impact of different beam sizes on the results in the BPT diagram. We take *s100*, t_{50} and calculate the emission line ratios with varying resolution. On top of each BPT diagram are the line ratios map viewed at a certain resolution, top left [N$_{\rm II}$] λ6584 / Hα λ6563 (labelled BPT: x) and top right [O$_{\rm III}$] λ5007 / Hβ λ4861 (labelled BPT: y). The line ratio of the total emission (i.e. measured with a beam size of 500 pc^2) is indicated by the red star. The red diamond is the average position of all integrated line-of-sight line ratios in the BPT diagram. This value is strongly dependent on the resolution of the observer's beamwidth and it converges towards the line ratio of the total emission with increasing beamwidth. Features like the shock-heated gas emission in the top right region of the BPT diagram can be lost when the line ratios are measured with too coarse beam sizes.

in the emission maps are different lines-of-sight that did not fulfil the equivalent width cut of $EW > 0.1$ Å for all four optical lines used in the ratios. The red star in each panel is again the position of the line ratio of the total sum of each line like it was in the previous BPT analyses (see Fig. 4.10). The red diamond, on the other hand, is the average of the hexbins in the BPT diagram. This can be interpreted as a likelihood of measuring a specific line ratio in the $500 \times 500\,\mathrm{pc}^2$ galactic patch when taking only one line-of-sight at a given beamwidth. Naturally, with increasing beamwidth the average ratio (red diamond) converges to the total emission (red star). At this point, we like to note again that the bin size of the hexbins does not correlate with the observing beamwidth, but rather with the energy/intensity resolution of the observing instrument, which in our case is only limited by the machine precision of the simulation. Therefore, we picked an arbitrary hexbin size of 0.05 dex to obtain the best visualisation. The value of the average line ratio strongly depends on the beamwidth of the observation. Features like the shock-emission, which makes up to $\sim$ 30 per cent of the total emission, are getting lost when using coarser resolution, introducing a ambiguity into the classification of more distant objects. Observed with a $500\times500\,\mathrm{pc}^2$ beam, *s100*, t_{50}, appears to be fully within the star-forming sequence classification, whereas up to 30 per cent of its emission originates from the AGN/radiative-shock excited regime.

4.3 Summary

In this chapter, we introduced ELD - **e**mission, **l**ine **d**iagnostics - a post-processing tool in combination with the photo-ionisation code Cloudy. This tool predicts optical line emission and their line ratio diagnostics for AMR, MHD simulations. We are applying ELD to high-resolution state-of-the-art ISM simulations of different initial environments. The underlying ISM simulations incorporate one of the up-to-date most complete set of physical processes within the field of numerical ISM modelling, notably self-consistent HII regions via on-the-spot radiative transfer with TreeRay (Wünsch et al., 2021), CR acceleration and diffusion (see also Sec. 2 and Rathjen et al., 2021), and the inclusion of runaway stars. As far as we are aware, this is the first analysis of this kind. We tested our tool with idealised setups of single HII regions in controlled environments and are fully aligned with theoretical predictions (see e.g. Kewley et al., 2006), as well as observational data (Abazajian et al., 2009). Our analysis gives another confirmation of the theoretical excitation source classification developed by Kewley et al. (2001) and (Kauffmann et al., 2003). Emission from radiative shocks becomes important in more violent environments with higher gas surface densities and star formation activity where it can make up to 30 per cent of the total emission of individual lines. Nevertheless, high-resolution observations - a beamwidth of at least $dx = 32$ pc within our framework - are needed to detect the features of the shock-emission and distinguish it from the HII region abundance sequence.

4.4 Appendix A4

We show the equivalent width emission maps for all post-processed snapshots for completeness in Fig. A4.15 to Fig. A4.18. See Fig. 4.9 for a description.

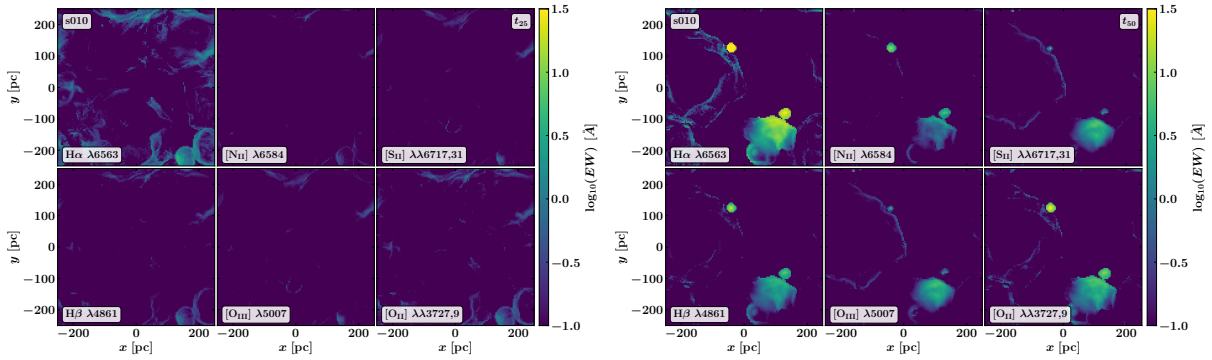

Figure 4.15: Emission map *s010*, left: t_{25}, right: t_{50}

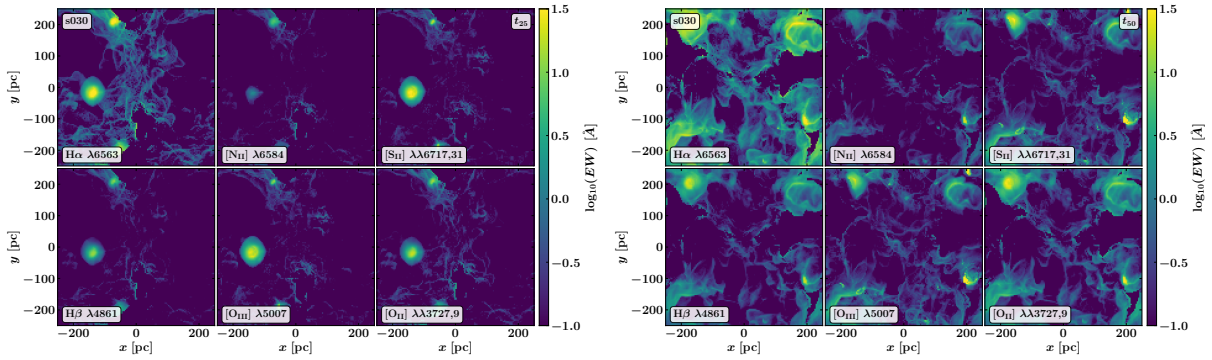

Figure 4.16: Emission map *s030*, left: t_{25}, right: t_{50}

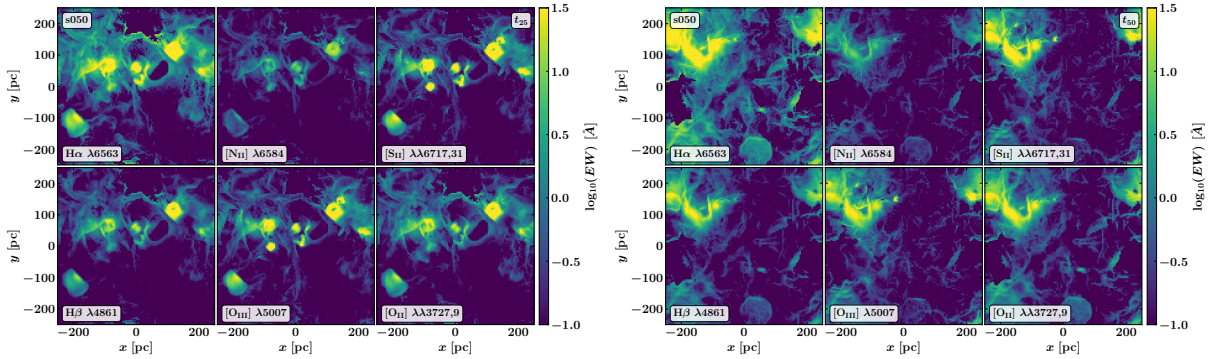

Figure 4.17: Emission map *s050*, left: t_{25}, right: t_{50}

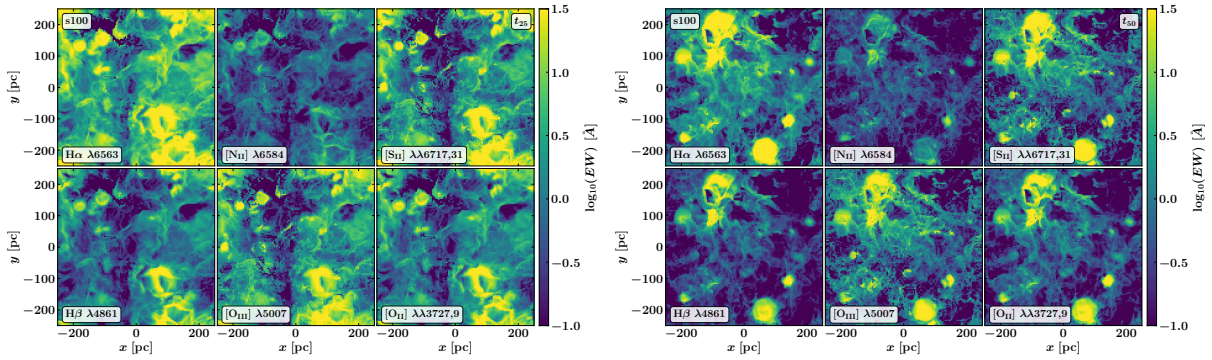

Figure 4.18: Emission map *s100*, left: t_{25}, right: t_{50}

Chapter 5

Conclusion and future prospects

We extensively studied how the ISM is formed and how stellar feedback can shape the structure and influence the outflow behaviour of the ISM. For the first chapter of the thesis, we run a set of six high-resolution, parsec-scale stratified disk MHD simulations with increasing stellar feedback complexity. We especially study the effect early feedback has on star and star cluster formation. Our findings suggest that it is indispensable to consider early feedback in form of stellar winds and ionising UV radiation when simulating the star-forming ISM. Without early feedback, star cluster grow to masses beyond $M_{\rm cl} = 10^5\,{\rm M}_\odot$, contradicting observational limits (Sec. 2.4.1. The resulting strong clustering of SNe leads to an episode of violent ballistic outflows, fully depleting the mid-plane ISM (see Fig. 2.2). However, including ionising radiation, provided by TreeRay (Wünsch et al., 2021), lead to a self-regulation of star formation, star cluster masses compatible with local neighbourhood estimates (Fig. 2.9) and a fully evolved ISM with reasonable warm gas VFF, ${\rm VFF}_{\rm warm} = 60 - 80$ per cent. CR play a subordinate role in shaping the ISM but have an important dynamical impact on galactic outflows and fountain flows. Our models strongly suggest that the star formation history is not solely regulated by outflow and inflow but instead on star cluster scales by radiation and wind feedback.

We continued with further investigating the dynamical impact of CR on galactic outflows by simulating the long-term evolution of the ISM up to $t = 250\,{\rm Myr}$. We set up another suite of six simulations, three with and three without CR, including ionising UV radiation, stellar winds and type II SNe in all of them. We also included a type Ia SNe background component and runaway stars in each of the runs with and without CR. The runaway stars are ejected from their parental star clusters via two different mechanisms, the dynamical ejection at the birth of the cluster (Poveda et al., 1967) and the binary supernova scenario (Blaauw, 1964). The runaway stars in models without CR have a strong influence on the overall mass outflow rates, but in a different way than naively assumed. We find that 80 per cent of all runaway stars explode as SNe in an ambient density environment one order of magnitude denser than their natal star clusters (Fig. 3.4). The effects of clustered SNe and early stellar feedback efficiently disperse the gas around the star cluster. The runaway stars in our models, however, travel $\sim 200\,{\rm pc}$ (Fig. 3.5) above and below the mid-plane into denser regions. Nonetheless, the very first runaway stars which are ejected via DES, i.e. which are still young and have a larger travel time, can propagate into low-density environments and enable an early build-up of a hot gas phase. This hot gas

phase can drive a galactic outflow early on but is not able to sustain it. Instead, a fountain flow establishes, replenishing and compressing the gas in the disk and trigger a new episode of star formation (compare with the early onset of an outflow in Fig. 3.6). This leads to the highest hot gas volume-filling factor in our simulations without CR of $\mathrm{VFF_{hot}} \approx 50$ per cent (Fig. 3.12) and resulting from this the highest mass and energy loadings of simulations without CR. With CR the picture is drastically different. It takes up to 100 Myr for the CR pressure gradient to fully develop up to a height of $|z| = 1$ kpc. However, once established the additional energy reservoir of the inefficiently cooling CR sustain and lift a continuous outflow even in episodes of low star formation and with an average $\mathrm{VFF_{hot}} \approx 10 - 20$ per cent during periods of strong outflow. The outflow is very smooth and dominated by the warm gas phase (Fig. 3.7), in contrast to the fast and hot outflow driven in the model with runaway stars. CR-driven outflow has a typical outflow velocity of $v_{\mathrm{out}} = 10\,\mathrm{km\,s^{-1}}$ (Fig. 3.13), which is way below the escape velocity of the Milky-Way like galactic disk at solar radius. This outflowing gas falls back onto the disk with a long turnover time, creating a slow and steady fountain flow.

In the last part of the thesis, we developed a new tool to couple the photo-ionisation code Cloudy to our ISM simulations and predict optical emission lines in post-processing. We test and benchmark the tool with idealised simulations of single HII regions in a controlled environment and find that the calculated emission follows theoretical predictions. The position for the predicted line ratios for the optical emission lines [$\mathrm{N_{II}}$], Hα, [$\mathrm{O_{III}}$], Hβ for the analysed ISM simulations, sits right into the star-forming sequence of local SDSS galaxies. Galaxies with higher initial gas surface densities produce an increasing amount of emission from shock-heated gas, up to 30 per cent. When we analyse the phase-structure of the emission regions which lie above the Kewley et al. (2001) classification line in the BPT diagram we find indeed that the gas is too hot and too sparse the be part of a HII region but instead has to be heated by overlapping SN remnants. Whether or not the shock-heated component of the emission can be detected with the BPT diagnostics depends strongly on the resolution of the observing beam. Features like the shock-heated gas emission can be lost when the line ratios are measured with too coarse beam sizes.

Even though we try to account for all major thermal and non-thermal ISM processes in the SILCC framework there are still shortcomings and possible improvements for future studies.

- *The molecular gas phase* As discussed in Chapter 2, Sec. 2.5, we fail to fully capture the molecular gas phase within the high-resolution ISM simulations with at a refinement level of $dx = 4$ pc. One reason might be that the star cluster sink particles *trap* the molecular gas since the regions of the ISM favourable for the formation of $\mathrm{H_2}$ also facilitate star formation. Another reason might be that the resolution of $dx = 4$ pc is simply not high enough for the formation of CO and $\mathrm{H_2}$. The SILCC-Zoom project (Haid et al., 2019; Seifried et al., 2017, 2020) takes individual giant molecular clouds which have formed within the parsec-scale ISM simulations and re-simulates them with a refinement as high as $dx \approx 0.01$ pc. They demonstrated that the molecular gas abundances do not converge before resolving $dx \approx 0.5$ pc. Increasing the level of refinement by one stop, i.e. dividing the resolution by 2, increases the computational load by a factor of ~ 16 (2 times more cells in x, y, z, each, as well as shortening the time-step dt by a factor of 2). Trying to

simulate a full galactic patch with a developed ISM and outflow regions at this resolution would increase the computational demand by more than a factor 1000, which is - at the current state of super-computers - not feasible.

- *Missing a galactic context* The SILCC framework is based on stratified disk simulations in a 500 pc $\times$ 500 pc $\times$ $\pm$4 kpc computational domain, which sits *statically* in the Galaxy at solar radius. Large scale shearing flows from a differential galactic rotation are so far neglected. We have argued so far that the dynamical impact of galactic shear on a domain of size $L_x = 500$ pc during a time scale of up to $t = 250$ Myr is negligible. Still, we aim to push our ISM simulations further with longer simulation times for better statistics on the large-scale fountain flows. Also, we want to increase the size of the computational domain to $L_x = 1$ kpc to reduce the effects of periodicity and allow for a more consistent formation of super-bubbles. When we do so, the dynamic effects of galactic shear start becoming important and we have to transition from the current implementation of periodic and outflowing boundary conditions in our computational domain to a shearing box, like it is already done by other groups (see e.g. Colling et al., 2018; Kim & Ostriker, 2017).

- *Radiative transfer with only one energy bin* The radiative transfer tool TreeRay (Wünsch et al., 2021) works at its current state with one energy bin for hydrogen ionising UV radiation $h\nu \geq 13.6$ eV. Extending the module to a total of 5 energy bands is currently in progress. The radiation energy bands split up into $5.6 < h\nu < 11.2$ eV for photoelectric heating, $11.2 < h\nu < 13.6$ eV for H_2 dissociation by far-UV photons, $13.6 < h\nu < 15.2$ eV for photons which can ionise atomic hydrogen, but not molecular hydrogen, $15.2 < h\nu < 24.4$ eV for photons which can photo-ionise both hydrogen species, and $h\nu > 24.4$ eV which can ionise helium and doubly ionised carbon. In combination with higher spatial resolution this allows to follow the radiation fronts much more accurately. Furthermore, we can use the radiation spectrum directly for our post-processing tool *ELD* and do not rely anymore external models with additional assumptions.

- *Cosmic rays* Similarly, extending the CR module into multiple energy bins to follow the spectral evolution of the CR is currently in development with first results published in Girichidis et al. (2020). This will allow for an investigation of gamma-ray properties as well as ionisation structures at unprecedented resolution.

The main focus of our studies within the SILCC project so far was on galactic patches in solar neighbourhood environments with a gas surface density of $\Sigma_{\rm gas} = 10\,{\rm M}_\odot\,{\rm pc}^{-2}$. We have only recently started considering higher surface density environments (see Chapter 4) and there is plenty of room for more investigation. How does the feedback change in case of higher surface density? Will the higher density lead to more efficient cooling of the ISM and reduce the feedback effects? Or will the more numerous collapsing regions allow for a more efficient overlap of feedback bubbles that more efficiently form a hot outflow-driving gas phase? How is the composition of the gas and the mixing in the disc-halo interface? Will the runaway star fraction and the resulting differently distributed feedback have a more important impact at higher

surface density compared to solar neighbourhood conditions or will the more numerous stars and stellar clusters outweigh the effect of runaways?

And finally, we can deploy our post-processing tool for predicting optical emission lines, *ELD*, to different environments. Instead of focusing on the star-forming ISM, we can post-process full galaxy simulations which are also powered by AGN and test whether the line ratio classification analyses still holds. We can also increase the wavelength range to model infrared and far-UV emission which might enable us to make predictions for the emission of more distant objects.

Overall, we hope that the results of this thesis help to deepen the understanding of the star-forming, multi-phase ISM and what processes can launch and sustain galactic outflows. The field of numerical ISM studies is far from being exhausted and new observational insights and ever more improving numerical methods and tools will continue to drive our comprehension of the interstellar medium, the life-cycle of molecular clouds and the birthplaces of the stars, from which all life originates.

Per Aspera Ad Astra.

Bibliography

Abazajian K. N., Adelman-McCarthy J. K., Agüeros M. A., Allam S. S., Allende Prieto C., An D., Anderson K. S. J., et al., 2009, ApJS, 182, 543

Ackermann M., Ajello M., Allafort A., Baldini L., Ballet J., Barbiellini G., Baring M. G., et al., 2013, Science (80-.)., 339, 807

Agertz O., Kravtsov A. V., Leitner S. N., Gnedin N. Y., 2013, Astrophys. J., 770, 25

Allen M. G., Groves B. A., Dopita M. A., Sutherland R. S., Kewley L. J., 2008, Astrophys. J. Suppl. Ser., 178, 20

Andersson E. P., Agertz O., Renaud F., 2020, Mon. Not. R. Astron. Soc., 494, 3328

Baldwin J. A., Phillips M. M., Terlevich R., 1981, Publ. Astron. Soc. Pacific, 93, 5

Barber C. B., Dobkin D. P., Huhdanpaa H., 1996, ACM Trans. Math. Softw., 22, 469

Barnes J., Hut P., 1986, Nature, 324, 446

Bastian N., Schweizer F., Goudfrooij P., Larsen S. S., Kissler-Patig M., 2013, Mon. Not. R. Astron. Soc., 431, 1252

Bell A. R., 1978, Mon. Not. R. Astron. Soc., 182, 443

Bigiel F., Leroy A., Walter F., Brinks E., De Blok W. J., Madore B., Thornley M. D., 2008, Astron. J., 136, 2846

Bisbas T. G., Haworth T. J., Williams R. J., Mackey J., Tremblin P., Raga A. C., Arthur S. J., et al., 2015, Mon. Not. R. Astron. Soc., 453, 1324

Blaauw A., 1964, Annu. Rev. Astron. Astrophys., 2, 213

Black J. H., 1987, in , Vol. 134, Interstellar Process. Proc. a Symp. held Gd. Tet. Natl. Park. Wyo., July, 1986, Dordr. Reidel, 1987, Ed. by David J. Hollenbach, Harley A. Thronson. Astrophys. Sp. Sci. Libr. Vol. 134, p.731. Springer Netherlands, pp 731–744, doi:10.1007/978-94-009-3861-8_27, https://ui.adsabs.harvard.edu/abs/1987ASSL..134..731B/abstract

Blandford R. D., Ostriker J. P., 1978, Astrophys. J., 221, L29

Blondin J. M., Wright E. B., Borkowski K. J., Reynolds S. P., 1998, Astrophys. J., 500, 342

Booth C. M., Agertz O., Kravtsov A. V., Gnedin N. Y., 2013, Astrophys. J. Lett., 777, 16

Bouchut F., Klingenberg C., Waagan K., 2007, Numer. Math., 108, 7

Bouchut F., Klingenberg C., Waagan K., 2010, Numer. Math., 115, 647

Bressan A., Marigo P., Girardi L., Salasnich B., Dal Cero C., Rubele S., Nanni A., 2012, Mon. Not. R. Astron. Soc., 427, 127

Bruzual G., Charlot S., 2003, Mon. Not. R. Astron. Soc., 344, 1000

Butler M. J., Tan J. C., Teyssier R., Rosdahl J., Van Loo S., Nickerson S., 2017, Astrophys. J., 841, 82

Caffau E., Ludwig H. G., Steffen M., Freytag B., Bonifacio P., 2011, Sol. Phys., 268, 255

Castor J., Weaver R., McCray R., 1975, Astrophys. J., 200, L107

Chabrier G., 2003, Publ. Astron. Soc. Pacific, 115, 763

Chen Y., Bressan A., Girardi L., Marigo P., Kong X., Lanza A., 2015, Mon. Not. R. Astron. Soc., 452, 1068

Chevance M., Kruijssen J. M. D., Krumholz M. R., Groves B., Keller B. W., Hughes A., Glover S. C. O., et al., 2020a, arXiv e-prints, p. arXiv:2010.13788

Chevance M., Diederik Kruijssen J. M., Hygate A. P., Schruba A., Longmore S. N., Groves B., Henshaw J. D., et al., 2020b, Mon. Not. R. Astron. Soc., 493, 2872

Clark P. C., Glover S. C. O., Klessen R. S., 2012, Mon. Not. R. Astron. Soc., 420, 745

Colling C., Hennebelle P., Geen S., Iffrig O., Bournaud F., 2018, Astron. Astrophys., 620, A21

Cox D. P., 2005, Annu. Rev. Astron. Astrophys., 43, 337

Cox D. P., Smith B. W., 1974, Astrophys. J., 189, L105

Creasey P., Theuns T., Bower R. G., 2013, Mon. Not. R. Astron. Soc., 429, 1922

Crutcher R. M., 2012, Annu. Rev. Astron. Astrophys, 50, 29

Crutcher R. M., Kemball A. J., 2019, Front. Astron. Sp. Sci., 6, 66

Dale J. E., Bonnell I. A., Clarke C. J., Bate M. R., 2005, Mon. Not. R. Astron. Soc., 358, 291

Dale J. E., Ercolano B., Bonnell I. A., 2012, Mon. Not. R. Astron. Soc., 424, 377

Dale J. E., Ngoumou J., Ercolano B., Bonnell I. A., 2014, Mon. Not. R. Astron. Soc., 442, 694

De Avillez M. A., Breitschwerdt D., 2005, Astron. Astrophys., 436, 585

Dib S., Helou G., Moore T. J. T., Urquhart J. S., Dariush A., 2012, Astrophys. J., 758, 125

Dinnbier F., Walch S., 2020, Mon. Not. R. Astron. Soc., 499, 748

Dobbs C. L., Burkert A., Pringle J. E., 2011, Mon. Not. R. Astron. Soc., 417, 1318

Dopita M. A., Kewley L. J., Heisler C. A., Sutherland R. S., 2000, Astrophys. J., 542, 224

Dorfi E. A., Breitschwerdt D., 2012, Astron. Astrophys., 540, 77

Draine B. T., 1978, Astrophys. J. Suppl. Ser., 36, 595

Draine B. T., 2003, Astrophys. J., 598, 1017

Draine B. T., 2010, Physics of the interstellar and intergalactic medium. Princeton University Press, doi:10.2307/j.ctvcm4hzr

Draine B. T., Bertoldi F., 1996, Astrophys. J., 468, 269

Dubey A., Reid L. B., Fisher R., 2008, Phys. Scr., T132, 014046

Dubey A., Antypas K., Ganapathy M. K., Reid L. B., Riley K., Sheeler D., Siegel A., et al., 2009, Parallel Comput., 35, 512

Ekström S., Georgy C., Eggenberger P., Meynet G., Mowlavi N., Wyttenbach A., Granada A., et al., 2012, Astron. Astrophys., 537

Eldridge J. J., Langer N., Tout C. A., 2011, Mon. Not. R. Astron. Soc., 414, 3501

Eswaran V., Pope S. B., 1988, Comput. Fluids, 16, 257

Federrath C., Banerjee R., Clark P. C., Klessen R. S., 2010, Astrophys. J., 713, 269

Ferland G. J., Chatzikos M., Guzmán F., Lykins M. L., Van Hoof P. A., Williams R. J., Abel N. P., et al., 2017, Rev. Mex. Astron. y Astrofis., 53, 385

Ferrière K. M., 2001, Rev. Mod. Phys., 73, 1031

Fielding D., Quataert E., Martizzi D., Faucher-Giguère C.-A., 2017, Mon. Not. R. Astron. Soc. Lett., 470, L39

Fielding D., Quataert E., Martizzi D., 2018, Mon. Not. R. Astron. Soc., 481, 3325

Fryxell B., Olson K., Ricker P., Timmes F. X., Zingale M., Lamb D. Q., MacNeice P., et al., 2000, Astrophys. J. Suppl. Ser., 131, 273

Fujii M. S., Portegies Zwart S., 2011, Science, 334, 1380

Gatto A., Walch S., Mac Low M.-M., Naab T., Girichidis P., Glover S. C. O., Wünsch R., et al., 2015, Mon. Not. R. Astron. Soc., 449, 1057

Gatto A., Walch S., Naab T., Girichidis P., Wünsch R., Glover S. C. O., Klessen R. S., et al., 2017, Mon. Not. R. Astron. Soc., 466, 1903

Geen S., Rosdahl J., Blaizot J., Devriendt J., Slyz A., 2015, Mon. Not. R. Astron. Soc., 448, 3248

Geen S., Soler J. D., Hennebelle P., 2017, Mon. Not. R. Astron. Soc., 471, 4844

Gent F. A., Shukurov A., Fletcher A., Sarson G. R., Mantere M. J., 2013, Mon. Not. R. Astron. Soc., 432, 1396

Girichidis P., Walch S., Naab T., Gatto A., Wünsch R., Glover S. C. O., Klessen R. S., et al., 2016a, Mon. Not. R. Astron. Soc., 456, 3432

Girichidis P., Naab T., Walch S., Hanasz M., Low M.-M. M., Ostriker J. P., Gatto A., et al., 2016b, Astrophys. J., 816, L19

Girichidis P., Naab T., Hanasz M., Walch S., 2018a, Mon. Not. R. Astron. Soc., 479, 3042

Girichidis P., Seifried D., Naab T., Peters T., Walch S., Wünsch R., Glover S. C. O., et al., 2018b, Mon. Not. R. Astron. Soc., 480, 3511

Girichidis P., Pfrommer C., Hanasz M., Naab T., 2020, Mon. Not. R. Astron. Soc., 491, 993

Glover S. C. O., Mac Low M.-M., 2007, Astrophys. J. Suppl. Ser., 169, 239

Goldsmith P. F., Langer W. D., 1978, Astrophys. J., 222, 881

Gong M., Ostriker E. C., Kim C.-G., Kim J.-G., 2020, Astrophys. J., 903, 142

Gorski K. M., Hivon E., Banday A. J., Wandelt B. D., Hansen F. K., Reinecke M., Bartelmann M., 2005, Astrophys. J., 622, 759

Gräfener G., Koesterke L., Hamann W. R., 2002, Astron. Astrophys., 387, 244

Grasha K., Calzetti D., Adamo A., Kim H., Elmegreen B. G., Gouliermis D. A., Dale D. A., et al., 2017, Astrophys. J., 840, 113

Gutkin J., Charlot S., Bruzual G., 2016, Mon. Not. R. Astron. Soc., 462, 1757

Haid S., Walch S., Naab T., Seifried D., Mackey J., Gatto A., 2016, Mon. Not. R. Astron. Soc., 460, 2962

Haid S., Walch S., Seifried D., Wünsch R., Dinnbier F., Naab T., 2018, Mon. Not. R. Astron. Soc., 478, 4799

Haid S., Walch S., Seifried D., Wünsch R., Dinnbier F., Naab T., 2019, Mon. Not. R. Astron. Soc., 482, 4062

Hanasz M., Lesch H., Naab T., Gawryszczak A., Kowalik K., Wóltański D., 2013, Astrophys. J. Lett., 777, 38

Heiles C., Troland T. H., 2005, Astrophys. J., 624, 773

Heitsch F., Stone J. M., Hartmann L. W., 2009, Astrophys. J., 695, 248

Helder E. A., Vink J. S., Bykov A. M., Ohira Y., Raymond J. C., Terrier R., 2012, Space Sci. Rev., 173, 369

Hennebelle P., Iffrig O., 2014, Astron. Astrophys., 570, 81

Hill A. S., Ryan Joung M., Mac Low M.-M., Benjamin R. A., Matthew Haffner L., Klingenberg C., Waagan K., 2012, Astrophys. J., 750, 104

Hoogerwerf R., De Bruijne J. H., De Zeeuw P. T., 2001, Astron. Astrophys., 365, 49

Howard C. S., Pudritz R. E., Harris W. E., 2017, Mon. Not. R. Astron. Soc., 470, 3346

Hu C.-Y., Naab T., Glover S. C. O., Walch S., Clark P. C., 2017, Mon. Not. R. Astron. Soc., 471, 2151

Ibáñez-Mejía J. C., Mac Low M.-M., Klessen R. S., Baczynski C., 2017, Astrophys. J., 850, 62

Iffrig O., Hennebelle P., 2015, Astron. Astrophys., 576, 95

Iffrig O., Hennebelle P., 2017, Astron. Astrophys., 604, 70

Inutsuka S. I., Inoue T., Iwasaki K., Hosokawa T., 2015, Astron. Astrophys., 580, 49

Jiménez S., Tenorio-Tagle G., Silich S., 2019, Mon. Not. R. Astron. Soc., 488, 978

Joshi P. R., Walch S., Seifried D., Glover S. C. O., Clarke S. D., Weis M., 2019, Mon. Not. R. Astron. Soc., 484, 1735

Joung M. K. R., Mac Low M.-M., 2006, Astrophys. J., 653, 1266

Kado-Fong E., Kim J.-G., Ostriker E. C., Kim C.-G., 2020, Astrophys. J., 897, 143

Kafle P. R., Sharma S., Lewis G. F., Bland-Hawthorn J., 2014, Astrophys. J., 794, 59

Kalberla P. M. W., Kerp J., 2009, Annu. Rev. Astron. Astrophys., 47, 27

Kauffmann G., Heckman T. M., Tremonti C., Brinchmann J., Charlot S., White S. D., Ridgway S. E., et al., 2003, Mon. Not. R. Astron. Soc., 346, 1055

Kennicutt R. C., 1998, Astrophys. J., 498, 541

Kennicutt R. C., Evans N. J., 2012, Annu. Rev. Astron. Astrophys., 50, 531

Kewley L. J., Dopita M. A., Sutherland R. S., Heisler C. A., Trevena J., 2001, Astrophys. J., 556, 121

Kewley L. J., Groves B., Kauffmann G., Heckman T., 2006, Mon. Not. R. Astron. Soc., 372, 961

Kewley L. J., Nicholls D. C., Sutherland R. S., 2019, Understanding Galaxy Evolution through Emission Lines (arXiv:1910.09730), doi:10.1146/annurev-astro-081817-051832

Kharchenko N. V., Piskunov A. E., Röser S., Schilbach E., Scholz R. D., 2005, Astron. Astrophys., 438, 1163

Kim C. G., Ostriker E. C., 2015, Astrophys. J., 802, 99

Kim C.-G., Ostriker E. C., 2017, Astrophys. J., 846, 133

Kim C.-G., Ostriker E. C., 2018, Astrophys. J., 853, 173

Kim C.-G., Kim W.-T., Ostriker E. C., 2011, Astrophys. J., 743, 25

Kim J., Chevance M., Kruijssen J. M. D., Schruba A., Sandstrom K., Hygate A. P. S., Barnes A. T., et al., 2021, arXiv e-prints, 000, arXiv:2012.00019

Klessen R. S., Glover S. C., 2016, Saas-Fee Adv. Course, 43, 85

Klingenberg C., Schmidt W., Waagan K., 2007, J. Comput. Phys., 227, 12

Konstandin L., Shetty R., Girichidis P., Klessen R. S., 2015, Mon. Not. R. Astron. Soc., 446, 1775

Kroupa P., 2001, Mon. Not. R. Astron. Soc., 322, 231

Krumholz M. R., Bate M. R., Arce H. G., Dale J. E., Gutermuth R., Klein R. I., Li Z.-Y., et al., 2014, in Protostars Planets VI. University of Arizona Press, p. 243 (arXiv:1401.2473)

Lada C. J., Lada E. A., 2003, Annu. Rev. Astron. Astrophys., 41, 57

Lanz T., Hubeny I., 2003, Astrophys. J. Suppl. Ser., 146, 417

Leroy A. K., Walter F., Brinks E., Bigiel F., De Blok W. J. G., Madore B., Thornley M. D., 2008, Astron. J., 136, 2782

Li M., Bryan G. L., 2020, Astrophys. J., 890, L30

Li M., Ostriker J. P., Cen R., Bryan G. L., Naab T., 2015, Astrophys. J., 814, 4

Li M., Bryan G. L., Ostriker J. P., 2017, Astrophys. J., 841, 101

Mac Low M.-M., Klessen R. S., 2004, Rev. Mod. Phys., 76, 125

Mac Low M.-M., McCray R., 1988, Astrophys. J., 324, 776

Mac Low M.-M., McCray R., Norman M. L., 1989, Astrophys. J., 337, 141

MacKey J., Gvaramadze V. V., Mohamed S., Langer N., 2015, Astron. Astrophys., 573, 10

Maíz Apellániz J., Pantaleoni González M., Barbá R. H., Simón-Díaz S., Negueruela I., Lennon D. J., Sota A., et al., 2018, Astron. Astrophys., 616, A149

Martin C. L., Shapley A. E., Coil A. L., Kornei K. A., Bundy K., Weiner B. J., Noeske K. G., et al., 2012, Astrophys. J., 760, 127

Martizzi D., Faucher-giguère C. A., Quataert E., 2015, Mon. Not. R. Astron. Soc., 450, 504

Martizzi D., Fielding D., Faucher-Giguère C. A., Quataert E., Faucher C.-A., Ere G., Quataert E., 2016, Mon. Not. R. Astron. Soc., 459, 2311

Mather J. C., Fixsen D. J., Shafer R. A., Mosier C., Wilkinson D. T., 1999, Astrophys. J., 512, 511

McKee C. F., Ostriker J. P., 1977, Astrophys. J., 218, 148

McKee C. F., Ostriker E. C., 2007, Annu. Rev. Astron. Astrophys., 45, 565

McLaughlin D. E., van der Marel R. P., 2005, Astrophys. J. Suppl. Ser., 161, 304

Moe M., Di Stefano R., 2017, Astrophys. J. Suppl. Ser., 230, 15

Mottram J. C., Hoare M. G., Davies B., Lumsden S. L., Oudmaijer R. D., Urquhart J., Moore T. J., et al., 2011, Astrophys. J. Lett., 730, 33

Moustakas J., Kennicutt R. C., Tremonti C. A., Dale D. A., Smith J. D. T., Calzetti D., 2010, Astrophys. Journal, Suppl. Ser., 190, 233

Murray N., Quataert E., Thompson T. A., 2010, Astrophys. J., 709, 191

Naab T., Ostriker J. P., 2017, Annu. Rev. Astron. Astrophys., 55, 59

Nava L., Gabici S., 2013, Mon. Not. R. Astron. Soc., 429, 1643

Navarro J. F., Frenk C. S., White S. D. M., 1996, Astrophys. J., 462, 563

Nelson R. P., Langer W. D., 1997, Astrophys. J., 482, 796

Newman S. F., Genzel R., Förster-Schreiber N. M., Griffin K. S., Mancini C., Lilly S. J., Renzini A., et al., 2012, Astrophys. J., 761, 43

Oh S., Kroupa P., Pflamm-Altenburg J., 2015, Astrophys. J., 805

Olivier G. M., Lopez L. A., Rosen A. L., Nayak O., Rieter M., Krumholz M. R., Bolatto A. D., 2021, Astrophys. J., 908, 68

Pakmor R., Pfrommer C., Simpson C. M., Springel V., 2016, Astrophys. J., 824, L30

Pardi A., Girichidis P., Naab T., Walch S., Peters T., Heitsch F., Glover S. C. O., et al., 2017, Mon. Not. R. Astron. Soc., 465, 4611

Pellegrini E. W., Reissl S., Rahner D., Klessen R. S., Glover S. C., Pakmor R., Herrera-Camus R., et al., 2020, Mon. Not. R. Astron. Soc., 498, 3193

Perets H. B., Šubr L., 2012, Astrophys. J., 751

Peters T., Naab T., Walch S., Glover S. C. O., Girichidis P., Pellegrini E., Klessen R. S., et al., 2017, Mon. Not. R. Astron. Soc., 466, 3293

Pfrommer C., Pakmor R., Schaal K., Simpson C. M., Springel V., 2017, Mon. Not. R. Astron. Soc., 465, 4500

Pineda J. L., Fischer C., Kapala M., Stutzki J., Buchbender C., Goldsmith P. F., Ziebart M., et al., 2018, Astrophys. J. Lett., 869, 6 pp.

Plat A., Charlot S., Bruzual G., Feltre A., Vidal-García A., Morisset C., Chevallard J., et al., 2019, Mon. Not. R. Astron. Soc., 490, 978

Portegies Zwart S. F., McMillan S. L. W., Gieles M., 2010, Annu. Rev. Astron. Astrophys., 48, 431

Poveda A., Ruiz J., Allen C., 1967, Boletín los Obs. Tonantzintla y Tacubaya, 4, 86

Puls J., Vink J. S., Najarro F., 2008, Astron. Astrophys. Rev., 16, 209

Rahner D., Pellegrini E. W., Glover S. C. O., Klessen R. S., 2017, Mon. Not. R. Astron. Soc., 470, 4453

Rahner D., Pellegrini E. W., Glover S. C. O., Klessen R. S., 2019, Mon. Not. R. Astron. Soc., 483, 2547

Rathjen T. E., Naab T., Girichidis P., Walch S., Wünsch R., Dinnbier F., Seifried D., et al., 2021, Mon. Not. R. Astron. Soc., 504, 1039

Reissl S., Klessen R. S., Low M. M. M., Pellegrini E. W., 2018, Astron. Astrophys., 611, 70

Renzo M., Zapartas E., De Mink S. E., Götberg Y., Justham S., Farmer R. J., Izzard R. G., et al., 2019, Astron. Astrophys., 624

Rogers H., Pittard J. M., 2013, Mon. Not. R. Astron. Soc., 431, 1337

Salem M., Bryan G. L., 2014, Mon. Not. R. Astron. Soc., 437, 3312

Salpeter E. E., 1955, Astrophys. J., 121, 161

Schinnerer E., Meidt S. E., Colombo D., Chandar R., Dobbs C. L., García-Burillo S., Hughes A., et al., 2017, Astrophys. J., 836, 62

Schmidt W., Federrath C., Hupp M., Kern S., Niemeyer J. C., 2009, Astron. Astrophys., 494, 127

Schneider E. E., Ostriker E. C., Robertson B. E., Thompson T. A., 2020, Astrophys. J., 895, 43

Seifried D., Walch S., Girichidis P., Naab T., Wünsch R., Klessen R. S., Glover S. C. O., et al., 2017, Mon. Not. R. Astron. Soc., 472, 4797

Seifried D., Haid S., Walch S., Borchert E. M., Bisbas T. G., 2020, Mon. Not. R. Astron. Soc., 492, 1465

Simpson C. M., Pakmor R., Marinacci F., Pfrommer C., Springel V., Glover S. C. O., Clark P. C., et al., 2016, Astrophys. J., 827, L29

Smith M. C., Bryan G. L., Somerville R. S., Hu C.-Y., Teyssier R., Burkhart B., Hernquist L., 2020, Mon. Not. R. Astron. Soc. Adv. Access, 000, 0

Somerville R., Davé R., 2015, Annu. Rev. Astron. Astrophys., 53, 51

Spitzer L., 1942, Astrophys. J., 95, 329

Spitzer L., 1978, Physical Processes in the Interstellar Medium. Wiley, doi:10.1002/9783527617722

Stone R. C., 1991, Astron. J., 102, 333

Strong A. W., Moskalenko I. V., Ptuskin V. S., 2007, Annu. Rev. Nucl. Part. Sci., 57, 285

Tetzlaff N., Neuhäuser R., Hohle M. M., 2011, Mon. Not. R. Astron. Soc., 410, 190

Thomas A. D., Groves B. A., Sutherland R. S., Dopita M. A., Kewley L. J., Jin C., 2016, Astrophys. J., 833, 266

Tielens A. G., 2005, The physics and chemistry of the interstellar medium. Cambridge University Press, doi:10.1017/cbo9780511819056

Toalá J. A., Arthur S. J., 2011, Astrophys. J., 737, 100

Tress R. G., Smith R. J., Sormani M. C., Glover S. C., Klessen R. S., Low M. M. M., Clark P. C., 2020, Mon. Not. R. Astron. Soc., 492, 2973

Tumlinson J., Peeples M. S., Werk J. K., 2017, Annu. Rev. Astron. Astrophys., 55, 389

Waagan K., Federrath C., Klingenberg C., 2011, J. Comput. Phys., 230, 3331

Walch S., Naab T., 2015, Mon. Not. R. Astron. Soc., 451, 2757

Walch S. K., Whitworth A. P., Bisbas T., Wünsch R., Hubber D., 2012, Mon. Not. R. Astron. Soc., 427, 625

Walch S., Whitworth A. P., Bisbas T. G., Wünsch R., Hubber D. A., 2013, Mon. Not. R. Astron. Soc., 435, 917

Walch S., Girichidis P., Naab T., Gatto A., Glover S. C. O., Wünsch R., Klessen R. S., et al., 2015, Mon. Not. R. Astron. Soc., 454, 238

Weaver R., McCray R., Castor J., Shapiro P., Moore R., 1977, Astrophys. J., 218, 377

Weingartner J. C., Draine B. T., 2001, Astrophys. J., 548, 296

Whitworth A., 1979, Mon. Not. R. Astron. Soc., 186, 59

Wolfire M. G., McKee C. F., Hollenbach D., Tielens A. G. G. M., 2003, Astrophys. J., 587, 278

Wünsch R., Tenorio-Tagle G., Palouš J., Silich S., 2008, Astrophys. J., 683, 683

Wünsch R., Silich S., Palou J., Tenorio-Tagle G., Mũoz Tũón C., 2011, Astrophys. J., 740, 75

Wünsch R., Walch S., Dinnbier F., Whitworth A. P., 2018, Mon. Not. R. Astron. Soc., 475, 3393

Wünsch R., Walch S., Dinnbier F., Seifried D., Haid S., Klepitko A., Whitworth A. P., et al., 2021, Mon. Not. R. Astron. Soc., 505, 3730